

# Broadband optical quantum memory



Klaus Franz Reim

Clarendon Laboratory  
Wolfson College  
University of Oxford

Supervised by  
Prof. Ian. A. Walmsley

A thesis submitted for the degree of

*Doctor of Philosophy*

Hilary term 2011



To my parents



## Acknowledgements

First of all I would like to thank my supervisor Prof. Ian Walmsley, for the continuous support I received from him during my DPhil. Ian was a great advisor – I feel very fortunate to be one of his students!

Second, I would like to thank Dr. Joshua Nunn for his extraordinary patience with respect to the many theoretical discussions we had. They helped a lot when experimental progress was waiting to be made.

Then I would like to thank Dr. Virginia Lorenz, who I spent a lot of time with in the lab at the beginning of my DPhil. From her I learned how to work and survive in a dark, windowless laser lab, and together we faced the harsher times of the experiment, where nothing seemed to work. Thanks to Prof. Taylor and Dan Collins, who I collaborated with in my first year and from whom I learned about quantum dots and how to conduct cryogenic superconducting experiments.

I gratefully acknowledge the doctoral scholarship I received from the European Union under the framework six research training network ‘EMALI’. Especially I would like to thank Prof. Klaas Bergmann who coordinated the network and supported us ‘young researchers’ with great enthusiasm, advice and foresight. It was a unique opportunity to participate in this research network where I was able to establish strong social and scientific bonds with fantastic people across Europe.

Then I would like to thank my dear fellow colleagues from the Ultrafast group, particularly Philip Bustard, Dr. Dave McCabe, Duncan England and Tim Bartley, who besides the sometimes stressful academic life introduced me to the relaxed, cheerful British side of things.

I am grateful to Dr. Adam Wyatt, Dr. Dane Austin and Tobias Witting, who helped me on many occasions with programming issues.

My family in Germany, who supported and motivated me not just from a distance, but also by visiting me regularly in Oxford. Without them I would not be who I am and where I am today. Thank you!

I would like to thank my dear friend Dr. Philipp Ridha in Switzerland, who strongly supported me during my DPhil and always was very receptive to both pleasant and unpleasant discussions, my former housemates from 354 Cowley Road and ‘the orchard’, especially Jeremie Becker and Gunnar Langfahl-Klabes, who contributed an important part to my social life in Oxford.

Rob Harris from the machine shop, who taught me how to operate drilling and milling machines – skills, which contributed significantly to the experimental success of the project.

I am also very grateful to Richard Harley, who made it possible for me to live at ‘the orchard’ in Old Marston during my last months in Oxford. There, I was able to write my DPhil thesis in peace and harmony full of muse and inspiration while overlooking one of nature’s beautiful playgrounds.

# Abstract

This thesis is about the experimental implementation of a high-speed and robust quantum memory for light. A novel far off-resonant Raman approach to ensemble-based quantum memories in a room-temperature environment is developed and demonstrated. Storage and retrieval of sub-nanosecond, weak coherent light pulses at the single-photon-level with total efficiencies exceeding 30% and storage times of up to 4  $\mu$ s are achieved. The coherence of the memory is shown by directly interfering a copy of the incident signal with the retrieved signal from the memory. The unconditional noise floor of the memory is found to be low enough to operate the memory in the quantum regime at room temperature. Multiple readout of a single stored excitation is demonstrated, suggesting that 100% readout is possible in different temporal modes. Furthermore, first results regarding the storage and retrieval of polarisation encoded qubits are obtained. This and the memory's ability to operate in the quantum regime at room temperature with a low unconditional noise floor illustrate its potential usefulness for real world applications.



## Publications

1. **K. F. Reim**, P. Michelberger, K. C. Lee, J. Nunn, N. K. Langford & I. A. Walmsley. Single-photon-level quantum memory at room temperature. [arXiv:1010.3975](https://arxiv.org/abs/1010.3975) (2010).
2. **K. F. Reim**, J. Nunn, V. O. Lorenz, B. J. Sussman, K. C. Lee, N. K. Langford, D. Jaksch & I. A. Walmsley. Towards high-speed optical quantum memories *Nature photonics* **4**, 218-221 (2010).
3. J. Nunn, U. Dorner, P. Michelberger, **K. F. Reim**, K.C. Lee, N. K. Langford, I. A. Walmsley & D. Jaksch. Quantum memory in an optical lattice *Phys. Rev. A* **82**, 022327 (2010).
4. K. C. Lee, B. J. Sussman, J. Nunn, V. O. Lorenz, **K. Reim**, D. Jaksch, I. A. Walmsley, P. Spizzirri & S. Prawer. Comparing phonon dephasing lifetimes in diamond using Transient Coherent Ultrafast Phonon Spectroscopy *Diamond related materials* **19**, 10-1289-1295 (2010).
5. J. Nunn, **K. Reim**, K. C. Lee, V. O. Lorenz, B. J. Sussman, I. A. Walmsley & D. Jaksch. Multimode memories in atomic ensembles *Phys. Rev. Lett.* **101**, 260502 (2008).
6. K. Surmacz, J. Nunn, **K. Reim**, K.C. Lee, V. O. Lorenz, B. Sussman, I. A. Walmsley & D. Jaksch. Efficient spatially resolved quantum memory *Phys. Rev. A* **78**, 033806 (2008).



# Contents

<b>1</b>	<b>Introduction</b>	<b>1</b>
1.1	Motivation . . . . .	1
1.2	Quantum memories overview . . . . .	5
1.2.1	EIT . . . . .	5
1.2.2	CRIB . . . . .	7
1.2.3	AFC . . . . .	9
1.2.4	Raman . . . . .	11
<b>2</b>	<b>Raman Memory Theory</b>	<b>15</b>
2.1	General memory interaction picture . . . . .	15
2.1.1	Optical field description . . . . .	16
2.1.2	Atomic response . . . . .	18
2.2	Light-matter interaction Hamiltonian . . . . .	18
2.3	Equations of motion for atomic coherences . . . . .	20
2.4	Light propagation . . . . .	21
2.5	Raman memory equations . . . . .	22
2.6	Raman regime and adiabatic limit . . . . .	23
2.7	Raman storage, retrieval & efficiency . . . . .	24

---

2.8	Optical depth . . . . .	26
2.9	Raman memory benefits . . . . .	26
2.9.1	Bandwidth . . . . .	27
2.9.2	Robustness, compatibility & integrability . . . . .	29
2.10	Decoherence & Noise . . . . .	30
2.10.1	Magnetic dephasing . . . . .	31
2.10.2	Stimulated Raman scattering (SRS) noise model . . . . .	33
<b>3</b>	<b>Caesium experiment</b>	<b>39</b>
3.1	Electronic configuration – $\Lambda$ -level structure . . . . .	39
3.2	Vapour cell and heating system . . . . .	41
3.2.1	Cell setup . . . . .	42
3.2.2	Atoms and buffergas . . . . .	43
3.2.3	Caesium absorption profile . . . . .	44
3.3	Laser systems . . . . .	45
3.3.1	Tsunami Ti:Sapph . . . . .	46
3.3.2	External cavity diode laser (ECDL) . . . . .	47
3.3.2.1	General operation . . . . .	47
3.3.2.2	Switching the diode laser . . . . .	48
3.4	Signal field generation . . . . .	49
3.4.1	Raman cell approach . . . . .	51
3.5	Spectrometer . . . . .	52
3.5.1	Electro optic modulator (EOM) . . . . .	55
3.5.2	EOM operation & switching . . . . .	57
3.5.3	First observation of sidebands . . . . .	57

---

3.5.4	Selective sideband detection with spectrometer . . . . .	59
3.6	Double $\Lambda$ -level system issue . . . . .	60
3.7	Filtering . . . . .	61
3.7.1	Lyot filters . . . . .	62
3.7.2	Etalons . . . . .	64
3.7.3	Polarisation . . . . .	67
3.8	Pockels cell . . . . .	68
3.9	Detection system . . . . .	71
3.9.1	Andor camera . . . . .	72
3.9.2	Webcam . . . . .	72
3.9.3	Fast photodiode . . . . .	73
3.9.4	Fast avalanche photo diode . . . . .	73
3.10	Optical pumping . . . . .	74
3.10.1	Fluorescence measurements . . . . .	77
3.10.2	Absorption/Transmission measurements . . . . .	78
3.11	Polarising beam displacers . . . . .	80
<b>4</b>	<b>Raman memory realisation</b>	<b>83</b>
4.1	Influence of optical pumping on sidebands . . . . .	83
4.2	Temporal pulse overlap . . . . .	87
4.2.1	Interference fringes on camera . . . . .	88
4.2.2	Direct temporal measurements on a fast photodiode . . . . .	91
4.3	Observation of Raman gain and absorption . . . . .	93
4.3.1	Gain and absorption on red and blue sideband . . . . .	93
4.3.2	Gain and absorption on a single sideband . . . . .	97

---

4.3.3	Gain and absorption power study . . . . .	99
4.3.4	Conclusion of Raman gain and absorption studies . . . . .	101
4.4	Experimental setup . . . . .	102
4.5	Results . . . . .	104
4.5.1	First observation of storage and retrieval . . . . .	104
4.5.2	Memory parameter-space investigation . . . . .	107
4.5.2.1	Vapour cell temperature run . . . . .	108
4.5.2.2	Control field pulse energy dependence . . . . .	109
4.5.2.3	Signal field power run . . . . .	113
4.5.3	Storage and retrieval of gigahertz bandwidth . . . . .	114
4.5.4	Verification of the memory coherence . . . . .	117
4.6	Improving the memory . . . . .	123
4.6.1	Increasing the memory efficiency . . . . .	123
4.6.2	Storage time enhancement & dephasing . . . . .	125
4.6.2.1	First memory decay measurements . . . . .	125
4.6.2.2	Extension of memory lifetime by magnetic shielding	127
4.6.2.3	Dephasing caused by the diode laser . . . . .	129
4.6.2.4	Memory with magnetic shielding and diode laser off	130
4.6.2.5	Magnetic rephasing . . . . .	132
4.7	Multiple readout . . . . .	134
4.7.1	Complete readout – ‘Crazy train’ . . . . .	135
4.7.2	Balanced and pyramid readout . . . . .	137
<b>5</b>	<b>Single-photon-level experiments</b>	<b>141</b>
5.1	Technical upgrades . . . . .	142

---

5.1.1	Improved filtering . . . . .	142
5.1.2	Single Photon counting modules . . . . .	143
5.1.3	FPGA . . . . .	143
5.1.4	Time-to-amplitude converter . . . . .	144
5.1.5	Multi-channel analyser . . . . .	145
5.2	Results . . . . .	146
5.2.1	Single-photon-level data & fluorescence noise . . . . .	146
5.2.2	Instantaneous noise . . . . .	149
5.2.3	Origins of instantaneous noise . . . . .	151
<b>6</b>	<b>Polarisation encoded qubit memory</b>	<b>155</b>
6.1	Qubit memory — experimental setup . . . . .	156
6.2	Quantum process tomography . . . . .	159
6.3	Results . . . . .	162
6.3.1	Process tomography with 400 ns storage time . . . . .	163
6.3.2	Process tomography with 12.5 ns storage time . . . . .	165
6.3.3	Interferometer phase fluctuations . . . . .	166
6.3.4	Most recent QPT results . . . . .	170
6.3.5	Alternatives for qubit storage . . . . .	172
<b>7</b>	<b>Conclusions</b>	<b>175</b>
<b>8</b>	<b>Outlook</b>	<b>177</b>



# List of Figures

1.1	Global quantum information network . . . . .	3
1.2	EIT protocol . . . . .	6
1.3	CRIB protocol . . . . .	8
1.4	AFC protocol . . . . .	10
1.5	Raman scattering . . . . .	12
2.1	General Raman memory interaction . . . . .	16
2.2	Virtual Raman resonance . . . . .	27
3.1	Electronic structure of caesium ( $\text{Cs}^{133}$ ) . . . . .	40
3.2	Schematic of the caesium vapour cell . . . . .	41
3.3	Caesium $\text{D}_2$ line absorption spectrum . . . . .	44
3.4	Principle of an acousto-optic modulator (AOM) . . . . .	49
3.5	Signal field generation and $\Lambda$ -level scheme . . . . .	50
3.6	High resolution grating spectrometer . . . . .	53
3.7	Spectrometer image of two laser beams separated by 9.2 GHz . . . . .	54
3.8	Efficiency of electro optic modulator (EOM) . . . . .	56
3.9	Spatial beam profiler . . . . .	58
3.10	Spectrometer image of sidebands ( $m = 1$ ), carrier and diode laser . . . . .	59

---

3.11	Double $\Lambda$ -level system . . . . .	60
3.12	Lyot filter schematic . . . . .	62
3.13	Fabry Perot etalon schematic . . . . .	64
3.14	Pockels cell schematic . . . . .	70
3.15	Optical pumping sequence . . . . .	75
3.16	First optical pumping setup and data . . . . .	77
3.17	Second optical pumping experiment and data . . . . .	79
3.18	Polarising beam displacer . . . . .	80
4.1	Optical pumping effects on sidebands . . . . .	84
4.2	Sideband absorption study . . . . .	86
4.3	Experimental pulse overlap verification . . . . .	87
4.4	Spatially measured interference of signal and control field . . . . .	89
4.5	Temporal beam profiles of signal and control field . . . . .	91
4.6	Raman gain and absorption scheme and setup . . . . .	94
4.7	Raman gain and absorption on both sidebands . . . . .	96
4.8	Raman gain and absorption on a single sideband . . . . .	97
4.9	Raman gain and absorption dependence on control field pulse energy . . . . .	100
4.10	Quantum memory setup and $\Lambda$ -level scheme . . . . .	103
4.11	First observed memory operation . . . . .	105
4.12	Temperature dependence of the optical memory . . . . .	108
4.13	Optical storage and retrieval in detail . . . . .	110
4.14	Memory efficiency dependence of control field pulse energy . . . . .	111
4.15	Detected power vs. signal field intensity . . . . .	113
4.16	Storage and retrieval of pulses with GHz bandwidth . . . . .	115
4.17	Memory coherence test interferometer setup . . . . .	118

---

4.18	Mach-Zender type interferometer characterisation . . . . .	119
4.19	Memory coherence data . . . . .	121
4.20	Increased memory efficiency . . . . .	124
4.21	Memory lifetime without magnetic shielding . . . . .	126
4.22	Memory lifetime with magnetic shielding and diode laser off for 900 ns . . . . .	128
4.23	Effect of diode laser on memory efficiency . . . . .	130
4.24	Memory lifetime with magnetic shielding and diode laser perma- nently off . . . . .	131
4.25	Magnetic rephasing . . . . .	133
4.26	Complete readout . . . . .	136
4.27	Balanced and pyramid readout . . . . .	138
5.1	Single photon level experiments . . . . .	145
5.2	Single photon level storage and retrieval . . . . .	147
5.3	Single photon level data and instantaneous noise . . . . .	149
5.4	Spontaneous Raman scattering (SRS) noise . . . . .	152
6.1	Qubit memory experimental setup and $\Lambda$ -level system . . . . .	156
6.2	Process tomography at 400 ns . . . . .	163
6.3	Process tomography at 12.5 ns . . . . .	165
6.4	Polarisation interferometer fluctuations for different QPT settings	167
6.5	Polarisation interferometer fluctuations vs. cell temperature and time . . . . .	169
6.6	Stable QPT measurements . . . . .	171
6.7	Zeeman qubit memory . . . . .	172



# Chapter 1

## Introduction

### 1.1 Motivation

The word ‘quantum’ is derived from the Latin word ‘quantus’, for ‘how much’. Max Planck used it in 1901 to describe distinct portions of matter and electricity, ‘quanta’<sup>[1]</sup>, and Albert Einstein suggested in 1905, that light is composed of quanta of light, ‘Lichtquanta’<sup>[2]</sup>. As these early incarnations of this word indicate, the research field *quantum optics* deals mainly with the interplay between light and matter at its most fundamental level.

The foundations of quantum optics as a research field can therefore be dated back to the early years of the 20th century when Max Planck postulated his quantised description of the black body radiation<sup>[1,3]</sup> and Niels Bohr demonstrated that atoms only emit light containing discrete amounts of energy<sup>[4]</sup>.

In the 1960’s, quite a long time after these first fundamental findings, the invention of the laser<sup>[5]</sup> posed the next milestone. This discovery turned out to be of major importance for many of today’s research fields and created and

shaped our global information technology age<sup>[6]</sup>.

In the late 1970's Jeff Kimble and co-workers demonstrated the first experiment that required a quantum description for light<sup>[7]</sup>: a single atom emitting a single photon<sup>1</sup> at a time. Such photons play a major role in today's quantum information science, which deals with the understanding of quantum effects in light and matter, their control and manipulation

There have been tremendous advances over the past 20 years in the fields of coherent control of atomic systems, generating laser pulses, laser cooling of atoms, single photon generation and manipulation, ion trapping, BECs, etc.<sup>[8-14]</sup>. All this research has led to a better understanding of our natural environment and also to the hope that we will ultimately be able to control and use this fantastic toolbox that quantum mechanics provides to build real world devices which will be useful.

One of quantum information science's visions is the replacement of our current, classical information technology architecture with a quantum information technology architecture that offers more security and vastly superior computational power compared to classical systems. Imagine a global quantum network, where quantum information is exchanged on an intercontinental scale<sup>[15]</sup>, as illustrated in Figure 1.1. Quantum information is generated and processed in local nodes using future quantum computers<sup>[16-19]</sup>, and then shared with people on different continents via completely secure quantum channels<sup>[20]</sup>, enabled by quantum repeaters<sup>[21-23]</sup>.

Due to this ever increasing global information transfer, there is growing demand for secure communication technology, such as could be provided by photonic

---

<sup>1</sup>A photon or light particle, is the quantum of electromagnetic radiation and the basic unit of light.

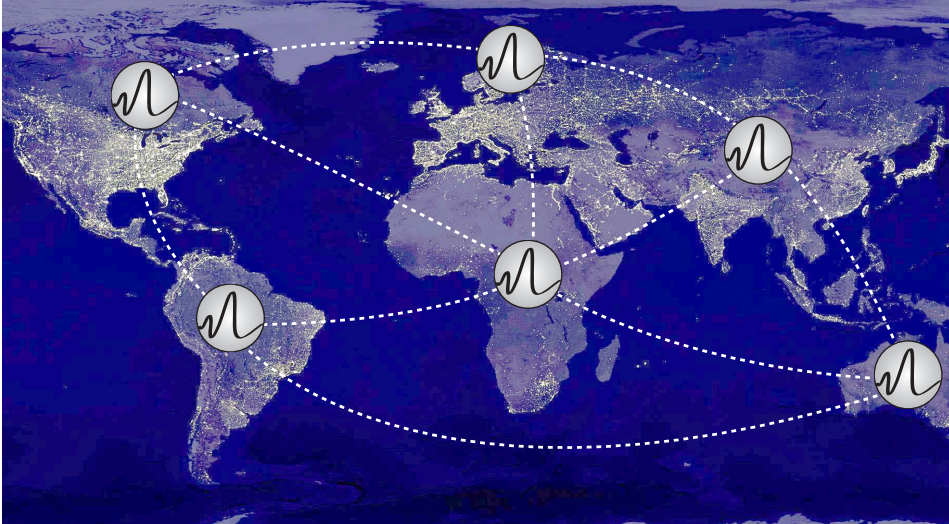


**Figure 1.1:** Earth at night with metropolitan areas (lights) and global quantum network with local nodes (wave symbols) and intercontinental links (dashed lines).

quantum communication networks<sup>[20]</sup>. Currently, the biggest challenge for such networks is distance. Over short distances, photons, interacting only weakly with their environment, easily and reliably carry quantum information without much decoherence, but intercontinental quantum communication will require quantum repeaters embedded in potentially isolated locations, because transmission decreases exponentially with distance<sup>[15,23]</sup>.

In general, these repeater systems will require some sort of quantum memory, a coherent device that interfaces between light and matter, in order to function properly. Single photons – or so called flying qubits<sup>1</sup>, get controllably mapped into an atomic system and at a later point in time are transformed back into a single photon. Also, locally stored quantum information can be processed by applying quantum logic gates<sup>[12,24–27]</sup> or error-corrected by applying error correction

---

<sup>1</sup>A qubit or quantum bit is a unit of quantum information, e.g. polarisation encoded in a photon.

algorithms<sup>[28–32]</sup> that compensate for decoherence in quantum systems.

To be truly practical, a quantum memory needs to fulfil several requirements such as having a large bandwidth<sup>[33]</sup>, a high memory efficiency<sup>[34–36]</sup>, a long storage time<sup>[37,38]</sup> and multimode capacity<sup>[39,40]</sup> as well as being able to operate in the quantum regime. For ‘real world’ applications, another crucial feature of such memories will be ease of operation near room temperature. Ideally they should not need complex cryogenic or laser cooling apparatus, so that they are suitable for deployment in harsh environments such as transatlantic communication links.

Warm atomic vapours of alkali atoms such as rubidium and caesium are potentially excellent storage media. At room temperature they provide enough optical depths for achieving a strong atom-photon interaction in a centimeter-scale vapour cell<sup>[41–44]</sup>. Recent experimental advances point towards the miniaturisation of vapour cells<sup>[45]</sup> and integrated on-chip hollow core waveguide structures<sup>[46]</sup> that can be mass-produced, are robust, and easy to operate<sup>[33]</sup>.

Furthermore, highly efficient quantum memories could be used for building deterministic single photon sources<sup>[47–49]</sup>, crucial components in a future quantum information architecture, where on demand photons are required.

As we have seen *quantum memories* will play an important role in future quantum information technology networks, enabling quantum information storage, local processing, and its subsequent exchange. Quantum memories will have a huge impact on quantum information science and the realisation of on-chip integrated technology might bring us a step closer to a global high-speed quantum information network hugely benefiting mankind.

## 1.2 Quantum memories overview

Quantum memories are based on the controllable interaction between light and matter. Over the last few years different approaches have been invented to achieve this goal. This thesis focusses on ensemble based, *absorptive* quantum memories, i.e. memories that work on the principle of absorption of a quantum state of light and its coherent storage in a long-lived metastable state of the absorber. The memory interaction is reversible and the controlled readout of the stored excitation leads to the re-emission of the original quantum state of light. Ensemble based memories based on *continuous variables*<sup>[50–52]</sup>, an approach introduced by Eugene Polzik and co-workers, provide another route to quantum information storage, which is not going to be discussed in greater detail here. However, further information on this topic can be found in the review article by Klemens Hammerer<sup>[53]</sup>. Ensemble based, absorptive quantum memories can be categorised in the following way.

### 1.2.1 EIT

The most established absorptive quantum memory is based on *electromagnetically induced transparency* (EIT), a technique by which an optically thick medium is rendered transparent. The effect was first observed by Boller et *al.* in 1991<sup>[54]</sup>, but at that time was not used for constructing a quantum memory. The transparency results from destructive interference of the dressed states created by applying a strong coupling laser between a ground state of an atom, e.g. state  $|3\rangle$  and its excited state  $|2\rangle$  (See Figure 1.2)<sup>[55]</sup>. Within this transparency window the dispersion of the system is changed in such a way that the group velocity of a

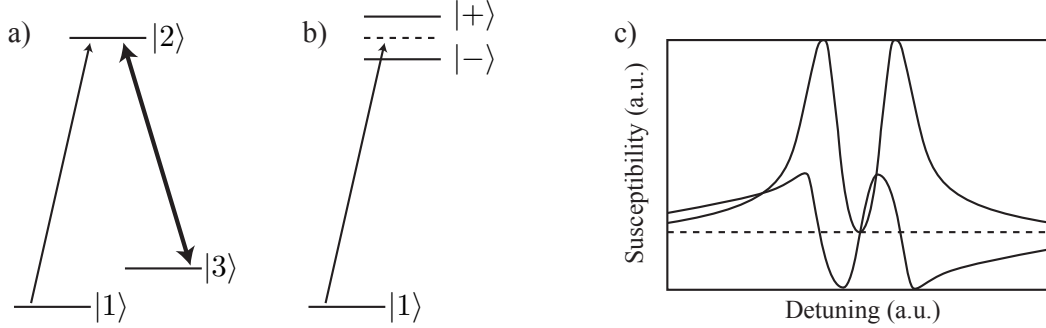


**Figure 1.2:** EIT protocol. **(a)** Weak signal field (light arrow) and strong coupling laser (thick arrow). **(b)** The coupling laser creates the dressed states  $|+\rangle$  and  $|-\rangle$ . The signal field is tuned inside the transparency window. **(c)** Imaginary and real part of the susceptibility, indicating absorption and the refractive index of a probe field in the presence of a strong coupling field.

probe beam is reduced drastically — measured values as low as  $17 \text{ ms}^{-1}$  have been reported in ultra-cold experiments<sup>[56]</sup>.

In order to use EIT to bring a signal pulse (the pulse one would like to store) to a complete halt and store it, the transparency window needs to be adiabatically closed; therefore the coupling laser needs to be turned off adiabatically. The whole procedure is as follows. A signal pulse, tuned to the center of the transparency window, enters the storage medium, e.g. an atomic ensemble, and gets slowed down, depending on how strongly the dispersion is altered by the control field. The signal field gets spatially compressed until it completely fits inside the atomic ensemble and then the control field is slowly attenuated and switched off such that the shape and quantum state of the signal field are completely mapped onto a collective state in the storage medium. This method was discovered by Mikhail Lukin and Michael Fleischauer in 2000<sup>[57]</sup>, almost a decade after EIT was observed for the first time. Since then there have been various experimental demonstrations in cold atomic ensembles<sup>[58,59]</sup>, single and multi-

ple trapped atoms in cavities<sup>[47,60,61]</sup>, solid states systems<sup>[62,63]</sup> and warm atomic ensembles<sup>[41,64]</sup>. The advantages of this storage mechanism are that the EIT protocol is well understood and that the pulse energies required for opening the transparency window can be easily delivered by commercially available, relatively low-cost diode lasers. The protocol's disadvantages lie in its on-resonant character. Operating close to resonance leads to collision-induced fluorescence noise that is particularly disturbing when operating at the single photon level<sup>[44,64,65]</sup>. Furthermore it is difficult to achieve high memory bandwidths in EIT memories, because large (broadband) transparency windows require extremely large Rabi frequencies. Most experiments operate in the MHz regime with  $\mu\text{s}$  duration laser pulses<sup>[41,43,63–65]</sup>.

### 1.2.2 CRIB

*Controlled reversible inhomogeneous broadening* (CRIB)<sup>[66–69]</sup> is a photon echo technique that makes use of an external gradient electric or magnetic field to artificially broaden the atomic resonance. Each individual atom still has a narrow resonance but as the external field experienced at different locations varies, the entire ensemble exhibits an inhomogeneous broadening that is much larger than an atomic linewidth (see Figure 1.3).

Due to this broadening this approach is capable of storing photons with a bandwidth exceeding the natural linewidth of the atoms. During the storage process an external field broadens the resonance and the signal field gets absorbed by the atomic ensemble. The duration of the signal field is short compared to the excited state lifetime<sup>1</sup> because otherwise one would lose the signal field's in-

---

<sup>1</sup>The time during which the excited state population of an atom drops by  $1/e$

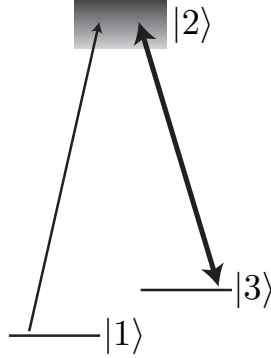


**Figure 1.3:** CRIB protocol. A signal photon (weak arrow) is absorbed resonantly into the artificially broadened excited state  $|2\rangle$ . The strong control field transfers the excited atom to the storage state  $|3\rangle$ . Upon retrieval, the process sequence happens in reversed order as well as the reversal of the artificially applied broadening.

formation due to spontaneous emission. After absorption of the signal field the phases of the excited atomic dipoles start precessing at different frequencies due to the external field gradient. This means they get out of phase relative to each other. A strong control field then ‘freezes’ their motion and transfers the excited state population into a long-lived storage state  $|3\rangle$  where the initial signal field information is stored. Upon retrieval, a strong control pulse ‘unfreezes’ the stored information and lifts the atoms back into the excited state. In order to recover the initial signal field, a reversed external broadening needs to be applied such that all the atoms precess in the opposite way compared to during the storage event. This causes a re-phasing of the atomic spins and when they are all re-aligned such that they mirror the configuration at the time of absorption, they re-emit a photon echo. In the last few years there have been various experimental demonstrations of this storage mechanism mainly carried out in rare earth ion doped crystals<sup>[70–73]</sup>, but also in hot vapours<sup>[74]</sup>. The advantage of the CRIB protocol is its multimode character, which enables the storage of multiple

frequencies at the same time. Its disadvantage lies in the preparation of the interaction medium. CRIB was designed for rare earth ion doped crystals, which have an in-homogeneously broadened linewidth due to the doping of the solid state system. In order to achieve a controlled broadening of the absorbers, the broad inhomogeneous ensemble needs to be narrowed drastically by optical pumping, such that a controlled broadening, caused by an external gradient field applied to the narrow absorption line, can be achieved. Thereby a lot of absorbers are lost and the optical density of the interaction medium is reduced, making it difficult to achieve high memory efficiencies.

### 1.2.3 AFC

The *atomic frequency comb* (AFC) is the most recent of the proposed quantum memory schemes. It was introduced by Afzelius *et al.*<sup>[75]</sup> in Geneva and is based on the CRIB scheme. The AFC protocol increases the memory's multimode capacity, i.e. the possibility to store different frequency modes at the same time, significantly<sup>[39,75]</sup>. An atomic frequency comb can be thought of as an ensemble based system where the excited state is spread into equally spaced atomic absorption lines, as can be seen in Figure 1.4. Due to this frequency-spread structure it is possible to store bandwidths greater than the atomic linewidth. The absorption process and the transfer to a long-lived storage state is similar to the one described above in the CRIB case. The special feature of the AFC protocol comes into play when the signal is retrieved. After the application of a control pulse, one would have to apply a reversed broadening in the CRIB case in order to re-phase the atomic spins and obtain a retrieved signal, whereas in the AFC case the discrete structure of the excited states itself causes periodic re-phrasings

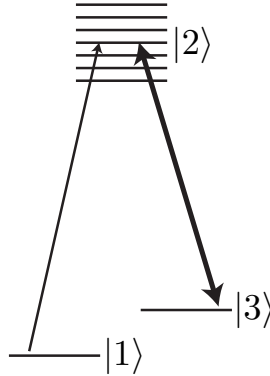


**Figure 1.4:** AFC protocol. A broadband signal photon (light arrow) is absorbed by the atomic frequency comb’s discrete teeth structure  $|2\rangle$ . The excitation is then transferred to state  $|3\rangle$  by a strong control pulse (thick arrow). Upon retrieval, the process is reversed and after a rephasing of the atomic dipoles, the retrieved signal emerges.

of the atomic spins. They occur with periodicity of  $2\pi/\Delta$ , where  $\Delta$  is the spacing between the frequency comb teeth, and each re-phasing results in a photon-echo type coherent retrieval. The absorption between the comb teeth never vanishes completely such that a broadband pulse can be absorbed in a coherent fashion. The control field, transferring the excited state population to a long-lived storage state, must be broadband too and ideally spans the whole range of the atomic frequency comb. Experimentally preparing such an absorption structure is a challenge in itself. Rare earth ion doped crystals are the proposed atomic system<sup>[75]</sup>, which need to be modified and shaped by optical pumping to create an AFC structure. Recently there were first experimental demonstrations of this new memory protocol<sup>[76–78]</sup>. The AFC protocol’s biggest advantage is its large multimode capacity<sup>[75]</sup>, which is significantly bigger than in any other memory scheme. Many different frequency modes can be stored and retrieved at the same time<sup>[76]</sup>, making this memory scheme very useful for quantum repeater networks.

Basically the amount of entanglement swapping trials can be reduced and the speed with which the quantum channel is established can be enhanced. Its disadvantage is the procedure of creating the atomic frequency comb. It is a non-trivial process and requires complicated preparation steps, where lots of atoms are shelved away (excluded) from the genuinely broad absorption spectrum of the rare earth ion doped crystal<sup>[76]</sup>. This is similar to the CRIB case, but not as bad, because the number of the teeth in the AFC structure is a lot larger than the single narrow (but artificially broadened) absorption line used in the CRIB memory.

#### 1.2.4 Raman

Lastly, I would like to describe the Raman memory scheme, which was recently proposed theoretically<sup>[79–81]</sup>. The experimental realisation of this interaction mechanism is the heart of my doctoral thesis, which is the first experimental demonstration of coherent storage and retrieval of broadband light pulses using this Raman interaction.

Historically, Raman scattering dates back to the early 20th century. In 1928, Chandrasekhara V. Raman discovered this scattering effect<sup>[82]</sup>, which was named after him. In 1930 he received the Nobel Prize for Physics for his discovery, which in the following decades led to many applications like Raman spectroscopy for material analysis or industrial sensing and became of importance also in the research field of quantum optics.

The importance of the Raman effect lies in the inelastic nature of the scattering process. Light is scattered by a material excitation, which allows for gaining insight to the electronic, vibrational or rotational state of an observed system. It

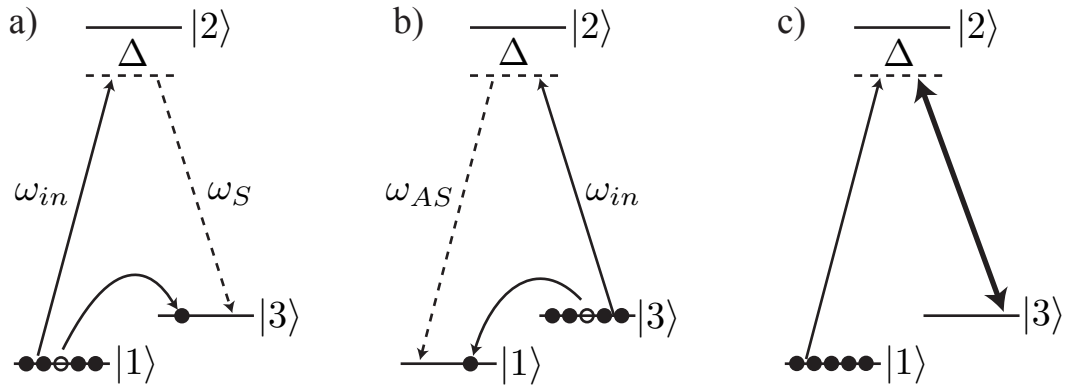


**Figure 1.5:** Raman scattering. (a) Stokes scattering. The Raman scattered photon has less energy than the incoming photon (b) Anti-Stokes scattering. The scattered photon has more energy than incoming photon (c) Raman memory. Two input fields, a weak signal and a control control field cause a two photon Raman transition to take place and coherently excite the atomic medium.

is an instantaneous, off-resonant two-photon process that can be schematically illustrated in a  $\Lambda$ -level system like the one displayed in Figure 1.5. A photon of frequency  $\omega_{in}$  is incident on the atom, producing or annihilating an excitation in the medium with energy  $\omega_{13}$  and producing a frequency-shifted photon. Red-shifted photons ( $\omega_S = \omega_{in} - \omega_{13}$ ) are called *Stokes* photons (see Figure 1.5 (a)), and blue-shifted photons ( $\omega_{AS} = \omega_{in} + \omega_{13}$ ) are called *anti-Stokes* photons (see Figure 1.5 (b)). Both optical fields have a common detuning  $\Delta$  from the atomic resonance, enabling the off-resonant two-photon interaction. Generally, Raman scattering has a very low probability to take place, because its scattering cross section is very small. For a centimeter-sized sample the typical probability for scattering a Stokes photon is around one in a million<sup>[83]</sup>.

This of course is not suitable for a quantum memory where one would like to produce on demand storage and retrieval of quantum information. Therefore, instead of waiting for a spontaneous scattering event to take place one sends in two

fields with common detuning, the signal and the control field, at the same time (see Figure 1.5). The strong control field dresses state  $|3\rangle$  and creates a virtual resonance into which the signal field is absorbed. After the fields have passed the virtual resonance collapses back to state  $|3\rangle$ , which now contains one excited atom from the ground state  $|1\rangle$ . One does not know which of the atoms contributed to this transition and therefore the excitation is called a *collective excitation*. Upon retrieval, the interaction is reversed and the application of a strong read pulse triggers a coherent read-out event producing a retrieved photon, identical to the one initially stored. Further details concerning the interaction will be discussed in chapter 2.

The interaction looks very similar to the EIT case discussed in Section 1.2.1. The difference, however, is that in the EIT case the signal field is tuned right in between the dressed states and is usually very close to the bare atomic resonance. In the Raman case, the signal field is tuned right into one of the artificially created resonances far away from the bare atomic resonance. The interaction with the atoms is different compared to EIT, where the signal is slowed down due to the modified dispersion. Here the signal field does not experience any slowing effects, in fact it is a true absorption process with superluminal group velocity.

There are some benefits compared to the other memory schemes described above that motivated us to study this far off-resonant interaction for storing single photons. The primary benefit is the Raman memory's capability to store broadband photons. A large bandwidth means in turn temporally short photons, which is advantageous in future quantum networks regarding data transfer rates or processors speeds. Furthermore, as will be demonstrated throughout this thesis, the Raman memory's large detuning makes the memory robust to inho-

mogeneous broadening of the atomic system and allows for single-photon-level operation at room temperature. This is an important factor, if one bears in mind that there are strong efforts in the research community to make quantum information technology devices scalable and integrable, such that one can build a real quantum information technology infrastructure.

# Chapter 2

## Raman Memory Theory

In this chapter we develop the necessary theoretical background to understand the interaction between light and matter. Most of the theoretical work describing the interaction and evolution of light fields and atomic systems, approximated as two-level systems, can be found in standard text books about atomic physics and quantum optics<sup>[83,84]</sup>. A detailed quantum field theory for spontaneous Raman scattering and the onset of stimulated Raman scattering was developed in the early 80's<sup>[85]</sup> by Mostowski *et al.* and reviewed by Raymer and Walmsley in 1990<sup>[86]</sup>. The theory for a Raman memory was first laid out by Kozhokin *et al.* in 2000<sup>[81]</sup> and then extended independently by Gorshkov and Nunn to include the treatment for storage and retrieval of a single photon in 2007<sup>[79,80]</sup>.

### 2.1 General memory interaction picture

Two essential ingredients are required in order build a quantum memory. The first is the quantum light that one would like to store and the second is an interaction medium that acts as a storage and retrieval interface. In our case

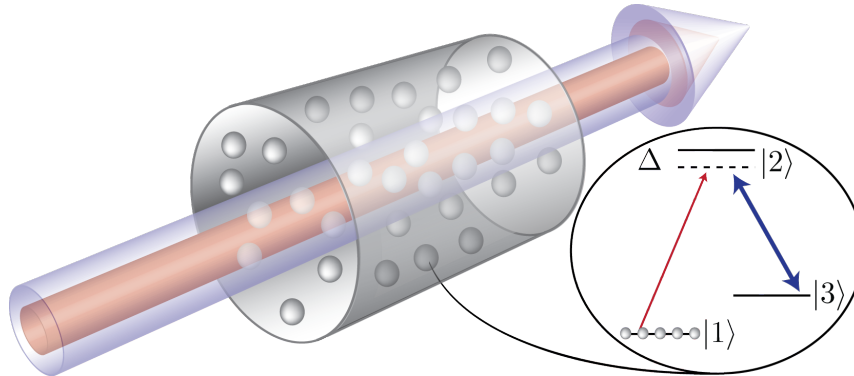


**Figure 2.1:** General Raman memory interaction. Atomic vapour cell containing a single species of atoms, e.g. rubidium or caesium atoms. The red beam is the signal field that shall be stored and the blue beam is the control field that mediates the interaction. Inset: Atomic structure illustrated as  $\Lambda$ -level diagram which is prepared in the ground state  $|1\rangle$ . The storage state  $|3\rangle$  is empty. The blue arrow indicates the control field, the red arrow indicates the signal field. Both fields are commonly detuned from the excited state  $|2\rangle$  by the detuning  $\Delta$ .

we consider warm atomic ensembles<sup>1</sup> as illustrated in Figure 2.1. The signal (red) and the control field (blue) overlap inside the vapour cell and address the atoms contained in their mode volume<sup>2</sup> via the electric dipole interaction. The interaction Hamiltonian can be written as  $H_{ED} = -\mathbf{E} \cdot \mathbf{d}$ , where  $\mathbf{E}$  is the electric field of the light pulses and  $\mathbf{d}$  is the dipole moment of the addressed transition in the atoms.

### 2.1.1 Optical field description

The optical fields introduced in Section 2.1 are composed of a weak signal field and a strong classical control field both directed and collimated along the atomic vapour cell as shown in Figure 2.1. Therefore, we use a scalar model for describing the light fields and atomic responses and disregard divergence. Due to its

<sup>1</sup>For example rubidium or caesium at room temperature in a vapour cell

<sup>2</sup>Volume of the laser beam

strength, the control field is not changed by the interaction with the atoms. It can be written as

$$\tilde{E}_c(t, z) = E_c(t, z)e^{i\omega_c(t-z/c)} + c.c., \quad (2.1)$$

where  $\omega_c$  is the angular frequency and  $E_c(t, z)$  is the slowly varying envelope.

The signal field needs to be treated quantum mechanically because it usually consists of a single photon only. The signal field operator can be expressed as<sup>[87]</sup>

$$\tilde{E}_s(z, t) = i \int g(\omega)a(\omega, t)e^{-i\omega z/c}d\omega + h.c., \quad (2.2)$$

where  $g(\omega) = \sqrt{\hbar\omega/4\pi\epsilon_0c\mathcal{A}}$  is the mode amplitude with the transverse area  $\mathcal{A}$  and  $a(\omega, t)$  is the annihilation operator for a signal photon in the Heisenberg picture with frequency  $\omega$  and an explicit time dependence  $t$ . In order to rewrite the signal field in a slowly varying envelope picture as was done for the control field in (2.1), we need to assume that the bandwidth of the signal field is much smaller than its angular frequency  $\omega_s$ . Then only terms close to  $\omega_s$  become important. With  $g(\omega) \rightarrow g(\omega_s)$  and integrating over  $\omega$ , we can rewrite equation (2.2) as

$$\tilde{E}_s(t, z) = ig_s A(t, z)e^{i\omega_s(t-z/c)} + h.c., \quad (2.3)$$

where  $g_s = \sqrt{2\pi}g(\omega_s)$  and  $A$  is the slowly varying time-domain annihilation operator given by

$$A(t, z) = e^{-i\omega_s(t-z/c)} \times \frac{1}{\sqrt{2\pi}} \int a(\omega, t)e^{-i\omega z/c}d\omega. \quad (2.4)$$

Its function in free space can be pictured as the annihilation of a signal photon in a spatio-temporal mode at time  $t$  and position  $z$ .

### 2.1.2 Atomic response

The atoms respond to the impinging electric fields according to their electronic structure. In our simplified three level system (see Figure 2.1), the three states  $|i\rangle, i \in \{1, 2, 3\}$  represent the eigenstates of our system and form the orthonormal basis for the Hilbert space of the atom. Operators acting on these states can be represented in this basis. For example, the dipole operator  $\mathbf{d}$  can be expressed as

$$\mathbf{d} = \sum_{j,k} \mathbf{d}_{jk} \sigma_{jk}, \quad (2.5)$$

where  $\mathbf{d}_{jk} = \langle j | \mathbf{d} | k \rangle$  are the dipole matrix elements,  $\sigma_{jk} = |j\rangle \langle k|$  are the transition projection operators or flip operators and the sum over  $j, k$  accounts for the three atomic states.

The electric dipole interaction has negative parity<sup>2</sup> and is therefore completely *off-diagonal*. This means that it only couples different states to each other, never the same state to itself. Furthermore we assume that the storage state  $|3\rangle$  is long-lived and its transition to the ground state  $|1\rangle$  is dipole forbidden. Taking these assumptions into account reduces the expression for the dipole moment to

$$\mathbf{d} = \mathbf{d}_{12} \sigma_{12} + \mathbf{d}_{23} \sigma_{23} + h.c. \quad (2.6)$$

## 2.2 Light-matter interaction Hamiltonian

Knowing what the electric fields look like and how the light fields couple to the atoms, we are now able write down a Hamiltonian describing the complete light-

matter system,

$$H = H_A + H_L + H_{ED}. \quad (2.7)$$

$H_A$  is the pure atomic Hamiltonian. Its eigenstates are given by the atomic states  $|1\rangle, |2\rangle, |3\rangle$ , which is why  $H_A$  is purely diagonal and can be expressed as

$$H_A = \sum_j \omega_j \sigma_{jj}. \quad (2.8)$$

The resonant frequency  $\omega_j$  corresponds to the atomic state  $|j\rangle$ .

$H_L$  is the free-field energy of the light field and can be written as

$$H_L = \int \omega a^\dagger(\omega) a(\omega) d\omega. \quad (2.9)$$

In order to find the time evolution of the atomic flip operators, we use the Heisenberg equation of motion. As the flip operators always commute with the optical free-field Hamiltonian  $H_L$ , we do not include it and the Heisenberg equation reduces to

$$\partial_t \sigma_{jk} = i[\sigma_{jk}, H_A + H_{ED}]. \quad (2.10)$$

Substituting for  $H_A$  and  $H_{ED}$  gives us five independent equations of motion; two for the atomic populations,

$$\begin{aligned} \partial_t \sigma_{11} &= -iE(\mathbf{d}_{12}\sigma_{12} - h.c.), \\ \partial_t \sigma_{33} &= iE(\mathbf{d}_{23}\sigma_{23} - h.c.), \end{aligned} \quad (2.11)$$

and three for the atomic coherences,

$$\begin{aligned}
\partial_t \sigma_{12} &= i\omega_{21}\sigma_{12} - iE[\mathbf{d}_{12}^*(\sigma_{11} - \sigma_{22}) + \mathbf{d}_{23}\sigma_{13}], \\
\partial_t \sigma_{13} &= i\omega_{31}\sigma_{13} - iE[\mathbf{d}_{23}^*\sigma_{12} - \mathbf{d}_{12}^*\sigma_{23}], \\
\partial_t \sigma_{23} &= i\omega_{32}\sigma_{23} - iE[\mathbf{d}_{23}^*(\sigma_{22} - \sigma_{33}) - \mathbf{d}_{12}\sigma_{13}],
\end{aligned} \tag{2.12}$$

where  $\omega_{jk} = \omega_j - \omega_k$  is the frequency difference between states  $|j\rangle$  and  $|k\rangle$ . Note that  $\sum_j \sigma_{jj} = I$ , the identity, so that the sum of the populations commutes with the Hamiltonian, and therefore has no time-dependence. This simply expresses the fact that the atom remains in one of the states  $|1\rangle, |2\rangle, |3\rangle$ , at all times<sup>[88]</sup>. Therefore  $\partial_t \sigma_{22} = -\partial_t(\sigma_{11} - \sigma_{33})$ .

The set of coupled differential equations (2.11) and (2.12) describes the whole interaction physics. In this form though, it is not possible to find an analytic solution which is why additional assumptions need to be made.

### 2.3 Equations of motion for atomic coherences

Applying two different linear approximations<sup>[88]</sup>, the rotating wave approximation<sup>[84,89]</sup> and neglecting unwanted coupling of the strong control field to the excited state, which is a valid assumption given the detuning  $\Delta$  is large, leads us to the linearised equations of motion for the atomic coherences,

$$\begin{aligned}
\partial_t \tilde{\sigma}_{12} &= \mathbf{d}_{12}^* g_s A e^{-i\Delta\tau} - i\mathbf{d}_{23} E_c e^{-i\Delta\tau} \tilde{\sigma}_{13}, \\
\partial_t \tilde{\sigma}_{13} &= -i\mathbf{d}_{23}^* E_c e^{i\Delta\tau} \tilde{\sigma}_{12},
\end{aligned} \tag{2.13}$$

where  $\tilde{\sigma}_{jk} = \sigma_{jk} e^{i\omega_{jk}\tau}$  are the slowly varying atomic flip operators and  $\tau = t - z/c$  is the *retarded time* in a moving frame. Equations (2.13) completely describe the memory interaction process. In the first equation one can see how  $\tilde{\sigma}_{12}$  is directly excited by the signal field  $A$  and the second equation illustrates how that excitation is coupled to the atomic coherence  $\tilde{\sigma}_{13}$  by the control field  $E_c$ .

## 2.4 Light propagation

The atomic ensemble we consider behaves like a dielectric medium in the presence of a signal field. We start from Maxwell's equations,

$$\begin{aligned} \nabla \cdot \mathbf{D} &= \rho_{\text{free}}, & \nabla \cdot \mathbf{B} &= 0, \\ \nabla \times \mathbf{E} &= -\partial_t \mathbf{B}, & \nabla \times \mathbf{H} &= \mathbf{J}_{\text{free}} + \partial_t \mathbf{D}, \end{aligned} \quad (2.14)$$

where  $\mathbf{D}$  is the *displacement field*,  $\mathbf{E}$  is the *electric field*,  $\mathbf{B}$  is the *magnetic induction*,  $\mathbf{H}$  is the *magnetic field*,  $\rho_{\text{free}}$  is the *free charge density* and  $\mathbf{J}_{\text{free}}$  is the *current*. After assuming that there are no free charges or currents ( $\rho_{\text{free}} = \mathbf{J}_{\text{free}} = 0$ ), applying  $\mathbf{D} = \epsilon_0 \mathbf{E} + \mathbf{P}$  with  $\mathbf{P}$  being the atomic polarisation, and doing some mathematical simplifications<sup>[88]</sup>, we arrive at the wave equation for the signal field

$$\left[ \nabla^2 - \frac{1}{c^2} \partial_t^2 \right] \mathbf{E}_s = \mu_0 \partial_t^2 \mathbf{P}_s, \quad (2.15)$$

with  $\mathbf{E}_s$  the electric field of the signal and  $\mathbf{P}_s$  the atomic polarisation that acts on the signal field. The control field is intense enough such that it is not affected or changed by the atomic polarisation, so its propagation does not have to be considered in detail.

## 2.5 Raman memory equations

Now we have all the building blocks in order to put together a set of equations that govern the Raman memory process. As a final step to deriving these, we make a continuum approximation<sup>[85]</sup>, where we assume that the atomic flip operators  $\sigma_{jk}$  remain constant over a distance  $\delta z \ll \lambda_s$ , where  $\lambda_s = 2\pi c/\omega_s$  is the wavelength of the signal field. We then identify the coherences  $\sigma_{12} \rightarrow P(z)$  and  $\sigma_{13} \rightarrow B(z)$  where B is the spinwave excitation inside the medium and P is the atomic polarisation. Their commutation relations are:

$$\begin{aligned} [\sigma_{12}, \sigma_{12}^\dagger] &= 1 \quad \longrightarrow \quad [P(z), P^\dagger(z')] = \delta(z - z') \\ [\sigma_{13}, \sigma_{13}^\dagger] &= 1 \quad \longrightarrow \quad [B(z), B^\dagger(z')] = \delta(z - z'). \end{aligned} \quad (2.16)$$

Replacing the electric field of the input signal by  $\mathbf{E}_s \rightarrow A$  in (2.15) and adding (2.13 & 2.15) leads to

$$\begin{aligned} \partial_z A(z, \tau) &= -\kappa^* P(z, \tau), \\ \partial_\tau P(z, \tau) &= -\Gamma P(z, \tau) + \kappa A(z, \tau) - i\Omega(\tau) B(z, \tau), \\ \partial_\tau B(z, \tau) &= -\Omega^*(\tau) P(z, \tau), \end{aligned} \quad (2.17)$$

where  $\Gamma = \gamma - i\Delta$  is the *complex detuning*,  $\gamma$  is the *spontaneous decay rate* of the excited state,  $\Omega = \frac{d_{23}}{\hbar} E_c$  is the control Rabi frequency,  $\kappa = \frac{d_{12}^*}{\hbar} \sqrt{\frac{\hbar\omega_s n}{2\epsilon_0 c}}$  is the coupling constant and  $n$  is the number density of the atoms. These equations completely describe the interaction process between a classical input field  $A$  and the atomic polarisation  $P$  and the coupling to the spinwave excitation  $B$ .

## 2.6 Raman regime and adiabatic limit

In order to operate a quantum memory in the *Raman regime*, the detuning  $\Delta$  needs to be a lot bigger than the natural homogeneous linewidth  $\gamma$  of the atomic system's excited state  $|2\rangle$ :

$$\Delta \gg \gamma. \quad (2.18)$$

Finding analytic solutions to the equations of motion described in (2.17) is challenging, however, possible in the *adiabatic regime*<sup>[79,80]</sup>,

$$\begin{aligned} \Delta &\gg \Omega, \\ \Delta &\gg \delta_c, \end{aligned} \quad (2.19)$$

where  $\delta_c$  is the control field bandwidth. The idea behind this adiabatic approximation is that the prominent frequency in the system is the detuning  $\Delta$ , which is a lot larger than the Rabi frequency  $\Omega$  and the control field bandwidth  $\delta_c$ . In this case the Rabi frequency  $\Omega$  changes sufficiently slowly such that the change in the optical polarisation in equations (2.17) can be considered zero ( $\partial_\tau P = 0$ ). In other words, the natural dynamics of the optical polarisation ( $P$ ) are overwhelmed by the motion initiated by the signal and the control field — this is known as *adiabatic following*<sup>[88]</sup>. The optical polarisation can now be eliminated from the equations of motion (2.17), which reduce to

$$\begin{aligned} \left(\partial_z + \frac{d}{\Gamma}\right)A &= i\frac{\Omega\sqrt{d}}{\Gamma}B, \\ \left(\partial_\tau + \frac{|\Omega|^2}{\Gamma}\right)B &= -i\frac{\Omega^*\sqrt{d}}{\Gamma}A, \end{aligned} \quad (2.20)$$

where  $d = \frac{|\kappa|^2 L}{\gamma}$  is the on-resonant *optical depth*<sup>[79]</sup> of the atomic ensemble and  $L$  is the length of the atomic ensemble.

## 2.7 Raman storage, retrieval & efficiency

These semi-classical linearised Maxwell-Bloch equations (2.20) form the basis for Raman storage and retrieval (see Gorshkov<sup>[79,90,91]</sup> and Nunn<sup>[39,80,88,92]</sup>). Analytical solutions to these equations can be found in<sup>[39,79]</sup> and the spinwave  $B_{\text{mem}}$  and the retrieved signal  $A_{\text{out}}$  can be expressed as:

$$B_{\text{mem}}(z) = \int_{-\infty}^{\infty} f(\tau) J_0 \left[ 2C \sqrt{(1 - \omega(\tau))z} \right] A_{\text{in}}(\tau) d\tau \quad (2.21)$$

$$A_{\text{out}}(\tau) = f^*(\tau) \int_0^1 J_0 \left[ 2C \sqrt{\omega(\tau)(1 - z)} \right] B_{\text{mem}}(z) dz \quad (2.22)$$

Here  $A_{\text{in}}(\tau) = A(\tau, z = 0)$  and  $A_{\text{out}}(\tau) = A(\tau, z = L)$ .  $A_{\text{in}}$  is the amplitude of the incident signal field to be stored,  $J_0$  is a Bessel function and the number

$$C^2 = d\gamma W / \Delta^2 \quad (2.23)$$

quantifies the Raman memory coupling<sup>[80]</sup>.  $W$  is a normalisation related to the total energy in the control pulse  $W = \int_{-\infty}^{\infty} |\Omega(\tau)|^2 d\tau$ . The coupling parameter  $C$  is very important for the Raman memory, because together with the optical depth  $d$  (2.27) it directly affects the memory efficiency (2.26).  $\omega(\tau) = \frac{1}{W} \int_{-\infty}^{\tau} |\Omega(\tau')|^2 d\tau'$  is the dimensionless integrated Rabi frequency and  $f(\tau) = C e^{iW\omega(\tau)/\Delta} \Omega(\tau) / \sqrt{W}$  represents the normalised Stark-shifted Rabi frequency<sup>[88]</sup>. The longitudinal coordinate  $z$  is normalized so that  $z = 1$  represents the exit face of the ensemble.

The storage efficiency of the quantum memory  $\eta_{\text{store}}$  can be calculated by

$$\eta_{\text{store}} = N_{\text{mem}}/N_{\text{in}}, \quad (2.24)$$

where  $N_{\text{mem}} = \int_0^1 |B_{\text{mem}}(z)|^2 dz$  is the final number of spinwave excitations in the storage medium, and  $N_{\text{in}} = \int_{-\infty}^{\infty} |A_{\text{in}}(\tau)|^2 d\tau$  is the total number of incident signal photons.

The total efficiency of the quantum memory  $\eta_{\text{tot}}$  can be written as

$$\eta_{\text{tot}} = N_{\text{out}}/N_{\text{in}}, \quad (2.25)$$

where  $N_{\text{out}} = \int_{-\infty}^{\infty} |A_{\text{out}}(\tau)|^2 d\tau$  is the total number of retrieved photons from the memory.

These formulas are used in Section 4.5.2.2 to compare experimental results with theoretical predictions. Numerical solutions indicate that the Raman memory process can work very efficiently (close to 100%), when phase-matched backward retrieval techniques are applied<sup>[93]</sup>, as can be seen in Figure 4.14 (c).

A unified theory describing both off-resonant Raman and resonant EIT memories has been developed in<sup>[79]</sup>, where the memory efficiency is bounded by the resonant optical depth only:

$$\eta_{\text{tot}} \sim 1 - 2.9/d \quad (2.26)$$

This result suggests that a large on-resonant optical depth is crucial for achieving high quantum memory efficiencies.

## 2.8 Optical depth

The optical depth was introduced in Section 2.6. It can also be expressed as

$$d = \frac{|\kappa|^2 L}{\gamma} = \left| \frac{d_{12}^*}{\hbar} \right|^2 \frac{\hbar \omega_s}{2\epsilon_0 c \mathcal{A} \gamma} \times N_A, \quad (2.27)$$

where  $N_A$  is the number of atoms in the ensemble. As can be seen from (2.27), the optical depth mostly depends on interaction medium specific parameters, as well as signal field specific parameters. The major contribution, though, originates from  $N_A$ , the number of atoms.

As discussed in Section 2.7, the optical depth directly influences the total memory efficiency. Therefore warm atomic vapours have a great advantage compared to cold ensembles<sup>[48,94]</sup> because the achievable optical depth is significantly larger<sup>[33,95]</sup>.

Of course there are issues that have to be thought about in warm atomic vapours, like atomic motion, collisions with other atoms or the containing walls, the use of buffer gas, Doppler shifts, etc. As I will show in this thesis, the far off-resonant Raman memory approach deals with many of these issues excellently and makes them negligible.

## 2.9 Raman memory benefits

As we have briefly addressed in the introduction (see Section 1.2.4), Raman memories, especially if implemented in a warm room temperature vapour, offer a certain set of benefits that make them potentially useful for future quantum information technology applications.

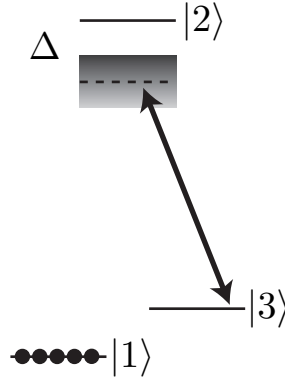


**Figure 2.2:** Virtual Raman resonance. The strong control field dynamically dresses the storage state  $|3\rangle$  to a virtual state detuned by  $\Delta$  from the excited state  $|2\rangle$ . The bandwidth of this virtual resonance is determined by the bandwidth of the control field. The system is prepared in the ground state  $|1\rangle$ .

### 2.9.1 Bandwidth

Besides the large achievable optical depth and efficiencies, the bandwidth is another important factor when it comes to characterising a quantum memory (see Section 1.2.4). Due to the large detuning (see Section 2.6), the Raman memory works far off-resonance. This far off-resonant character allows for storing broadband photons much larger than the individual linewidth of the excited states of the atom participating in the interaction.

The way this works can be seen from looking at the mechanism that drives the interaction (see Figure 2.2). The strong control field dresses the storage state  $|3\rangle$  such that a broad virtual Raman resonance is created. The bandwidth of this virtual resonance is independent of the excited state linewidth and the control field Rabi frequency, unlike the EIT case, where the bandwidth of the transmission window directly depends on the Rabi frequency. In the far off-resonant Raman case the important variable determining the bandwidth of the virtual state is

the bandwidth of the control field, detuned by  $\Delta$  from the  $|3\rangle - |2\rangle$  transition. It dynamically generates this Raman resonance into which a signal field, detuned by  $\Delta$  from the  $|1\rangle - |2\rangle$  transition, can be absorbed and then stored in the spinwave coherence between the ground  $|1\rangle$  and the storage state  $|3\rangle$ , as we have seen in Section 2.7.

In principle the Raman memory offers extremely large bandwidth. As long as all the constraints from the adiabatic regime (see Section 2.6) are fulfilled, the bandwidth of the memory could be increased by applying more broadband control fields and detuning further. The issue with this is that the memory interaction scales with the coupling parameter  $C$  introduced in Equation (2.23) in Section 2.7. The larger the detuning  $\Delta$  from the bare atomic resonance, the smaller the coupling parameter  $C$ . In order to compensate for the large detuning, the control field  $\Omega$  has to be increased. The limit to this is that eventually the condition  $\Delta \gg \Omega$  is violated (see Equation 2.19). In order to keep the balance, the optical depth  $d$  has to be increased.

Another issue arises from the splitting of the ground state and the storage state. This splitting in alkali atoms is typically of the order of several GHz<sup>[95,96]</sup>. This sets a natural limit for the storage of broadband light pulses, because under no circumstances should the applied fields overlap with both the ground and storage state at the same time. This means that if one wanted to store very broadband light pulses, say on the THz scale, one would have to find or engineer a system that offers a large enough splitting of the ground and the storage states<sup>[97]</sup> – or develop new design principles for the memory interaction.

The term *broadband* in this thesis refers to the fact that Fourier-transform-limited, temporally short photons have a large spectral frequency distribution.

### 2.9.2 Robustness, compatibility & integrability

Another positive feature arises from the large detuning  $\Delta$  necessary for the Raman protocol to function properly. It is robustness. What I mean by this is the fact that the large detuning makes the Raman memory tolerant to random inhomogeneous broadening. As discussed in Section 1.2, there are memory schemes, like CRIB or AFC, where a controlled inhomogeneous broadening is explicitly desired and created by an externally applied electric or magnetic gradient field. However, uncontrolled inhomogeneous broadening, for example caused by the random motion of atoms in a hot vapour or the large spread of absorption frequencies caused by doping of rare earth ion crystals, is a problem.

In the far off-resonant Raman case we do not address a single magnetic sub-level of a certain hyperfine state. Rather, we address a whole manifold of states at the same time. As we will see in the next chapters, the inhomogeneous broadening in a warm atomic vapour is on the order of several hundred MHz, which makes it impossible to address a single atomic resonance and isolate it. However, this is not necessary, because at a large detuning of 20 GHz for example, the light fields address all the resonances approximately equally.

This flexibility is a huge benefit and enables the Raman memory to interface with many different interaction systems, such as alkali atoms<sup>[95,96]</sup>, quantum dots<sup>[98]</sup>, solid state absorbers like rare earth ion doped crystals<sup>[99]</sup> or NV centers in diamond<sup>[100]</sup>.

A last comment I would like to make concerns integrability. Recently there has been much discussion at conferences, summer-schools and workshops about integrated quantum communication devices and how important miniaturisation and reliability is. If a functioning global quantum information architecture is to

be established it will surely require simple, easy to operate, room-temperature devices that are able to function without artificially created, magneto optically-trapped<sup>1</sup>[47,49,94] or cryogenically-cooled<sup>[35,66,68,76,77]</sup> environments. As we will see in Section 5.2, we managed to implement an easy-to-operate room temperature single photon level optical memory which fulfils most of these criteria. Furthermore, it is hard to believe that the other, technically very demanding technologies can be miniaturised and integrated easily into a small “black-box” quantum repeater system, which might be located at the bottom of the Atlantic ocean in an intercontinental quantum network. Therefore room-temperature approaches<sup>[33,101]</sup> utilising a simple experimental infrastructure are very promising options.

In order to make this physically feasible, integrated quantum memories are required. Recently there has been major progress in manufacturing miniaturised vapour cells<sup>[45,102]</sup>, creating hollow core waveguide structures that are able to contain room-temperature alkali gases<sup>[46]</sup> or trapping cold atoms cylindrically around a tapered nano-fibre<sup>[103]</sup>. All these approaches open up a way to achieving the goal of integrated quantum communication devices in the near future and can be well-interfaced with the far off-resonant Raman memory scheme.

## 2.10 Decoherence & Noise

In this section we present a theoretical model describing the decoherence of the spinwave excitation due to magnetic dephasing. Furthermore we give a theoretical description of the single-photon-noise floor for the operation of the Raman

---

<sup>1</sup>A *Magneto optical trap* (MOT) is a device for trapping atoms at low temperatures by using different detuned laser beams and magnetic fields.

memory in the quantum regime. The decoherence model relates to experimental measurements of the quantum memory lifetime described in Section 4.6.2.4. Experimental data regarding quantum noise and its comparison to theory can be found in Section 5.2.3

### 2.10.1 Magnetic dephasing

We model the magnetic dephasing by considering the evolution of the Raman coherence excited in the memory under the influence of a static magnetic field. The motivation for such a treatment originated from experimental data presented in Section 4.6.2.4. Figure 4.24 illustrates the reduction of memory efficiency with increasing storage time, indicating that magnetic decoherence mechanisms affect the spinwave excitation imprinted on the atomic caesium ensemble.

Suppose that an atom is initially prepared in the Zeeman state  $|F_i, m_i\rangle$  with probability  $p_{m_i}$  within the initial hyperfine manifold with  $F_i = 4$ . Storing a signal pulse creates a spin wave, represented by applying the operator  $S^\dagger$  to the initial atomic state, where  $S = \alpha I + \beta \Sigma$ , with  $I$  the identity operator,  $\alpha$ ,  $\beta$  two coefficients quantifying the amplitude of the spin wave, whose values are not important, and  $\Sigma$  the transition operator given by

$$\Sigma = \sum_{m_i=-F_i}^{F_i} \sum_{m_f=-F_f}^{F_f} C(m_i, m_f) |F_i, m_i\rangle\langle F_f, m_f|. \quad (2.28)$$

Here  $C(m_i, m_f)$  is the coupling coefficient between the initial state and the final Zeeman state  $|F_f, m_f\rangle$ , with  $F_f = 3$ . To model the dephasing, the absolute coupling strengths are not important; the relative strengths are computed in a straightforward manner from the Clebsch-Gordan coefficients describing the al-

lowed transitions, once the polarisations of the control field and the signal field are fixed. Over a time  $t$ , the atomic spins undergo Larmor precession due to the magnetic field. If the field has strength  $B$  in a direction parameterized by the polar and azimuthal angles  $\theta$ ,  $\phi$ , the precession is described by the operator  $U = R^\dagger E R$ , where  $R$  rotates the quantization axis to align it with the field, and  $E$  accounts for the accumulation of phase by each Zeeman level,

$$R = \sum_{m_i=-F_i}^{F_i} e^{i(Y_i \sin \phi - X_i \cos \phi)\theta} |F_i, m_i\rangle\langle F_i, m_i| \\ + \sum_{m_f=-F_f}^{F_f} e^{i(Y_f \sin \phi - X_f \cos \phi)\theta} |F_f, m_f\rangle\langle F_f, m_f|;$$

$$E = \sum_{m_i=-F_i}^{F_i} e^{im_i g_i \mu_B B t} |F_i, m_i\rangle\langle F_i, m_i| \\ + \sum_{m_f=-F_f}^{F_f} e^{im_f g_f \mu_B B t} |F_f, m_f\rangle\langle F_f, m_f|.$$

Here  $X_{i,f}$ ,  $Y_{i,f}$  are the  $x$  and  $y$  components of the spin angular momentum operators for the spins  $F_{i,f}$ , and  $g_{i,f}$  are the  $g$ -factors determining the size of the Zeeman splitting within each hyperfine manifold. In our case we have  $g_i = 1/4$  and  $g_f = -1/4$ .  $\mu_B$  is the Bohr magneton. The Raman coherence acts as a source for the retrieved signal field in the presence of the retrieval control pulse. The transition operator  $\Sigma$  plays a similar role to the spinwave excitation  $B$  in the  $\Lambda$ -level theory of Section 2.5. Upon retrieval,  $\Sigma$  is mapped to a polarisation  $P$ , which radiates the retrieved signal field. The retrieval efficiency is therefore proportional to  $|\langle P \rangle|^2 \propto |\langle \Sigma \rangle|^2$ , where the second expectation value is evaluated

just before retrieval. Incoherently summing the contributions arising from atoms starting in each of the initial Zeeman levels, we compute the retrieval efficiency according to the formula

$$\eta(t) \propto \sum_{m_i=-F_i}^{F_i} p_{m_i} |\langle F_i, m_i | SU^\dagger \Sigma U S^\dagger | F_i, m_i \rangle|^2. \quad (2.29)$$

The only non-vanishing terms in the above expression are all proportional to  $|\alpha\beta^*|^2$ , confirming that the absolute values of these coefficients simply determine the scaling of  $\eta$ , not its shape, so that we obtain

$$\eta(t) \propto \sum_{m_i=-F_i}^{F_i} p_{m_i} |\langle F_i, m_i | U^\dagger \Sigma U \Sigma^\dagger | F_i, m_i \rangle|^2. \quad (2.30)$$

This is the equation that we are going to use in Section 4.6.2.4 in order to model the experimentally measured spinwave decay.

### 2.10.2 Stimulated Raman scattering (SRS) noise model

Our experimental findings presented in Section 5.2.3 indicate that the dominant noise processes in our Raman memory are due to spontaneous Stokes and anti-Stokes scattering during the strong control pulse. Figure 5.4 displays the measured single-photon-level noise related to optical pumping of the ground state  $|1\rangle$  or the storage state  $|3\rangle$ .

To model this noise theoretically, we consider the Maxwell-Bloch equations. They describe the collinear propagation of Stokes and anti-Stokes field amplitudes  $A_S$ ,  $A_{AS}$  through a  $\Lambda$ -type ensemble with resonant optical depth  $d$  along the  $z$ -axis, in the presence of a control pulse, whose shape is described by the time

dependent Rabi frequency  $\Omega = \Omega(\tau)$ , where  $\tau$  is the time in a reference frame moving with the control. In the adiabatic limit, where the bandwidth and Rabi frequency of the control are much smaller than the detuning of the fields from resonance, the propagation equations take the form

$$\begin{aligned}
 \left[ \partial_z + \frac{d\gamma p_1}{\Gamma_S} \right] A_S &= -\frac{\Omega \sqrt{d\gamma}}{\Gamma_S} B, \\
 \left[ \partial_z - \frac{d\gamma p_3}{\Gamma_{AS}^*} \right] A_{AS}^\dagger &= -\frac{\Omega^* \sqrt{d\gamma}}{\Gamma_{AS}^*} B, \\
 \left[ \partial_\tau - |\Omega|^2 \left( \frac{1}{\Gamma_S} - \frac{1}{\Gamma_{AS}^*} \right) \right] B &= -\sqrt{d\gamma} \Omega^* \left( \frac{p_1}{\Gamma_S} + \frac{p_3}{\Gamma_S^*} \right) A_S \\
 &\quad -\sqrt{d\gamma} \Omega \left( \frac{p_1}{\Gamma_{AS}} + \frac{p_3}{\Gamma_{AS}^*} \right) A_{AS}^\dagger,
 \end{aligned} \tag{2.31}$$

where  $B$  is the amplitude of the spin wave,  $\Gamma_{S,AS} = \gamma - i\Delta_{S,AS}$  is the complex detuning of the Stokes (anti-Stokes) field,  $\gamma$  is the homogeneous linewidth of the  $|1\rangle \leftrightarrow |2\rangle$  transition,  $\Delta_{AS} = \Delta_S + \delta$ , and the Stokes detuning  $\Delta_S$  is equal to the detuning  $\Delta$  of the signal field in Figure 2.1.  $\delta = 9.2$  GHz is the Stokes shift, which is related to the  $6S_{1/2}$   $F = 3$  &  $F = 4$  hyperfine-split states in caesium that are separated by 9.2 GHz (see Section 3.1). The  $z$ -coordinate has been normalised so that it runs from 0 to 1. We have defined  $p_1$  ( $p_3$ ) as the fraction of atoms initially in state  $|1\rangle$  ( $|3\rangle$ ). Since the noise process is weak, we assume that these populations, as well as the control pulse, are unaffected by the interaction.

In general, the solution is given by

$$\begin{aligned}
A_{S,\text{out}}(\tau) &= \int_{-\infty}^{\infty} K_S(\tau, \tau') A_{S,\text{in}}(\tau') d\tau' \\
&+ \int_{-\infty}^{\infty} G_S(\tau, \tau') A_{AS,\text{in}}^\dagger(\tau') d\tau' \\
&+ \int_0^1 L_S(\tau, z) B_{\text{in}}(z) dz,
\end{aligned} \tag{2.32}$$

$$\begin{aligned}
A_{AS,\text{out}}(\tau) &= \int_{-\infty}^{\infty} K_{AS}(\tau, \tau') A_{AS,\text{in}}(\tau') d\tau' \\
&+ \int_{-\infty}^{\infty} G_{AS}(\tau, \tau') A_{S,\text{in}}^\dagger(\tau') d\tau' \\
&+ \int_0^1 L_{AS}(\tau, z) B_{\text{in}}^\dagger(z) dz,
\end{aligned} \tag{2.33}$$

where the subscripts ‘in’ (‘out’) describe the amplitudes at the start (end) of the interaction, and where the integral kernels  $K_{S,AS}$ ,  $G_{S,AS}$  and  $L_{S,AS}$  are Green’s functions that propagate the input fields to compute the output fields. Both the Stokes and anti-Stokes frequencies are passed by our spectral filters, so our noise signal is calculated by adding the average number of photons scattered into both Stokes and anti-Stokes modes,

$$\begin{aligned}
S &= \int_{-\infty}^{\infty} \langle A_{S,\text{out}}^\dagger(\tau) A_{S,\text{out}}(\tau) \rangle d\tau \\
&+ \int_{-\infty}^{\infty} \langle A_{AS,\text{out}}^\dagger(\tau) A_{AS,\text{out}}(\tau) \rangle d\tau.
\end{aligned} \tag{2.34}$$

It can be shown that the averaged photon numbers do not depend on the shape of

the control pulse, but only on its energy, through the quantity  $W = \int_{-\infty}^{\infty} |\Omega(\tau)|^2 d\tau$  [80], as is usual in the transient regime of spontaneous Raman scattering [104]. The initial state used to evaluate the expectation values is the vacuum state, with no Stokes/anti-Stokes photons and no spin wave excitations. Using the bosonic commutation relations  $[A_{A,AS,in}(\tau), A_{A,AS,in}^\dagger(\tau')] = \delta(\tau - \tau')$ , and noting that  $B \propto |1\rangle\langle 3|$ , so that  $\langle B_{in}^\dagger(z)B_{in}(z') \rangle = p_3\delta(z - z')$  and  $\langle B_{in}(z)B_{in}^\dagger(z') \rangle = p_1\delta(z - z')$ , we obtain

$$S = \int_{-\infty}^{\infty} \int_{-\infty}^{\infty} d\tau' d\tau \{ |G_S(\tau, \tau')|^2 + |G_{AS}(\tau, \tau')|^2 \} \quad (2.35)$$

$$+ \int_{-\infty}^{\infty} \int_0^1 dz d\tau \{ p_3 |L_S(\tau, z)|^2 + p_1 |L_{AS}(\tau, z)|^2 \}.$$

This expression depends only on the Green's functions, and can be evaluated by solving the system of equations (2.31) numerically, treating the amplitudes  $A_S$ ,  $A_{AS}$ , and  $B$  as classical complex-valued functions. The variation of the populations  $p_{1,3}$  with optical pumping power  $P$  is modelled by setting

$$p_3(P) = \frac{1}{2} \left[ 1 + \frac{P/P_s}{1 + |P|/P_s} \right]; \quad p_1(P) = 1 - p_3(P), \quad (2.36)$$

where  $P_s$  is the saturation power and with the convention that negative values of  $P$  indicate pumping on the blue  $|2\rangle \leftrightarrow |3\rangle$  transition. The spontaneously scattered Raman noise is then given by  $S_{\text{obs}}(P) = \kappa S(P)$ , which incorporates a scaling parameter into the simple one-dimensional theory to account for the fact that the Raman scattering process has a broad spatial distribution [104,105], whereas the signal is emitted into a single narrower spatial mode. The parameter  $\kappa$  defines the overlap between the scattered mode and the detected mode, which

is defined and filtered by a single-mode fibre optimised on the signal mode.

This consideration of spontaneously scattered Raman photons is very important when the quantum memory is operated at the single photon level. The Stokes noise (2.32) and Anti Stokes noise (2.33) are computed by solving the set of coupled differential equations (2.31) numerically for a chosen set of populations  $p_{1,3}$ , where the Green's functions  $K_S$ ,  $G_S$  and  $L_S$  that determine the Stokes and Anti Stokes noise are found through several iteration cycles. This model will be used in Section 5.2.3 in order to compare the theoretical noise predictions with experimentally measured noise data.



# Chapter 3

## Caesium experiment

In this chapter I introduce the experimental configuration and apparatus for a Raman memory. Many of the following sections illustrate a chronological path that developed dynamically bit by bit, as each hurdle was overcome.

I like to compare it with climbing a mountain, where you don't see the summit because it is covered in clouds (high optical depth) — you have to find your own way to reach it — on August 5th, 2009 we stood on top of it :)

### 3.1 Electronic configuration – $\Lambda$ -level structure

As was discussed in Section 2.9.2, there are many possible atomic systems one can use to implement a Raman memory. We chose to work with the alkali metal caesium (Cs)<sup>[95]</sup> for various reasons: i) Alkali atoms only have one electron in the outer most shell. This electron is optically active and can easily be addressed by electromagnetic radiation. ii) Caesium is the largest stable element out of the alkali metal group, which makes it also the slowest in a room temperature environment. This is important for a quantum memory operating in this regime

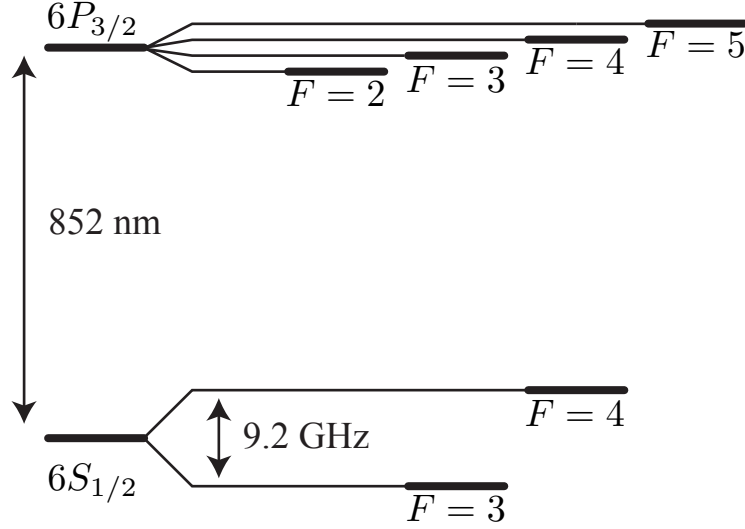


**Figure 3.1:** Electronic structure of caesium ( $\text{Cs}^{133}$ ). Caesium D<sub>2</sub>-line at 852 nm. The ground state hyperfine splitting between the  $6S_{1/2}$ ,  $F=3$  state and the  $6S_{1/2}$ ,  $F=4$  state is 9.2 GHz. This is the well-known caesium clock transition frequency. Both ground states are metastable and long-lived. The hyperfine splitting of the  $6P_{3/2}$ ,  $F=2, 3, 4, 5$  states is  $\sim 200$  MHz each.

because atomic diffusion is one of the decoherence mechanisms that limit storage times of room temperature memories<sup>[33,106]</sup>. iii) Caesium has the largest hyperfine splitting of the alkali atoms (9.2 GHz) providing enough bandwidth for the storage and retrieval of temporally short laser pulses.

The electronic structure of caesium that is relevant for the quantum memory can be seen in Figure 3.1. The optically active transition used for the memory operation is the caesium D<sub>2</sub> line at 852 nm. This is in the near infra-red spectrum of light and is not visible with human eyes. The nuclear spin of Cs  $I = 7/2$  together with the total electron spin of  $J = 1/2$  for the ground states and  $J = 3/2$  for the excited states, produces the hyperfine structure illustrated in Figure 3.1. The hyperfine-split, long-lived  $6S_{1/2}$  states  $F=3$  and  $F=4$  have a separation of 9.2 GHz and serve as ground and storage state in the  $\Lambda$ -level scheme used

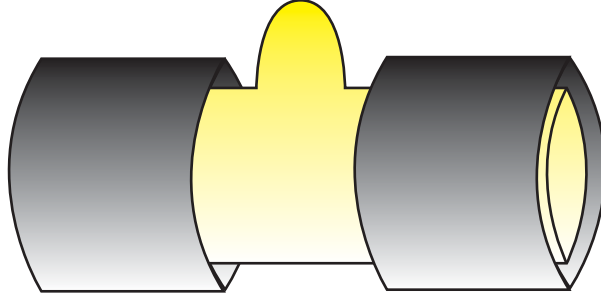


**Figure 3.2:** Schematic of the caesium vapour cell. Yellow container: cylindrical caesium cell with sealed nozzle (center). Grey shaded stubs: Heated holders of the vapour cell.

for the memory. They are the caesium clock transition states<sup>[107]</sup>, are dipole forbidden and are very long lived<sup>[108]</sup>. The hyperfine split  $6P_{3/2}$  states  $F = 2, 3, 4, 5$  are separated by about 200 MHz each. All of them together form the excited state relevant for the far off-resonant memory interaction. In the regime of a large detuning  $\Delta$  an effective, far-detuned dipole moment  $2.2 \times 10^{-29}$  Cm can be defined<sup>[95]</sup>, which describes the collective coupling of the  $D_2$  line to an impinging light field.

## 3.2 Vapour cell and heating system

The atomic vapour cell is the heart of the quantum memory. It provides the ensemble of caesium atoms within which the photons get stored and from which they are retrieved.

### 3.2.1 Cell setup

The vapour cell was purchased from Triad technologies (TT-CS-75-V-Q-CW). It is a glass cylinder with a length of 7.5 cm and a diameter of  $\varnothing = 2.5$  cm. It is made of heat resistant glass (up to 500°C) and has wedged windows that are antireflection coated for 852nm on the outside. The cell contains a liquid sample of caesium metal. At temperature  $T$  there is an equilibrium of caesium in gaseous and liquid phase<sup>[95]</sup>. More caesium atoms can be added to the ensemble by heating the vapour cell.

At the centre of the cylinder is a sealed nozzle; originally it was intended for the regulation of the buffer gas pressure (see Section 3.2.2). Attached to the nozzle (not illustrated in Figure 3.2) is a cold spot, implemented by a heat-resistant plastic tube that directs room-temperature air onto the centre of the vapour cell. This is very important because when the cell is placed inside a magnetic shielding cylinder<sup>1</sup> the temperature is homogeneously distributed, and the caesium condenses on all inner vapour cell surfaces, including the beam entrance and exit windows. Applying a cold spot to the vapour cell results in the condensation of caesium in the cooled areas only, thereby keeping the optical entry and exit ports clear. Typically the cell is heated to 62.5°C and the cold spot is kept a little lower at  $\sim 60^\circ\text{C}$ , which is enough to keep the windows clean.

An ohmic heating system consisting of counter-wound wires in order to cancel magnetic fields arising from the heating current is attached to two brass cylinders that slide over each end of the vapour cell. It is capable of regulating the temperature of the vapour cell from room-temperature to 300°C and is controlled via a feedback system from temperature sensors placed at the cold spot and directly

---

<sup>1</sup>Magnetic shielding reduces magnetic fields and creates a zero magnetic field environment.

in between the vapour cell and the brass cylinders. Its accuracy is  $\pm 0.1^\circ\text{C}$ .

### 3.2.2 Atoms and buffergas

The vapour cell contains caesium atoms with a typical density of  $1 \times 10^{18}$  particles  $\text{m}^{-3}$  at  $62.5^\circ\text{C}$ . The atoms at this temperature have an average thermal velocity of  $v_{\text{th}} = \sqrt{k_b T / m}$  where  $k_b$  is the Boltzmann constant,  $T$  is the temperature and  $m$  is the mass. In addition to the caesium vapour, neon buffer gas is added to the system. Its background pressure is 40 Torr, corresponding to a neon density of  $1 \times 10^{22}$  particles  $\text{m}^{-3}$ , a factor of  $10^4$  more compared to caesium. Therefore collisions of caesium atoms are much more likely to take place with neon atoms than with other caesium atoms. This has two major benefits:

i) Caesium atoms collide much more with other atoms and therefore their motion is comparable to a random walk<sup>[88]</sup>. This results in a much longer diffusion time of caesium atoms out of an optical beam path that addresses a certain subset of caesium atoms inside the atomic ensemble, which is important regarding the storage time of a quantum memory. For typical beam diameters  $\varnothing \sim 500 \mu\text{m}$  along the vapour cell (see Section 4.5.1) the atomic diffusion time of caesium atoms out of the beam path is estimated to be several hundred microseconds<sup>[88]</sup>.

ii) Caesium-neon collisions are *spin preserving*. In other words, quantum information, that has been stored in the hyperfine levels of the caesium D<sub>2</sub> line, is not affected by collisions with neon atoms. The reason is that neon has no nuclear spin and no electron spin and therefore no magnetic moment associated with it that could affect the spin coherences established in caesium atoms.

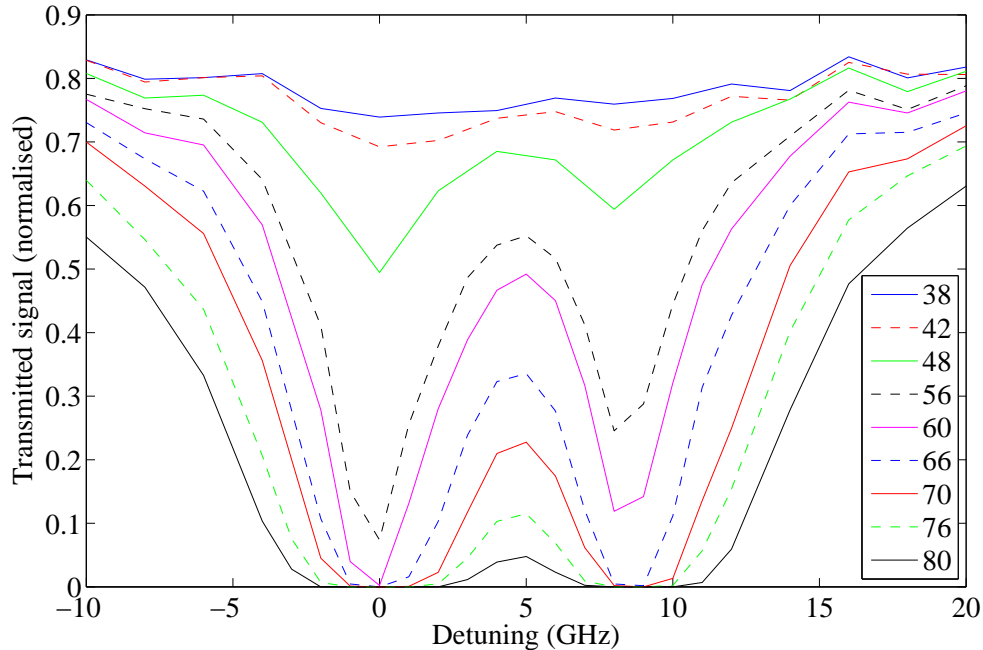


**Figure 3.3:** Caesium  $D_2$  line absorption spectrum. Plotted is the transmission of a probe beam vs. the detuning from the red resonance, located at 0 GHz detuning. The blue resonance is positioned at a detuning of 9.2 GHz. The differently coloured dashed and solid lines represent data taken at different vapour cell temperatures, ranging from 38° to 80° celsius.

### 3.2.3 Caesium absorption profile

As discussed in Section 3.1, we operate on the caesium  $D_2$  line at 852 nm, consisting of two hyperfine resonances separated by 9.2 GHz ( $6S_{1/2}$   $F=3$  &  $F=4$ ). Each of them is highly degenerate and hosts several magnetic sub-levels ( $m_F = -F, \dots, +F$ ). In a warm atomic vapour the hyperfine resonances are broadened by mechanisms like Doppler broadening due to atomic motion, pressure broadening due to vapour pressure, collisional broadening arising from caesium collisions with the buffer gas, etc. Most of these mechanisms depend strongly on temperature, and in order to get a feeling for the width of the  $D_2$  line resonances at different temperatures, we scanned a weak probe laser (Tsunami pico second probe power

$\sim \mu W$ , see Section 3.3.1) across the resonances and measured the transmitted signal on a photodiode. The result can be seen in Figure 3.3. At low vapour cell temperatures there is only weak absorption of the probe beam. From  $\sim 48^\circ\text{C}$  and above the absorption of the two resonances becomes very prominent and two absorption dips start to form. The red resonance ( $F = 4 \rightarrow F' = 2, 3, 4, 5$ ) is located where the detuning is zero; the blue resonance ( $F = 3 \rightarrow F' = 2, 3, 4, 5$ ) is positioned at a detuning of 9.2 GHz. The red resonance is a bit stronger than the blue resonance and the FWHM of the absorption lines is on the order of several GHz. The Doppler broadening estimated from a simple model<sup>[109]</sup>

$$\Delta f_D \simeq \frac{2u}{\lambda}, \quad (3.1)$$

where  $u = \sqrt{2k_B T/m}$  is the most probable velocity at a Temperature  $T$ ,  $k_B$  is the Boltzmann constant and  $m$  is the atomic mass, is  $\sim 0.5$  GHz. The reason why the atomic resonances appear so broad can also be due to the width of the probe laser (1.5 GHz bandwidth). Ideally a narrow-band laser is used for probing and scanning across the resonances, but our diode laser only had a mode-hop-free tuning range of about 1 GHz (see Section 3.3.2).

### 3.3 Laser systems

In this section we discuss the two laser systems that were used to operate the quantum memory.

### 3.3.1 Tsunami Ti:Sapph

The main laser system is a custom designed *Tsunami*<sup>1</sup> Ti:Sapph laser that has a built in *Gires-Tournois Interferometer*<sup>2</sup> (GTI) to increase the laser pulse duration from the femtosecond regime to the picosecond regime. The reason for this becomes clear when we have a look back at the discussion on usable bandwidths for the Raman protocol in Section 2.9.1 and the atomic structure of caesium in Section 3.1. The hyperfine splitting of the ground state and the storage state is 9.2 GHz and therefore the bandwidth of the control field and the signal lasers needs to be smaller than that splitting. The laser pulses of this modified Ti:Sapph laser system were measured to be 300 picoseconds by an autocorrelation measurement carried out by Dr. Joshua Nunn<sup>[88]</sup>. This corresponds to a spectral bandwidth of about 1.5 GHz.

The laser system can be tuned roughly to the caesium D<sub>2</sub> line transition at 852 nm by adjusting the laser prisms and monitoring the frequency on a standard spectrometer (Ocean optics USB 2000+). Fine tuning requires changing the *free spectral range* (FSR) of the GTI, which is done by controlling the temperature and thus the distance between the GTI interferometer mirrors. The tuning range of the GTI is on the order of 40 GHz with a sensitivity of approximately 0.2 GHz. In order to find the precise caesium resonance, the caesium atoms' fluorescence is monitored in a reference vapour cell by a camera that is sensitive to the near-infrared spectrum.

The Tsunami laser system is pumped by a frequency doubled, continuous wave solid state laser system (Millenia Pro) providing 5W of green pump light

<sup>1</sup>A Tsunami laser system is a commercial femtosecond laser system from Spectra Physics.

<sup>2</sup>A Gires-Tournois Interferometer is a transparent plate with two reflecting surfaces, very similar to a Fabry Perot Etalon. One of the reflective surfaces has a very high reflectivity.

at 532 nm. The power output of the Tsunami oscillator reaches a maximum of 1.5 W with a repetition rate of 80 MHz. This means that every 12.5 ns a laser pulse with an energy of 62.5 nJ and a duration of 300 ps is emitted. The laser beam is vertically polarised.

### 3.3.2 External cavity diode laser (ECDL)

#### 3.3.2.1 General operation

An *external cavity diode laser* (ECDL) was used for optical pumping purposes (see Section 3.10)<sup>[110]</sup>. It is a home-built system consisting of a diode laser head, diode laser driver and current controller from Thorlabs and an external grating with 1800 l/mm that is arranged in the Littrow configuration<sup>[110]</sup>. This means that the first diffraction order of the grating is coupled back into the laser diode. Usually laser diodes have a multimode emission spectrum, exhibiting lasing activity at multiple spectral frequency components. When the first diffraction order is redirected into the laser diode an external cavity between the grating and the laser diode is established. This seeds one specific laser frequency and suppresses all other laser modes, which leads to true single mode operation of the diode laser. The zeroth order of the diffraction grating is used to couple out the single mode laser beam. Its bandwidth is typically on the order of one MHz.

The spatial mode of the laser beam was rather poor. The vertical component was roughly collimated but the horizontal component was strongly divergent and elongated. We compensated for this by using an anamorphic prism pair that transformed the elliptical beam into a nearly circular beam. The beam then passed through a Faraday isolator<sup>1</sup> and was coupled into a single-mode fibre in

---

<sup>1</sup>A Faraday isolator transmits light of one polarisation in one direction but not in the other.

order to clean up the spatial profile.

The total output power of the diode laser in the zeroth order was 100 mW. After all the optics and fibre coupling mentioned before, the laser power was reduced to 20 mW but the laser beam had a Gaussian profile and operated stably in a single frequency mode.

### 3.3.2.2 Switching the diode laser

Diode lasers used for optical pumping purposes naturally operate in the continuous wave (cw) regime. As we will see in Section 4.6.2.3 this is a problem for the storage of light pulses, because a coherent spinwave excitation will be destroyed if the on-resonant diode laser is permanently turned on during the storage time. Therefore, it is important to be able to switch on and off the diode laser quickly. I explored two approaches to this.

i) Using an optical chopper wheel that physically blocked and unblocked the diode laser beam as it spun. The chopper could be synchronised to an external trigger, e.g. the Pockels cell (see Section 3.8) such that it was phase stabilised to the laser pulses from the Ti:Sapph oscillator. The rise and fall times for the on/off switching of the laser beam, however, took about 10 - 15  $\mu$ s and experienced a strong temporal jitter.

ii) The use of an *acousto optic modulator* (AOM), turned out to be a much better choice. First of all there were no physically moving parts that could cause vibrations, and second the rise and fall times were  $\sim$  50 ns, much quicker compared to those of the chopper wheel.

The principle of operation is diffraction of a light beam of an acoustic grating established inside a quartz crystal. A piezo electric transducer oscillates at a

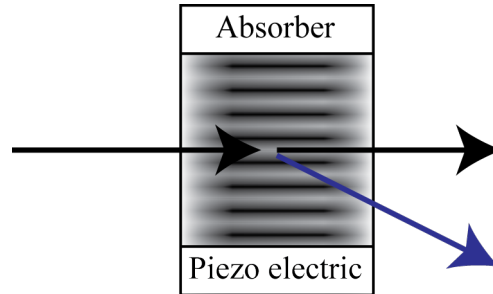


**Figure 3.4:** Principle of an acousto-optic modulator (AOM). An incoming laser beam is partially transmitted ( $\sim 20\%$ ) and partially diffracted ( $\sim 80\%$ ) when the AOM is switched on. The diffracted beam is blue detuned, shifted by the oscillation frequency of the piezo electric transducer. The acoustic absorber absorbs the oppositely created sound waves.

frequency, e.g. 80 MHz and creates sound waves inside the glass that change the refractive index of the material periodically. This acts as an acoustic Bragg grating off which an incident light beam is scattered. The transmitted beam has the same frequency as the incoming beam and the scattered beam has a shifted frequency set by the oscillation frequency of the transducer. The switching time of the AOM is basically set by the transit time of the sound wave across the beam waist of the incoming laser beam. The smaller the laser beam is focussed the quicker the AOM can switch (typically 5 - 100 ns). For our future experiments we only use the diffracted beam because it can be completely switched on and off. This is an important criteria for enabling long storage times in a quantum memory (see Section 4.6.2.3).

### 3.4 Signal field generation

As was discussed in Chapter 2, two light fields are needed for the operation of the quantum memory: the control field and the signal field. The control field

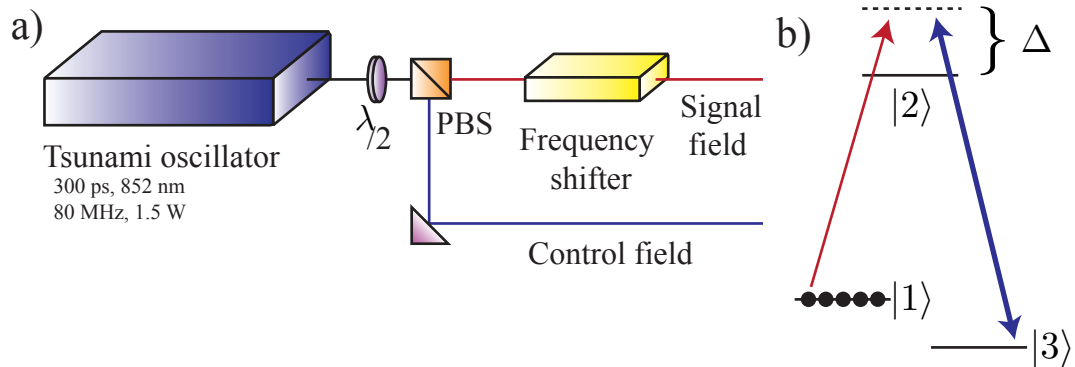


**Figure 3.5:** Signal field generation and  $\Lambda$ -level scheme. **(a)** Signal field generation. **(b)** The detuning  $\Delta$  is set 18.4 GHz to the blue of the excited state  $|2\rangle$ .  $\Lambda$ -level scheme with control field on the blue transition and signal field on the red transition. The ground state  $|1\rangle$  and the storage state  $|3\rangle$  separation is 9.2 GHz.

has to be powerful enough that it can mediate the two-photon transition from the ground to the storage state. Both fields were derived from the same source, namely the Tsunami laser oscillator described in Section 3.3.1. The laser beam was split into two beams using a half wave plate<sup>1</sup> and a polarising beam splitter cube (PBS)<sup>2</sup> (see Figure 3.5 (a)). The challenge was to introduce a frequency difference of 9.2 GHz between the control and the signal field. This is required for the two photon Raman memory interaction because the control and signal field have to be equally far detuned from the excited state  $|2\rangle$ . From this point on the  $\Lambda$ -level system we use is sketched as illustrated in Figure 3.5 (b). The upper state of the 6  $S_{1/2}$  states served as the ground state  $|1\rangle$  and the lower one served as the storage state  $|3\rangle$ . The control field was blue detuned by 18.4 GHz from the  $|3\rangle - |2\rangle$  transition (blue resonance). This was the position of the Tsunami laser oscillator. Therefore, the signal field (to be generated) had to be blue detuned by

<sup>1</sup>A half wave plate is a birefringent crystal that, if rotated by  $45^\circ$ , rotates a linearly polarised light beam by  $90^\circ$ .

<sup>2</sup>A PBS is a piece of optics that splits orthogonal polarisations into two output arms. Horizontal polarisation is transmitted and vertical polarisation is reflected by  $90^\circ$ .

18.4 GHz from the  $|1\rangle - |2\rangle$  transition in order to have same detuning  $\Delta$  from the excited state  $|2\rangle$  (see Figure 3.5 (b)). In the following we discuss two considered options for achieving this goal.

### 3.4.1 Raman cell approach

The first approach was the one I spent quite a lot of time on in my first year. We intended to use caesium vapour to generate stimulated Raman scattering, as discussed in Section 1.2.4. As it was not entirely clear in which parameter regime to work, this approach basically turned into a trial and error experience. I varied the cell temperature, the control field power of the laser system, the focal length of the lenses that focussed the laser beam into the vapour cell and the detuning from the excited state and looked both in the forward and backward direction and also investigated different polarisations.

Let us consider the outcome ahead of time and reveal the result here. This approach failed and I am going to explain in the following why this was the case.

i) We did not have the right means of spectral filtering. A 9.2 GHz frequency shift is a tiny difference in frequencies. It translates into a wavelength difference via the relation  $\Delta\lambda = \Delta f/f \times \lambda$ . Using the appropriate numbers for the caesium D<sub>2</sub> line transition<sup>[95]</sup> gives  $\Delta\lambda = 0.02$  nm. The best commercially available spectrometers one can purchase these days have a resolution of about 0.1 nm, too little to resolve our wavelength separation.

ii) Spontaneous Raman scattering events are very unlikely and a control field has a chance of  $1/10^6$  to produce a Stokes scattered photon when propagating through 1 cm of scattering medium (see Section 1.2.4). Spontaneously scattered Raman photons have a broad spatial distribution around the control field

mode<sup>[104,105]</sup>. Even if we managed to get into the stimulated regime, where the stimulated Stokes photons would be emitted alongside the control field, one would have to either spectrally resolve the two beams or extinguish the control field well enough to be able to detect the Raman signal only.

iii) At room temperature, both hyperfine states of the  $6S_{1/2}$  shell are roughly equally populated. In order to observe Raman scattering, optical pumping techniques (see Section 3.10) need to be applied in order to create a population imbalance. Optical pumping, however, works on the principle of excitation from the ground to the excited state and subsequent spontaneous decay into all possible decay channels, in our case the  $|2\rangle - |1\rangle$  and  $|2\rangle - |3\rangle$  transition. In addition to the optical pump beam this mechanism creates two more frequencies that have to be extinguished as well if Raman scattering is to be detected.

### 3.5 Spectrometer

As the generation of the signal field was not fruitful in the first vapour cell attempt, we needed to address the issues that prevented us from succeeding. The first challenge we tackled was the construction of a grating spectrometer that was able to detect a frequency shift of  $\Delta f = 9.2$  GHz ( $\Delta\lambda = 0.02$  nm). After sourcing the basic components for such a high resolution grating spectrometer from old unused experiments, we found the necessary pieces of equipment, namely a large grating ( $10$  cm<sup>2</sup>) with a line density of  $1200$  1/mm and a large parabolic mirror with a focal length of  $30$  cm and a diameter of  $13$  cm. The spectrometer design can be seen in Figure 3.6. The resolving power  $R$  of the spectrometer is given

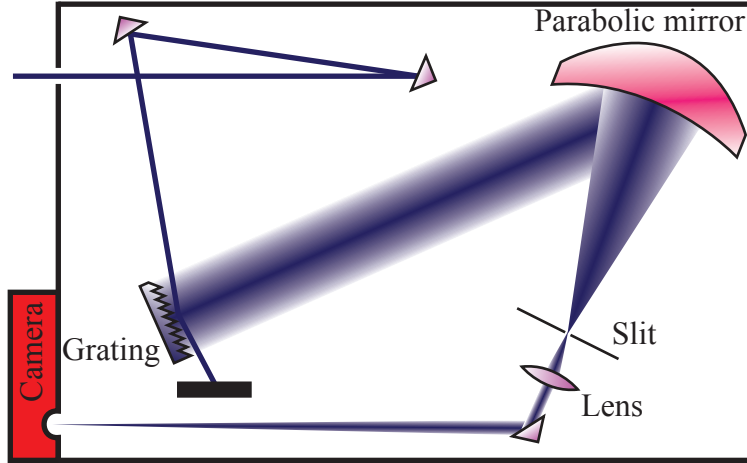


**Figure 3.6:** High resolution grating spectrometer. The incoming laser beam is directed onto a large grating with 1200 lines/mm. Its first diffraction order ( $m = 1$ ) is directed onto a parabolic mirror with a focal length of 30 cm. The slits in the focal plane clean up the image and another lens extends the focus of the mirror and images the beam onto the detection system (Andor camera).

by<sup>[111,112]</sup>

$$R = \frac{\lambda}{\Delta\lambda} = mN, \quad (3.2)$$

where  $\lambda$  is the central wavelength of the laser light,  $\Delta\lambda$  is the minimum wavelength difference that can be resolved,  $m$  is the diffraction order and  $N$  is the number of lines illuminated at the grating. Putting in the numbers for the interferometer (120,000 lines,  $m = 1$ ) and an incident light field ( $\lambda = 852$  nm) leads to a theoretical value of  $\Delta\lambda = 0.007$  nm for the minimum resolvable wavelength difference. Therefore, our setup should be able to resolve the signal field and control field which are separated by  $\Delta\lambda = 0.02$  nm.

The detection system used in this spectrometer setup is an *Andor i-Xon* camera, presented in Section 3.9.1. In the spectrometer, beams that are initially Gaussian-like and collimated are incident on the grating at an oblique angle;

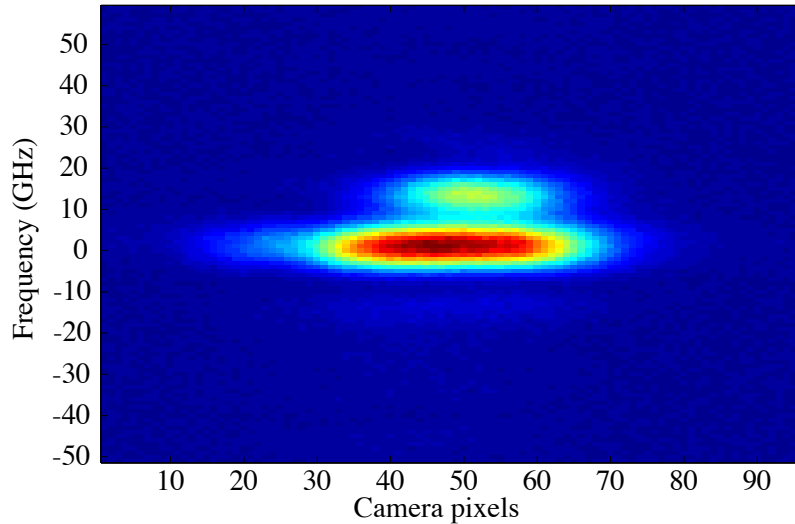


**Figure 3.7:** Spectrometer image with a resolution of 1 GHz/pixel. The diode laser (small blob) is tuned to the blue resonance and the pico-second laser (large blob) is tuned to the red resonance. The y-axis represents frequency, increasing from bottom to top. The laser frequencies are separated by 9.2 GHz.

when focussed, an image such as can be seen in Figure 3.7 is produced. In this image two ‘blobs’ are visible, each originating from a different laser beam. The reason they appear unequal in intensity is because the two different laser beams have different spatial modes (beam diameter and collimation) when they diffract off the grating. The x-axis represents spatial extent on the camera and the y-axis represents frequency in GHz. The resolution of the spectrometer is roughly 1 GHz per pixel and the frequency increases from bottom to top on the y-axis. The lower (broader) blob results from the tsunami laser tuned to the red resonance of the caesium  $D_2$  line at 852 nm and the upper (smaller) blob belongs to the diode laser tuned to the blue resonance. This image proves that our spectrometer is capable of separating two different laser beams separated by a wavelength difference of  $\Delta\lambda = 0.02$  nm, when the two beams are roughly equal in intensity. If they differ significantly in intensity it will be very difficult to resolve them.

### 3.5.1 Electro optic modulator (EOM)

The inefficiency of the spontaneous Raman scattering process ( $1/10^6$ ) was the main reason why the first approach was unsuccessful. Even with the new spectrometer (see Section 3.5), detection of such a weak and multimode Raman signal would be extremely difficult if not impossible. Therefore we decided to look into different options for generating the signal field. The solution was an *electro optic modulator* (EOM).

In principle an EOM is a phase modulator. It consists of a nonlinear crystal, such as Lithium niobate<sup>1</sup>, whose refractive index is a function of the strength of the local electric field inside the crystal. Applying an external electric field along one of the principal axes changes the refractive index for light polarised in this direction and therefore causes an optical path length change, that is proportional to the applied electric field. In turn, the phase of the optical field exiting the modulator depends on the electric field, too.

Applying an external radio frequency field to the EOM, for example with a frequency of 9.2 GHz corresponding to the required frequency difference for our quantum memory using caesium vapour, results in the creation of sidebands. In principle there are multiple sidebands present as can be seen in Figure 3.8.

The phase shift of the modulator is proportional to the applied strength of the electric radio frequency field. Initially, when there is no external field present, there is no sideband creation, only the carrier frequency  $\nu_0$  is transmitted (red curve). When the external electric field is increased, the onset of sideband creation is observable. Initially, there are only the first-order sidebands ( $m = 1$ ). The

---

<sup>1</sup>Lithium niobate ( $\text{LiNbO}_3$ ) is a compound of niobium, lithium and oxygen. Its single crystals are important material for optical modulators and other non-linear optical applications.

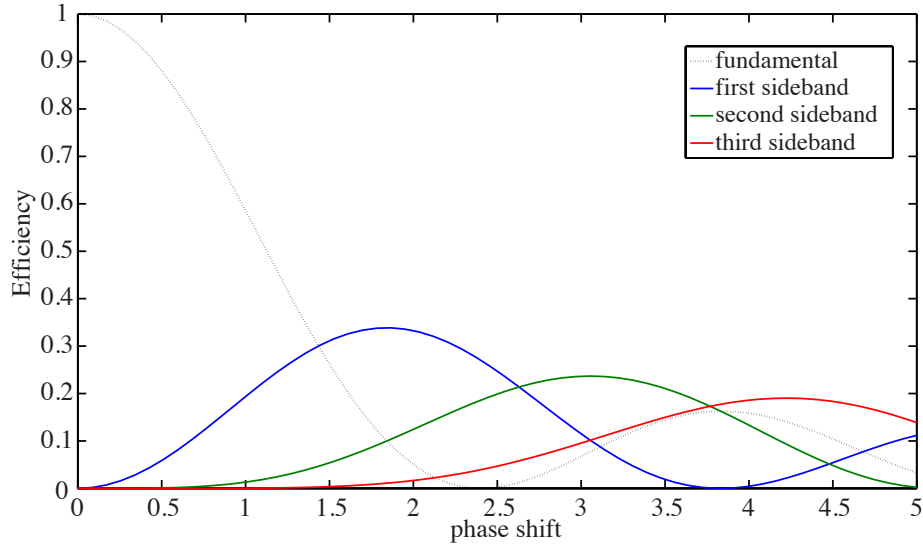


**Figure 3.8:** Efficiency of electro optic modulator (EOM). Sideband efficiency versus modulation depth. The modulation depth is proportional to the RF input power and the drive voltage.

frequency of the sidebands is given by  $\nu_0 \pm mx$ , where  $m$  is the order of the sideband and  $x$  is the frequency shift introduced by the external electric field (e.g. the 9.2 GHz modulation frequency). The optical power of the carrier is reduced and transformed into sideband power. Increasing the strength of the external electric field (and thereby the phase shift), leads to the generation of multiple sidebands of first, second and third order. The higher the order, the less efficient is the energy transformation process. In our case we would like to operate in a regime where we transform most of the power from the carrier into the first order sidebands but do not excite any second order effects.

The great advantage of such EOM systems is that the properties of a phase modulated optical beam are the same as those of the initial carrier beam. Furthermore, the unmodulated and modulated beams exiting the EOM are phase stable and collinear. The fact that the sideband beams travel alongside the car-

rier is another important aspect for us because it allows us to verify whether sidebands have been generated, using the spectrometer introduced in Section 3.5. Experimental sideband verification is demonstrated in Section 3.5.4.

### 3.5.2 EOM operation & switching

The EOM (Newport 4851-M @ 9.2 GHz) is equipped with a radio frequency (RF) input (SMA connector) and a built-in LC-circuit (RF oscillator) that enhances the amplitude of the applied electric field. The radio frequency was provided by a radio frequency generator (HP-8672A) with a frequency range from 2 - 18 GHz. It was set to 9.2 GHz and its power output was 0 dBm. This was not sufficient to modulate sidebands with the EOM, so the RF generator was connected to a broadband RF amplifier from Mini-Circuits (ZVA-183+), boosting the output power to  $\sim 25$  dBm. This corresponded to  $\sim 500$  mW RF power available to the EOM for sideband modulation.

As discussed in Section 3.5.1, the EOM modulates sidebands whenever a carrier frequency and RF power are available. It will become clearer in the course of this thesis, that the ability to switch off the EOM is of major importance for achieving longer storage times in the quantum memory (see Section 4.6). The solution was a very fast, broadband solid state RF switch from Hittite (HMC232LP4) with a on/off switching time of  $\sim 6$  ns and an isolation ratio of 45 dB. This ensured that the EOM was completely turned off when required.

### 3.5.3 First observation of sidebands

After the assembly of all components required for operating the EOM, the laser beam was aligned through the EOM using a 1:1 telescope consisting of two 40 cm

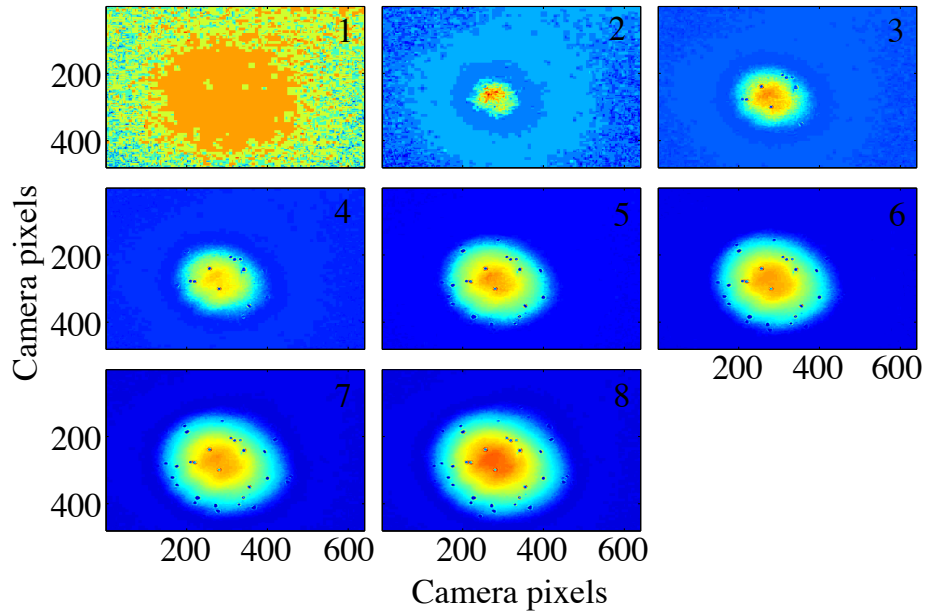


**Figure 3.9:** Spatial beam profiler. Images of modulated sidebands. Sideband intensity increases with increasing RF drive-power (5, 10, 12, 13, 15, 16, 17, 18 dBm).

lenses. The Rayleigh range was  $\sim 10$  cm and the beam diameter was  $\varnothing \sim 600 \mu\text{m}$ . Three etalons with an FSR of 18.4 GHz (see Section 3.7.2) were positioned after the EOM for extinguishing the carrier frequency. Successful sideband operation was first observed with a spatial beam profiler described in Section 3.9.2. The intensity of the sidebands as a function of RF drive-power can be seen in Figure 3.9. However, these images do not allow to distinguish between the blue and the red sideband. These images are preliminary results that demonstrate the functionality of the EOM and the Gaussian-like mode profile of the generated sidebands.

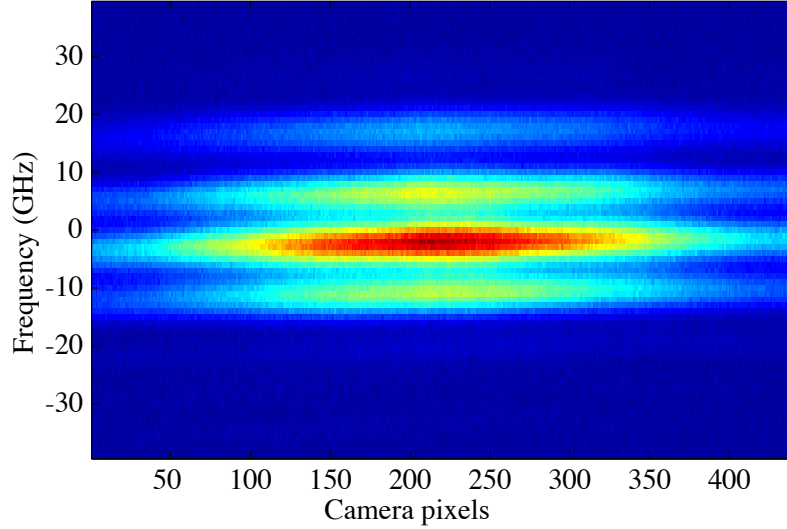


**Figure 3.10:** Spectrometer image of sidebands ( $m = 1$ ), carrier and diode laser.  $y$ -axis indicates frequency increase from bottom to top. Diode laser is tuned to the red resonance (top blob). The picosecond laser is tuned to 18 GHz to the red of the red resonance (strongest blob), with sidebands modulated 9.2 GHz shifted to each side.

### 3.5.4 Selective sideband detection with spectrometer

Using the high resolution spectrometer introduced in Section 3.5, the 9.2 GHz frequency-shifted modulated sidebands could be resolved spatially. The results are shown in Figure 3.10. The optical input to the spectrometer was fibre-coupled, which is why all the laser beams have the same physical shape compared to Figure 3.7, where they have different shapes because they were not fibre-coupled. Four blobs are visible in the image. The top blob (weakest one) represents the diode laser beam that was tuned to the red resonance on the  $|1\rangle - |2\rangle$  transition. The most prominent blob belongs to the picosecond laser, which was tuned 18 GHz to the red of the red resonance. 9.2 GHz to the blue and to the red of the picosecond carrier appear two more laser beams: the blue and the red frequency-shifted sidebands of the picosecond laser. The total modulation efficiency of the

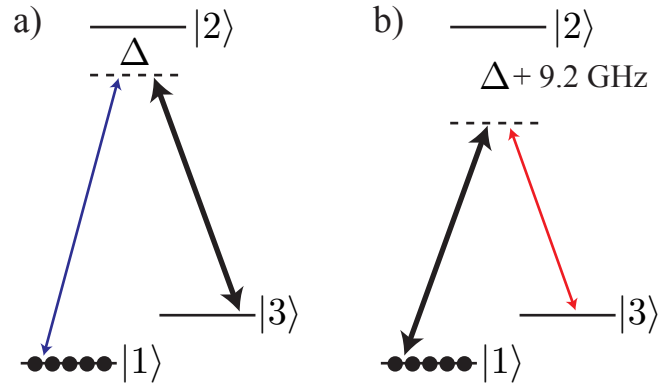


**Figure 3.11:** Double  $\Lambda$ -level system (a) Bold black arrow indicates control field detuned from resonance by  $\Delta$ . Two photon resonance established with blue sideband (light blue arrow). (b) Bold black arrow indicates control field detuned from resonance by  $\Delta + 9.2 \text{ GHz}$ . Two photon resonance established with red sideband (light red arrow).

EOM for each sideband was  $\sim 1\%$ .

This demonstrates that the different frequencies required for quantum memory operation in caesium vapour (see Section 4.4) can be generated: i) the diode laser, which is necessary for optical pumping and preparing the  $\Lambda$ -level system in the ground state  $|1\rangle$ . ii) the picosecond laser, which represents the control field. iii) the sidebands, one of which acts as the signal field that is going to be stored. These beams can be tuned to either side of the two resonances. This is important, because as we will see in Section 4.4, the quantum memory is going to be operated in a blue detuned regime relative to the blue resonance.

### 3.6 Double $\Lambda$ -level system issue

Two sidebands are problematic for the memory process, because of the development of a double  $\Lambda$ -level system as illustrated in Figure 3.11. These two  $\Lambda$ -level systems represent two competing processes. Imagine a memory process where

the system is prepared in the ground state  $|1\rangle$ , and the signal field (blue sideband, indicated by light blue arrow) is to be absorbed in the storage state  $|3\rangle$  via two-photon resonance with a strong control field (bold black arrow) as illustrated in Figure 3.11 (a). This by itself would work! But now consider the presence of a red sideband (light red arrow). A second two-photon resonance is established with the strong control field (bold black arrow) acting in the opposite way, as illustrated in Figure 3.11 (b). A stimulated Raman scattering process can be triggered, where the red sideband seeds the process and is enhanced. This event is less likely compared to the one described in Figure 3.11 (a), because the detuning  $\Delta$  is increased by 9.2 GHz. However, in the low photon number regime, this second unwanted effect creates noise, afflicting future experiments. In order to avoid any confusion caused by multiple  $\Lambda$ -systems, we face a new challenge: the extinction of one of the sidebands and the extinction of the strong control field. Only a single laser frequency is to remain in the signal field arm, namely the signal field that is to be stored (see Figure 4.10 (b)).

## 3.7 Filtering

In principle, high-resolution spectrometers like the one described in Section 3.5 could be used to distinguish between laser frequencies, separated by 9.2 GHz. Razor blades positioned in the focal plane of the spectrometer's large parabolic mirror (see Figure 3.6) could block unwanted laser frequencies, because different frequencies get imaged besides each other. As discussed in Section 3.5.4, the spatial separation between the generated sidebands and the carrier frequency is only several  $\mu\text{m}$ . This is not large enough to achieve good extinction between

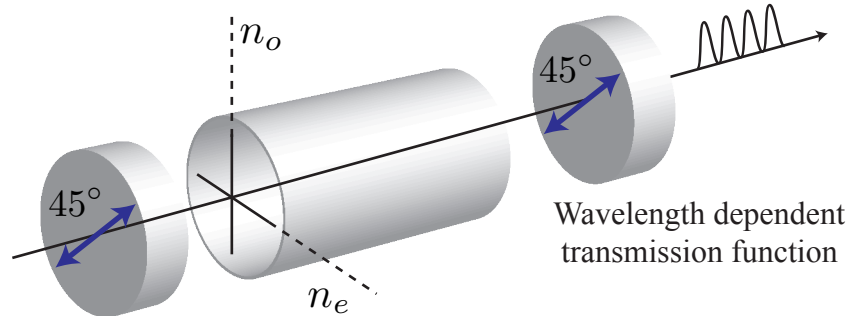


**Figure 3.12:** Lyot filter schematic. A birefringent crystal is placed in between two polarisers.  $n_o$  and  $n_e$  represent the refractive index  $n$  along the fast and the slow axis of the crystal. The transmission function of the second polariser can be approximated with wavelength dependent and phase dependent sinusoidal oscillations. A certain wavelength is transmitted whereas others are blocked.

the strong carrier and the weak sidebands. Tests showed that the use of razor blades for frequency selection purposes introduced spatial fringes and deformed the mode profile of the desired frequency. In addition two spectrometers would be required for operating a single quantum memory. One for generating the signal field and a second for filtering purposes after the actual memory process. This was unfeasible and therefore other alternatives had to be found.

### 3.7.1 Lyot filters

The first idea we had was to use Lyot filters<sup>1</sup> as a spectral filter to separate the sidebands from the carrier frequency. The simplest incarnation of this type of filter can be seen in Figure 3.12. It consists of two polarisers angled at  $45^\circ$  with respect to the ordinary ( $n_o$ ) and extraordinary ( $n_e$ ) axis of a birefringent crystal placed in between the two polarisers. An incident light field, transmitted

<sup>1</sup>A Lyot filter is a frequency filter based on birefringent crystals. It is named after Bernard Lyot, a French astronomer.

through the first polariser, therefore is composed of equal linear polarisations along the ordinary (fast) and the extraordinary (slow) axis of the crystal. The polarisation along the fast axis is transmitted quicker through the crystal than the one along the slow axis. Therefore, and due to dispersion in the crystal, the two polarisations acquire a wavelength-dependent phase shift  $\Delta\phi = 2\pi\Delta nL/\lambda$  relative to each other. When projected onto the same polarisation axis at the second polariser, they interfere. Whether this interference is destructive or constructive only depends on the acquired phase shift  $\Delta\phi$ , affected by the wavelength  $\lambda$  of the incident light, the crystal length  $L$  and the change in refractive index  $\Delta n = n_o - n_e$ . The free spectral range (FSR) of these filters is determined by  $\Delta f = c/L\Delta n$ .

We used a configuration with three calcite crystals, each 3.3 cm long, because it was not possible to purchase a single 10 cm long crystal, necessary for producing a FSR  $\Delta f = 18.4$  GHz. The Lyot filter can be tuned in frequency over one FSR, by tilting one of the calcite crystals slightly, thereby changing the laser beam's optical path length through the crystal.

The filter contrast was measured to be 99%. This was not sufficient for extinguishing the carrier with respect to the sidebands, if the sideband modulation efficiency was 1%. Therefore, the carrier and the sidebands had equal magnitudes and both sidebands were transmitted through the Lyot filter's filtering function (FSR = 18.4 GHz). The FSR could be changed by making the crystal longer, i.e. adding five or six instead of three calcite pieces. However, this would cause other problems like: i) losses arising from reflection and surface roughness of the additional crystals. ii) space constraints on the optical table in the lab. Furthermore if the filter ratio were to be increased, more of these Lyot filters would have to be added in series, multiplying these negative effects.

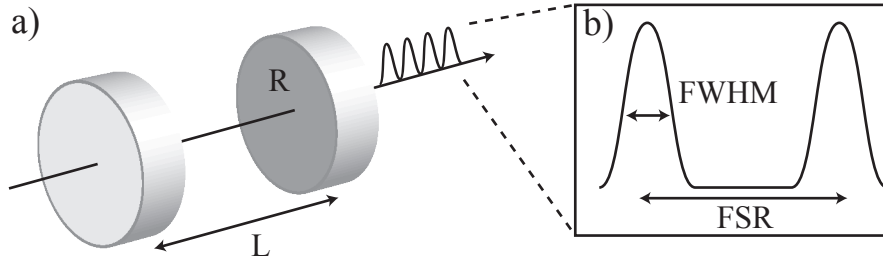


**Figure 3.13:** Fabry Perot etalon schematic. **(a)** Etalon. Two oppositely spaced, a distance  $L$  apart, planar glass plates form the Fabry Perot Resonator. The transmission function versus frequency of the incident light field shows oscillations similar to the ones of the Lyot filter. **(b)** Transmission function in detail. The spacing between the peaks (in frequency) is the free spectral range (FSR). The Full width half maximum (FWHM) of the transmission determines the bandwidth of the transmitted light.

### 3.7.2 Etalons

In parallel to the Lyot filters described in Section 3.7.1, we investigated the option of using etalons<sup>1</sup> to achieve the required spectral filtering. There is a wide variety of etalons available: Solid etalons, air-spaced etalons or even tuneable etalons that can be pressurised on the inside, thereby changing the refractive index between the parallel reflectors. We chose air-spaced etalons because they are unaffected by temperature fluctuations due to their construction from invar<sup>1</sup>.

In principle etalons consist of two parallel glass plates, separated from one another by a distance  $L$ , with a certain transmission on the outer windows and reflectivity  $R$  on the inner windows. A sketch of such a planar cavity can be seen in Figure 3.13 (a). The free spectral range (FSR) of the etalons depends on the separation  $L$  of the glass plates  $\Delta f = c/2L$ , since  $2L$  is the distance an optical wave has to travel in order to make a roundtrip and interfere constructively. Both external windows can be anti reflection coated to minimise losses.

<sup>1</sup>An etalon is a planar Fabry Perot resonator (see Figure 3.13).

<sup>1</sup>Invar is a material with an extremely low thermal expansion coefficient. [113]

Initially we were only concerned with extinguishing the carrier frequency of the EOM, which is why we ordered 6 etalons with a FSR of 18.4 GHz (type 1). The glass plates of these etalons have a separation of  $L = 8.2$  mm. The FWHM of the etalon's transmission function (see Figure 3.13 (b)) matches the 1.5 GHz bandwidth of the 300 ps long tsunami laser pulses (see Section 3.4). The finesse of the etalons is determined by  $\mathcal{F} = 18.4 \text{ GHz}/1.5 \text{ GHz} \sim 12$  but can be also calculated from the reflectivity  $R$  of the glass plates,

$$\mathcal{F} = \frac{\pi\sqrt{R}}{1-R}. \quad (3.3)$$

This sets the reflectivity of the inner surfaces to 78%. The free spectral range of the etalons can be tuned slightly by tilting the etalon with respect to the incident laser beam. This changes the cavity length  $L$  and thereby the FSR of the device.

Type 1 etalons are ideal for extinguishing the carrier frequency after the EOM but they are not capable of extinguishing the second sideband. The reason is that the  $m = 1$  sidebands are separated exactly by the FSR of the transmission function of the type 1 etalons. Therefore both sidebands are transmitted when the etalons are tuned to extinguish the carrier. For this reason we required another type of etalon (type 2) with a FSR of 38.8 GHz. This etalon was used to extinguish the second sideband after the EOM. The type 2 etalon has a reflectivity of 89%, a cavity length of  $L = 3.8$  mm, a transmission function with a FWHM of 1.5 GHz and a Finesse of  $\mathcal{F} \sim 25$ . If we had foreseen that an EOM, producing two sidebands, were to be used to create the 9.2 GHz shifted laser beam, we would have ordered appropriate (type 2) etalons in the first instance. However, this is a nice illustration for the fact that one is always smarter afterwards compared to

before!

Both types of etalons were mounted in large mirror mounts providing tip and tilt flexibility such that their filter function could be frequency-tuned. The etalons were aligned by tuning the laser beam to the frequency that should be transmitted through them. Then the etalons were placed in the beam path, tipping and tilting them such that maximum transmission was obtained. Experimental tests in the lab showed that each of the etalons had a maximum transmission of 50% only, even when tuned into transmission. The extinction ratio of each etalon was 99% (max. transmission compared to max. extinction), which in turn meant that 1% of a an unwanted laser frequency was transmitted through one etalon. The etalons could easily be stringed together in order to improve the total extinction ratio. However, attention had to be paid to the spacing between the etalons because sometimes it happened that two different etalons formed a cavity in between themselves, which affected the transmission of each etalon!

Another remark I would like to make concerns beam pointing. Ideally etalons do not deviate the beam – ideally etalons have 100% transmission... This however, is not feasible in a human laboratory, because it is almost impossible to produce pure plane waves for which the etalon theory is developed. There are imperfections in the surface of the windows and the cavity windows may not be entirely parallel. These issues make it necessary to tip and tilt the etalons in order to achieve a nice transmitted mode. Placing several etalons in series enhances this effect, and the beam pointing and mode profile change significantly. Therefore it is extremely useful to fibre-couple the transmitted beam such that the spatial mode is cleaned up and the beam pointing issue for the subsequent experiment is circumvented.

At this point, all the necessary light fields for implementing a far off-resonant, Raman-based quantum memory have been developed. These are: a pure control field, which is just the laser oscillator itself, a pure signal field, 9.2 GHz frequency-shifted from the control field, which is a frequency modulated control laser field in combination with spectral filters (etalons) and a pure diode laser which can be tuned independently because it is derived from a different laser system.

### 3.7.3 Polarisation

The last important filtering component required for enabling the implementation of the far off-resonant Raman quantum memory was polarisation filtering. In the experiment, the signal and control field polarisations were orthogonal (see Figure 4.10 (a)). This was important for two reasons. First, if the polarisations of the signal field and the control field were not orthogonal, the far off-resonant two-photon Raman interaction would become less efficient and therefore the memory efficiency would suffer<sup>[88]</sup>. This is due to a selection rule arising from destructive interference in the Raman scattering amplitude for co-polarised signal and control fields in case of a large detuning far from resonance. Second, crossed polarisations are crucial for achieving a high enough filtering ratio between the control field and the signal field after the memory in order to isolate the signal field (see Section 4.4). If the polarisations were the same, polarisation filtering could not be used for distinguishing between the two different light fields.

For single photon storage, the signal field/control field ratio was about  $1/10^9$ . If a retrieved single photon were to be detected, the control field would have to be attenuated by a factor of  $> 10^{10}$ . Half of this required extinction ratio could

be achieved using Glan Thompson polarisers<sup>1</sup> offering filtering ratios of  $10^5$  to  $10^6$ . The remaining part was accomplished using Fabry Perot etalons, described in Section 3.7.2. Together, polarisation filtering with a single Glan Thompson polariser and spectral filtering with three Fabry Perot etalons provided a total filtering ratio of  $> 10^{11}$  (see Section 5.1.1). As we will see in Section 5.2, this was good enough for demonstrating operation of the quantum memory at the single photon level with a low unconditional noise floor of  $< 0.25$  photons per pulse, unaffected by control field leakage.

### 3.8 Pockels cell

The Tsunami laser oscillator described in Section 3.3.1 provides 80 million laser pulses in a single second. In other words, there is a laser pulse every 12.5 ns. For implementing a quantum memory this is not really useful for several reasons:

i) Before the quantum memory can be operated, the  $\Lambda$ -level system needs to be prepared in the ground state  $|1\rangle$ . This preparation takes several  $\mu\text{s}$ . The protocol for this will be discussed in Section 3.10. During the preparation cycle there should be no signal or control field pulses.

ii) If arbitrary storage times longer than 12.5 ns are to be implemented, there must not be any control nor signal field pulses during the storage period. They would induce an unwanted readout event (control field only) or, if arriving at the same time (control and signal) another storage event together with a partial readout. It is clear from this perspective that the best thing to do during the storage period is to turn off all possible possible sources of distraction.

---

<sup>1</sup>A Glan Thompson polariser is a high extinction polarisation filter that consists of two right-angled calcite prisms, which are cemented together.

In order to switch off the laser pulses fast enough and select a single pulse only, an optical switch with a rise and fall time on the order of several nanoseconds was required. The solution to this problem was a Pockels cell<sup>1</sup> based on the Pockels effect, an effect that produces birefringence in an optical medium when exposed to a constant or varying electric field. The basic operating principle of a Pockels cell is illustrated in Figure 3.14. The Pockels cell's crystal is made of lithium niobate ( $\text{LiNbO}_3$ ) or potassium titanyl phosphate (KTP). These materials lack inversion symmetry, a necessary requirement for the Pockels effect to occur. The crystal is mounted inside a cylinder with electrodes placed on the top and at the bottom where high voltages can be applied. Once the electric field across the crystal is established, the crystal becomes birefringent with the fast and slow axes defined with respect to the electric field direction. Now the same polarisation rotation, due to a phase shift difference  $\Delta\phi$  between the components of light travelling along the fast and the slow axis of the crystal, as described before in the section on Lyot filters (see Section 3.7.1) takes place. The voltage required to induce a phase change of  $\pi$  is called half-wave voltage  $V_\pi$ . It turns a vertical input polarisation (blue wave) into a horizontal output polarisation (red wave) as illustrated in Figure 3.14.

So far the Pockels cell is nothing but a phase modulator that acts like a waveplate. Placing it in between two crossed polarisers, the first one transmitting vertically polarised light (V) and the second one blocking the V polarisation, turns the Pockels cell into an amplitude modulator that can be used to pick different pulses from the pulse train of the laser oscillator. Only pulses that are switched from V polarisation to H polarisation (horizontally polarised light) are able to

---

<sup>1</sup>A Pockels cell is a voltage controlled waveplate, able to rotate the polarisation of light on nanosecond time scales. It is named after Friedrich C. A. Pockels.

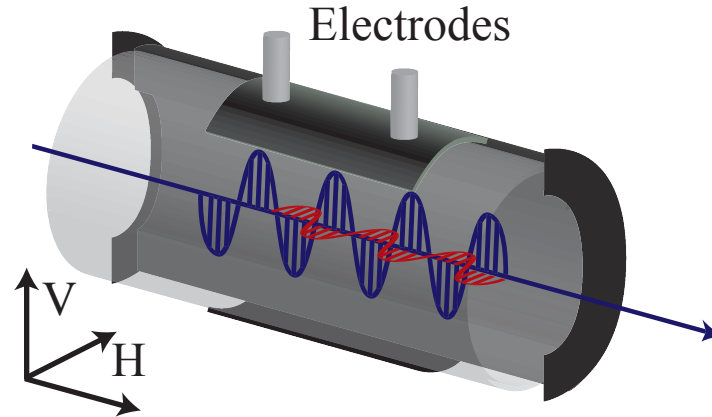


**Figure 3.14:** Pockels cell schematic. An electrically switchable birefringent crystal is placed in between two electrodes (bottom and top) where high voltage can be applied. The polarisation of an incident wave is transformed from vertical (V) to horizontal (H) by introducing a  $\pi$  phase shift of the components of light travelling along the fast and the slow axis of the crystal when an electric field is applied. Adding two crossed polarisers (not shown) turns the phase into an amplitude modulation.

pass through the crossed polariser setup! The switching time of the Pockels cell is fast enough for selecting (picking) a single pulse only. Pockels cells are typically operated with a repetition rate of kHz to MHz. The polarisers for a Pockels cell system switching pulses from a picosecond laser system with a repetition rate of 80 MHz have to be high power compatible. The choice were Glan Laser polarising prisms, because they have an air gap in between the prisms and are not cemented, which makes them suitable for high optical power applications. Their extinction ratio was  $\sim 10^{-5}$ .

Two different Pockels cells systems from Quantum Technology Inc., a US-based company, were used in the quantum memory experiments. The initial experiments were done with an old Pockels cell system (PCS1) that the group inherited from its former location in Rochester, US. PCS1 could be operated with a repetition rate of up to 10 kHz with  $V_{\pi} = 5$  kV. The rise and fall time was on

the order of 3 ns and the extinction ratio was  $\mathcal{R} = 10^{-3}$ . The switching window (duration of the high voltage) could be set from about 2 ns up to 1000 ns (1  $\mu$ s), enabling the selection of single or multiple pulses from the 80 MHz pulse train. The switching capabilities of a Pockels cell system are determined by the high voltage switch (driver) controlling the pulsing of the high voltage. The PCS1 Pockels cell model was QC-8 and the driver model was HVP-525-PN-CE.

After the successful demonstration of the Raman-based quantum memory using PCS1 (see Section 4.5.1), it became clear that arbitrary longer storage times could only be achieved if a different Pockels cell were used (see Section 4.6.2). Therefore, a new Pockels cell system (PCS2), capable of switching twice during one repetition cycle, was purchased. Its operational speed was  $\sim 10$  kHz. It was equipped with a driver allowing for the selection of two arbitrary pulses separated from each other by up to 100  $\mu$ s. The extinction ratio of PCS2 was  $10^{-3}$ . The PCS2 Pockels cell model was QC-8 and the driver was a Starfire 5DM-2-20k, which was used in combination with a divider delay unit DD2-2 that timed the two switching events with respect to each other.

### 3.9 Detection system

So far mainly technical components, like light sources, atomic vapour cells, optical switches, etc., required for implementing a far off-resonant Raman quantum memory in hot caesium vapour were discussed. However, in order to investigate the light-matter-interaction dynamics, different detection systems were essential. These are discussed in this section.

### 3.9.1 Andor camera

The Andor iXon<sup>EM</sup> + 885 camera is a low light EM CCD camera with single-photon sensitivity. The chip has 1004 x 1002 active pixels with a pixel size of 8 x 8  $\mu\text{m}$  each. It was mainly used in combination with the high-resolution spectrometer introduced in Section 3.5 for resolving and detecting the 9.2 GHz (0.02 nm) frequency difference of the signal field and the control field. The most important results achieved with this camera system were the observation of Raman gain and Raman absorption, as can be seen in Section 4.3. These results were the first indication that the far off-resonant Raman approach to quantum memories might be fruitful and that the two-photon interaction between the control field and the signal field was sufficiently strong.

### 3.9.2 Webcam

Small webcams (WCRNS-2936) from PlusCom, sensitive in the near infrared at 852 nm and cheap (£6 per piece), were used for various different purposes:

i) Monitoring fluorescence of caesium atoms exposed to the diode laser radiation. As was described in Section 3.3.2, the diode laser was not frequency-locked and drifted. Therefore, if the fluorescence from a caesium reference cell got weaker or disappeared, we could counteract and moved the external grating of the ECDL slightly to tune the laser emission back to the atomic resonance.

ii) Measuring spatial beam profiles of laser beams. We disassembled the webcam and took off the lens such that the bare chip could be exposed to laser radiation. Tobias Witting, another PhD student in Ian Walmsley's group programmed a Matlab interface for the webcams so that they could be used as spatial

beam profilers. They were capable of realtime beam imaging and could be used for beam characterisation purposes, e.g. carrying out FWHM measurements. This was extremely useful for general alignment purposes, but in particular helped when installing and aligning the EOM (see Section 3.5.1), the AOM (see Section 3.3.2.2) and also for ensuring the beam overlap of the signal field, the control field and the diode laser inside the atomic vapour cell, as will be discussed in Chapter 4.

### 3.9.3 Fast photodiode

The experiment was operated with sub-nanosecond laser pulses. Therefore, it would be nice to have photodiodes with pico-second response times so that the exact pulse shapes could be investigated. However, the group's fastest oscilloscope had a bandwidth of 1 GHz, limiting the speed of usable photo detectors. The DET10A from Thorlabs with a response time of 1 ns and a spectral responsivity of  $\sim 0.5$  A/W at 850 nm was our standard silicon photo detector. It was mainly used to monitor the pulse-picking of the Pockels cell, to ensure that both the signal and the control field arrived at the same time at the vapour cell and to verify that the diode laser was switched off in time before the actual memory interaction was performed.

### 3.9.4 Fast avalanche photo diode

The Thorlabs high-speed avalanche photo detector (APD210) with a bandwidth of 1 GHz was the key to the first successful observation of a single storage and retrieval event demonstrating the functionality of the far off-resonant Raman scheme (see Section 4.5.1). It has a response time of 500 ps, a noise-equivalent

power (NEP)  $\sim 0.4 \text{ pW}/\sqrt{\text{Hz}}$  and a maximum gain of  $2.5 \times 10^5 \text{ V/W}$  at a bandwidth of 1 GHz and a wavelength of 800 nm. This corresponds to a sensitivity of  $\sim 1000$  photons per pulse ( $\sim 100 \text{ pW}$  at 3 kHz repetition rate). It would have been impossible to demonstrate the read-in and the read-out of weak coherent states of light without this fast and sensitive avalanche photo diode.

The observation of Raman gain and Raman absorption, as demonstrated in Section 4.3, was a major step towards implementing a far off-resonant Raman memory in caesium vapour. However, it was far from demonstrating the storage and the retrieval of individual light pulses. The measurements of Raman gain and Raman absorption were carried out using the iXon Andor camera (see Section 3.9.1) by averaging over thousands of pulses. Observing a single storage and retrieval event was impossible with this technology because the shortest accumulation time was  $100 \mu\text{s}$ . Using the regular Thorlabs photodiodes described in Section 3.9.3 was not a real option either, because they were not sensitive enough to measure signal fields containing several thousand photons only.

### 3.10 Optical pumping

Optical pumping is a process in which light excites electrons in an atom or molecule from a low energy level into a higher one. The technique was developed by Alfred Kastler in the early 1950's<sup>[114]</sup> and is commonly used in laser construction for pumping the active laser medium in order to achieve population inversion<sup>[5,109,115]</sup>.

In our case optical pumping is right at the beginning of a series of events that have to happen successively to enable the operation of a quantum memory.

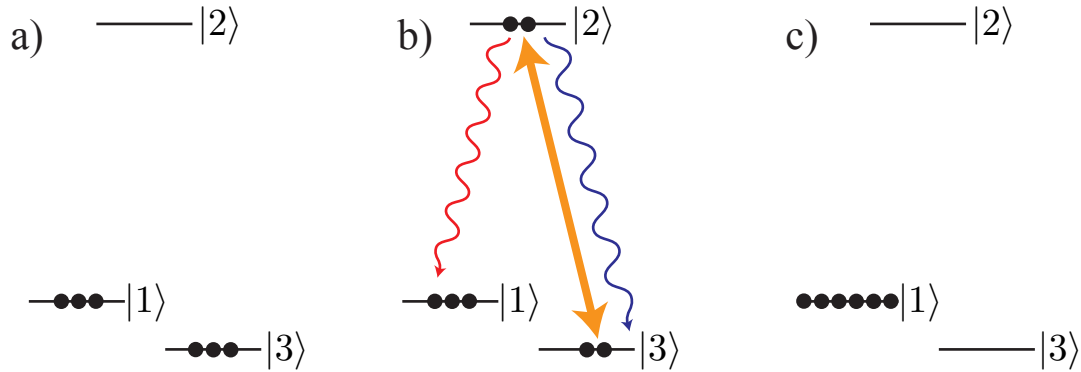


**Figure 3.15:** Optical pumping sequence. **(a)** Individual atoms in the atomic ensemble are equally distributed between the  $\Lambda$ -level system ground states  $|1\rangle$  and  $|3\rangle$ . **(b)** A continuous wave diode laser tuned to the  $|3\rangle - |1\rangle$  transition (orange arrow), resonantly excites atoms to the excited state  $|2\rangle$ . Excited atoms spontaneously decay to the ground state  $|1\rangle$  (red arrow) and to the storage state  $|3\rangle$  (blue arrow). **(c)** After several pumping cycles, the atomic ensemble is prepared in the ground state  $|1\rangle$ .

Only the two hyperfine-split ground states of the  $6S_{1/2}$  shell, as discussed in Sections 3.1 and 3.4, and no magnetic sub levels are considered. In this simple picture of optical pumping (see Figure 3.15), the excited state  $|2\rangle$ , consisting of a manifold of hyperfine split states ( $F = 2, 3, 4, 5$ ), is approximated as a single level. That is because the Doppler broadening in a  $60^\circ\text{C}$  warm caesium vapour spans the entire excited state manifold (see Section 3.2.3). Due to the constant change of directions caused by atomic collisions, each atom experiences the on-resonant diode laser radiation that is impinging on the caesium  $D_2$  line.

In a hot atomic vapour, initially, both the ground state  $|1\rangle$  and the storage state  $|3\rangle$  are equally populated, as illustrated in Figure 3.15 (a). If this caesium  $\Lambda$ -level structure were to be used for memory purposes, it needed to be optically pumped into the ground state  $|1\rangle$ . This is done by applying a cw laser field on resonance with the  $|3\rangle - |2\rangle$  transition, indicated by the orange arrow in Figure 3.15 (b). This laser field transfers some population from the storage state

$|3\rangle$  to the excited state  $|2\rangle$ . The excited state lifetime  $\tau$  of the caesium D<sub>2</sub> line at 852 nm is  $\tau \sim 30$  ns<sup>[95]</sup>. There are two decay channels, one on the  $|2\rangle - |1\rangle$  transition (red wiggled arrow) and one on the  $|2\rangle - |3\rangle$  transition (blue wiggled arrow). Both of them are equally likely, which in other words means that once the atom is excited, there is a 50/50 chance that it relaxes to the state it initially occupied. Therefore, in order to achieve good optical pumping, the cw laser field needs to stay on for quite some time, because the atom takes several cycles before it ends up in the desired state.

Imagine thirty excitation cycles, each with a 50% probability to fall back into the original state. This gives an overall probability of  $10^{-9}$  that at the end an atom still is in its original state. If there were  $10^9$  atoms in the atomic ensemble, one out of all of them would remain in its original state, whereas all the others would get transferred. Assuming an instantaneous excitation process from the ground state to the excited state, gives a lower bound for the total amount of time necessary to transfer all the population from the storage state to the ground state; it is approximately 1  $\mu$ s. Therefore, eventually, the caesium  $\Lambda$ -level system gets prepared in the ground state  $|1\rangle$ , as can be seen in Figure 3.15 (c), paving the ground for further quantum memory action.

Of course in theory everything is a bit easier than in reality and there are several mechanisms that complicate the optical pumping process: i) Collisions between caesium atoms are not spin-preserving and cause a flip of the pumped atoms from the ground to the storage state. Adding a buffer gas, as discussed in Section 3.2.2 reduces this effect, but as the temperature of the vapour cell is increased and more and more caesium atoms are added to the system, it becomes a non-negligible mechanism reducing the optical pumping efficiency. ii)

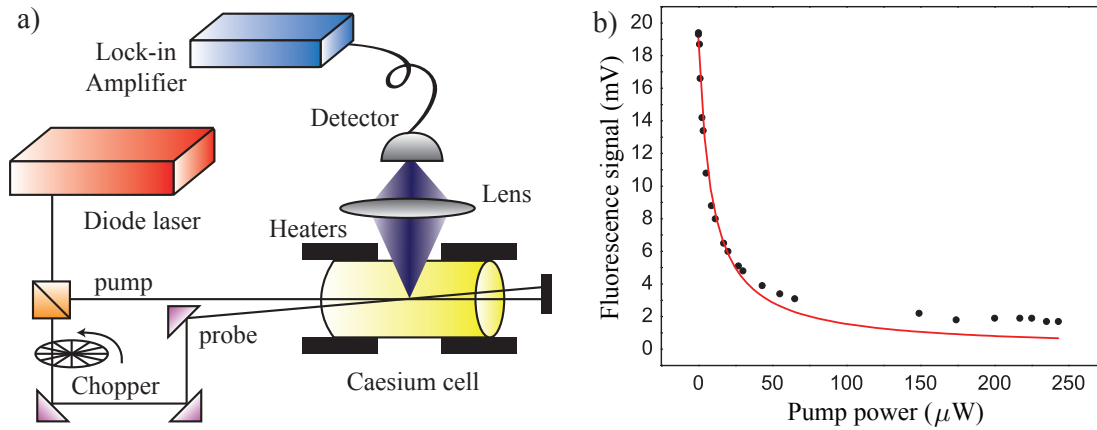


**Figure 3.16:** First optical pumping setup and data. **(a)** The diode laser provides the narrow band pump and probe (modulated by the optical chopper) beams. The vapour cell is heated to  $55^{\circ}\text{C}$  and the fluorescence from the temporally modulated probe beam is detected by time synchronising the detected signal with a lock-in amplifier to the chopper frequency ( $\sim 1\text{ kHz}$ ). The pump beam has a waist of  $\varnothing \sim 3\text{ mm}$  and the probe beam has a waist of  $\varnothing \sim 1.5\text{ mm}$ . **(b)** Optical pumping results. Black dots indicate experimental data and the red curve is a theory fit. The optical pumping efficiency at temperature  $T = 55^{\circ}\text{C}$  is  $\sim 95\%$ .

Radiation trapping is the second effect that occurs at high vapour pressures. If the caesium density is really large, it may happen that already optically pumped atoms are re-pumped from their destination state by fluorescence emitted from other atoms still participating in the optical pumping cycle. This means that light once absorbed from the pump laser and then re-emitted by the excited atoms is trapped within the atomic ensemble, limiting the optical pumping efficiency.

### 3.10.1 Fluorescence measurements

In order to measure the optical pumping efficiency we set up the experiment illustrated in Figure 3.16 (a). A strong pump beam, on resonance with the blue transition of the Cs  $D_2$  line, optically pumped the caesium atoms into the other hyperfine state and a weak probe beam ( $\sim \mu\text{W}$ ), on the same transition as the

pump, but temporally modulated with an optical chopper, probed the remaining, un-pumped population by causing fluorescence at the modulated frequency. This modulated fluorescence signal was then detected with the help of a lock-in amplifier synchronised to the chopper frequency. The result can be seen in Figure 3.16 (b).

Initially, when the pump power was low, the fluorescence signal was high because the population in both hyperfine states of the  $6S_{1/2}$  shell was roughly equal. When the pump power was increased, the fluorescence signal got smaller and smaller, indicating that more and more atoms got pumped into the other hyperfine state and could not participate any more in the resonant excitation process leading to fluorescence. The experimental data is approximated by a theoretical model described in<sup>[116]</sup> and the measured pumping efficiency is  $\sim 95\%$ .

### 3.10.2 Absorption/Transmission measurements

The previous optical pumping experiment was carried out at a very early stage of the memory project. At this time neither Raman gain nor Raman absorption had been observed. As progress was made regarding the implementation of the memory experiment, the experimental setup changed and I decided to carry out a second, slightly different experiment in order to determine the optical pumping efficiency at higher vapour cell temperatures, where the memory was operated. The setup is sketched in Figure 3.17 (a). The Tsunami picosecond laser provided the very weak probe beam ( $3 \mu\text{W}$ ) and the diode laser provided the optical pumping beam (1 mW). Both lasers were tuned to the blue resonance of the caesium  $D_2$  line. The detector measured the transmitted probe signal and the results can be seen in Figure 3.17 (b). The plotted data represent the transmitted fraction

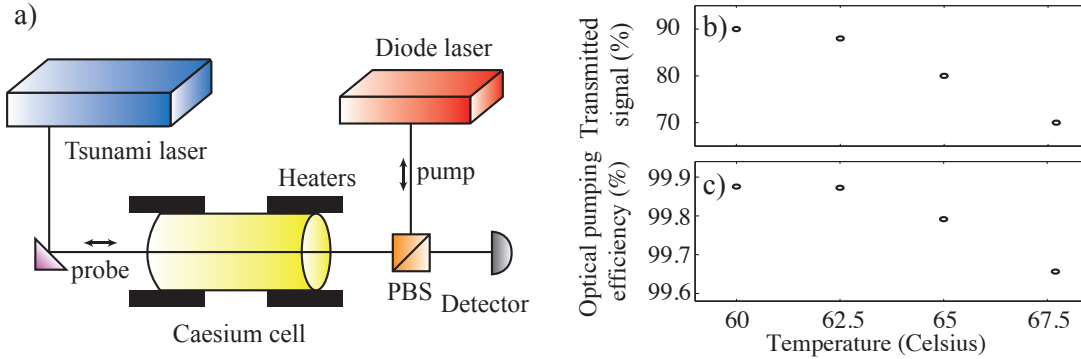


**Figure 3.17:** Second optical pumping experiment and data. **(a)** Experimental setup. The tsunami laser provides the weak probe beam and the diode laser acts as the optical pump. Both laser beams are orthogonally polarised and counter propagating.  $\leftrightarrow$  indicates horizontal and  $\updownarrow$  vertical polarisation. The detector monitors the transmitted probe beam. The pump and the probe laser are both tuned to the blue resonance of the caesium D<sub>2</sub> line. **(b)** Experimental data of the transmitted fraction of the probe beam for different vapour cell temperatures. A 20 GHz off-resonant reference signal sets the 100% benchmark. **(c)** Estimated optical pumping efficiency  $\eta_{\text{pump}}$  derived from probe transmission experiments in (b).

of an on-resonant probe signal while the optical pumping laser was switched on, in comparison to a 20 GHz off-resonant 3  $\mu\text{W}$  probe signal that set the 100% transmission benchmark. We observed that the transmission efficiency of the probe signal got lower with increasing temperature, indicating that the optical pumping efficiency was reduced when the temperature was increased. When the optical pump was switched off, there was no transmission of the probe laser at all, regardless of the set temperature.

We can estimate the optical pumping efficiency (see Figure 3.17 (c)) from the simple model

$$P_{\text{out}} = P_{\text{in}} e^{-d_{\text{exp}}}, \quad (3.4)$$

where  $P_{\text{in}}$  is the incident power of the probe beam,  $P_{\text{out}}$  is the output power of the probe beam and  $d_{\text{exp}}$  is the measured optical depth described in Section 2.8. In

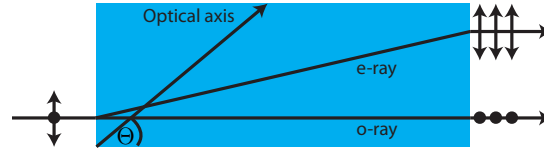


**Figure 3.18:** Polarising beam displacer. An orthogonally polarised input beam is separated into two parallel beams with horizontal ( $\cdot$ ) and vertical ( $\updownarrow$ ) polarisation.  $\Theta = 45^\circ$  is the angle between the optical axis and the light field. The ordinary ray (o-ray) is transmitted straight through the crystal and the extraordinary ray (e-ray) experiences a walk-off. The separation depends on the wavelength of the light and the length of the calcite crystal.

order to relate the experimentally measured optical depth  $d_{exp}$  back to the transmitted probe power, the Doppler and pressure linewidths and the laser bandwidth have to be taken into account. We then use the measured optical depth  $d_{exp}$  to estimate the optical pumping efficiency

$$\eta_{\text{pump}} = 1 - d_{\text{exp}}/d_{\text{th}}, \quad (3.5)$$

where  $d_{\text{th}}$  is the theoretical optical depth defined by Equation 2.27. According to these assumptions, the estimated optical pumping efficiencies  $\eta_{\text{pump}}$  for vapour cell temperatures between  $60^\circ\text{C}$  and  $67.5^\circ\text{C}$  are above 99%.

### 3.11 Polarising beam displacers

A calcite beam displacer splits an orthogonally polarised input beam into two orthogonally polarised parallel output beams. Our beam displacers have the dimensions: 10 mm x 26 mm x 72 mm ( $h \times w \times l$ ) and cause a beam separation of  $\sim 8$  mm. The polarisation extinction ratio is  $\sim 10^5$ , similar to the extinction

ratio of the Glan Thompson and Glan Laser polarisers we use.

As we will see in Chapter 6 and as is illustrated in Figure 6.1 these polarising beam displacers are used for implementing a dual-rail polarisation quantum memory in a single vapour cell. A high polarisation extinction ratio of the PBDs is required to ensure the purity of the of the stored polarisation encoded qubit.



# Chapter 4

## Raman memory realisation

In Chapter 3 all the individual components required for the successful implementation of a Raman quantum memory in a hot caesium vapour were introduced. This chapter illustrates how the basic understanding of the influence of optical pumping on the sidebands and the importance of the temporal overlap between all participating laser pulses eventually lead to the first observation of Raman gain and Raman absorption on the different sidebands. This is a major step towards the realisation of an optical Raman memory in hot caesium vapour, which was finally achieved after upgrading the detection system to a very sensitive time-resolving detector.

### 4.1 Influence of optical pumping on sidebands

In the quest for implementing an optical Raman-based quantum memory the first steps were to identify basic memory-relevant devices and components, understand their interplay and explore a possible experimental setup, like the one illustrated in Figure 4.1 (b). Raman gain and absorption were key features regarding the suc-

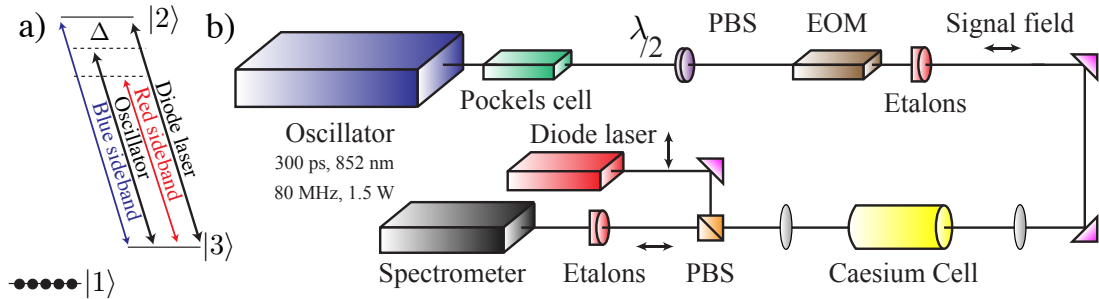


**Figure 4.1:** Optical pumping effects on sidebands. (a) Caesium D<sub>2</sub> line electronic structure and laser fields. (b) Experimental setup for investigating the influence of the diode laser on the sidebands with the spectrometer. The polarisation of the tsunami oscillator is set to horizontal polarisation with a half wave plate ( $\lambda/2$ ), whereas the diode laser has vertical polarisation. The caesium cell is heated to 60°C and the coupling to the spectrometer is in free space.

successful implementation of a Raman-based quantum memory. In order to observe these phenomena in the sidebands generated by the EOM, we first investigated the influence of optical pumping (see Section 3.10) on the sidebands.

The diode laser beam was tuned to the  $|3\rangle - |2\rangle$  transition on the caesium D<sub>2</sub> line at 852 nm (red resonance) and the picosecond oscillator was tuned 9.2 GHz to the red of the  $|3\rangle - |2\rangle$  transition, as can be seen in Figure 4.1 (a). Therefore, the blue sideband generated by the EOM was on resonance with the  $|3\rangle - |2\rangle$  transition and the red sideband was red detuned by 18.4 GHz from the red resonance. The Pockels cell system was set to a pulse-picking mode with a repetition rate of 8 kHz, corresponding to one laser pulse picked every 123  $\mu$ s. The signal field, horizontally polarised ( $\leftrightarrow$ ), and the diode laser, vertically polarised ( $\updownarrow$ ), were counter propagating such that theoretically only the signal field was detected by the spectrometer. The type 1 etalons (see Section 3.7.2) were tuned such that the picosecond oscillator was extinguished and both sidebands were transmitted. When the Pockels cell was set to pick single pulses at the aforementioned rate,

the sideband power was not measurable with our power meter, suggesting that the sideband power was less than  $0.01 \mu\text{W}$ , the sensitivity of the power meter. The power of the diode laser was set to 10 mW. Both beams, the sidebands and the diode laser were focussed into the vapour cell using a 40 cm lens, in order to establish a Rayleigh range<sup>1</sup> that extended the physical dimensions of the vapour cell ( $> 7$  cm). Their beam waists in the vapour cell were  $\sim 1$  mm. The camera of the spectrometer was set to an accumulation time of 0.2 s, which meant that  $\sim 1600$  picked and  $16 \times 10^6$  leak-through sideband pulses were acquired during this time interval. The Pockels cell extinction ratio was  $\mathcal{R} = 1/1000$ , as described before in Section 3.8. Figure 4.2 (a) shows the two sidebands separated from each other by 18.4 GHz. Both sidebands were visible because no vapour cell was present in this experiment. The data in Figure 4.2 (b) represents the case where a vapour cell was placed in the beam path. It was heated to  $60^\circ\text{C}$  and the diode laser was switched off. The blue sideband, which was on resonance with the red resonance, was absorbed due to the high optical depth of the cell at  $60^\circ\text{C}$ ; the red sideband, 18.4 GHz away from the closest resonance, was unaffected. The absorption of the blue sideband was not 100%. Possibly this was due to the fact that the bandwidth of the picosecond pulses was 1.5 GHz and the Doppler-broadened caesium resonance was on the order of 500 MHz (see Section 3.2.3). Figure 4.2 (c) shows the sidebands when the diode laser was turned on and tuned to the  $|3\rangle - |2\rangle$  transition. Therefore the hyperfine state  $|3\rangle$  was optically pumped and most the population was transferred to state  $|1\rangle$ . This explains why the blue sideband was transmitted instead of being absorbed. Figure 4.2 (d) shows the diode laser background. The fact that a diode laser background was observed

---

<sup>1</sup>The Rayleigh range is the distance along the propagation direction of a beam from the waist to the place where the area of the cross section is doubled.

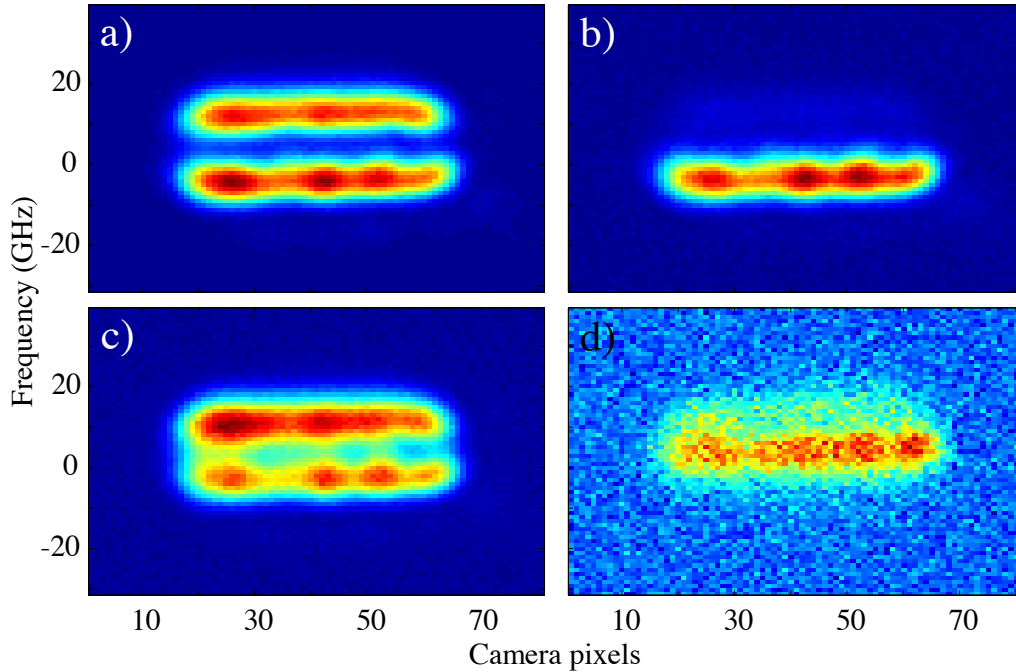


**Figure 4.2:** Sideband absorption study. In these spectrometer images the frequency increases from bottom to top. **(a)** No vapour cell is present; the picosecond carrier is 9.2 GHz red detuned from  $|3\rangle - |2\rangle$  transition; both sidebands are visible. **(b)** The vapour cell is present and is heated to  $60^\circ\text{C}$ ; the blue sideband is absorbed on the red resonance - the red sideband is transmitted. **(c)** The vapour cell is present but is optically pumped by the diode laser that is tuned to the red resonance. Therefore, both sidebands are transmitted. **(d)** Diode laser background.

is surprising, because the diode laser was counter propagating compared to the signal field, for which the detection system was optimised. There are two possible explanations for this phenomenon: i) There was a simple reflection of the diode laser on the vapour cell windows or on the polarising beam splitter cube that coupled the diode laser into the signal field beam path. This reflection could be directed along signal field path and be detected at the camera. ii) During the optical pumping process, the diode laser caused fluorescence of the caesium atoms, which was radiated into all directions.

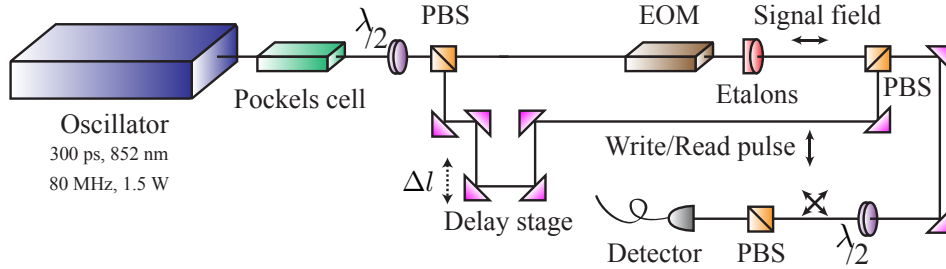


**Figure 4.3:** Experimental pulse overlap verification. The signal field is horizontally polarised  $\leftrightarrow$  and the control field is vertically polarised  $\updownarrow$ .  $\Delta l$  is the delay created by the delay stage. The control field and the signal field are balanced in power and get rotated to a common polarisation before impinging on the detector. The detector measures the interference signal arising due to the path length difference of the signal and the control field.

In future experiments, the diode laser noise could be suppressed by choosing a different detuning of the signal field such that the etalon transmission window does not overlap with the frequency of the fluorescence. Furthermore, a high-quality polarisation prism could be added to the detection beam path, such that only the signal field polarisation is transmitted. These observations give a hint about the problems we might face using an accumulative detection system that averages over many pulses at the same time and is unable to distinguish between individual pulses.

## 4.2 Temporal pulse overlap

In the previous experiment the influence of optical pumping on the red and blue sideband was studied (see Section 4.1). For the implementation of a Raman memory, however, an additional laser field, the control field was required. Therefore, the laser oscillator was split into two orthogonally polarised beam paths, the signal field and the control field, by using a  $\lambda/2$  wave plate and a polarising beam

splitter cube (PBS) as can be seen in Figure 4.3. The signal field was generated by the EOM and spectrally filtered using etalons. The control field passed through a delay stage before being recombined with the signal field at a second PBS. As orthogonal polarisations cannot interfere with one another, a  $\lambda/2$  wave plate rotated both fields by  $45^\circ$  such that they had equal intensities in the same polarisation direction. Then, using another PBS, their polarisations were projected onto a single polarisation state, enabling interferometric measurements.

For a subsequent implementation of a quantum memory, temporal overlap was crucially important. The two photon-transition from the ground state  $|1\rangle$  to the storage state  $|3\rangle$ , as discussed in Chapter 2, was strongly dependent on the timing of the control field and the signal field. Therefore, bad temporal overlap would result in a malfunctioning quantum memory.

### 4.2.1 Interference fringes on camera

Initially, this experiment was set up such that both optical beam paths measured exactly the same distance. A beam profiler was used as a detector, in order to look for spatial fringes created by interference of the signal and the control field. If both beams arrived at the same time, if their spatial profiles were identical and if they were completely in phase, there would be maximal interference. Placing a little glass plate in one of the interferometer arms and tilting it (thereby changing the optical path length in one arm and therefore its phase) should switch the interference from completely constructive to completely destructive. We never managed to observe these total interference effects, but we managed to observe the interference fringes plotted in Figure 4.4.

Figure 4.4 (a) is taken with both optical path lengths equal, as measured

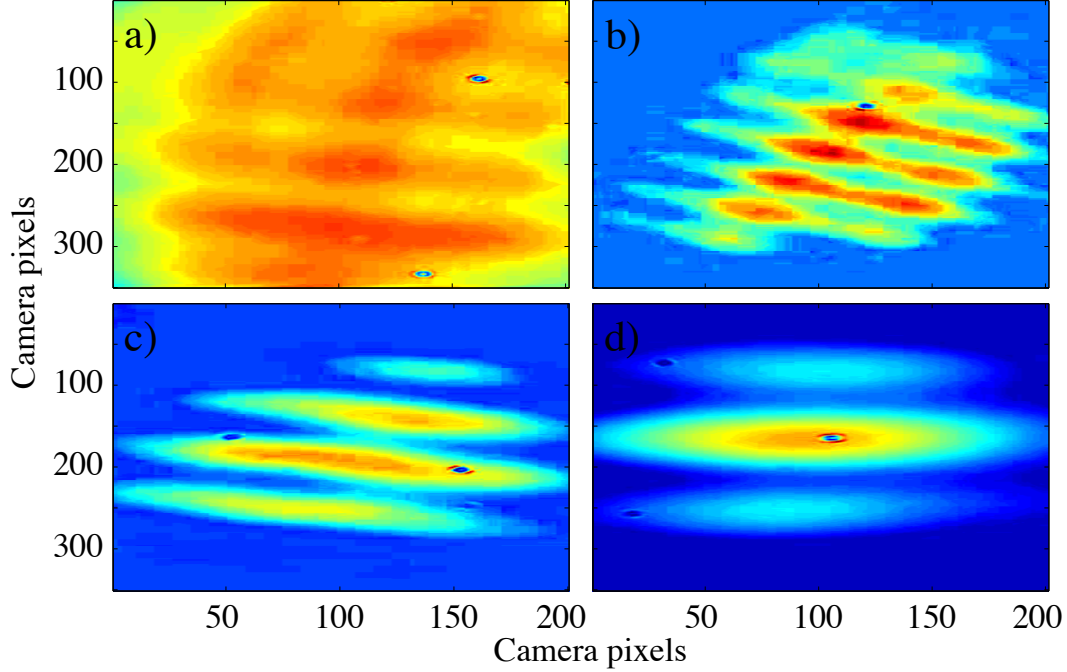


**Figure 4.4:** Spatially measured interference of the signal and the control field. The interference fringes are observed with a beam profiler for different settings of the delay stage  $\Delta l$  in the control field arm of the interferometer illustrated in Figure 4.3. (a)  $\Delta l = 0$  cm. (b)  $\Delta l = 17$  cm. (c)  $\Delta l = 25$  cm. (d)  $\Delta l = 35$  cm.

with a piece of string. Interference fringes are visible but they are not very pronounced. Reasons for this are likely to be optical path length difference and spatial mismatch of the two optical modes. It turns out that the etalons add optical path length to the signal arm of the interferometer. Basically the etalons are two mirrors within which a light field takes multiple round-trips according to the etalons' finesse (see Section 3.7.2). Type 1 etalons with an FSR = 18.4 GHz have a finesse of  $\mathcal{F} = 12$  and a reflector separation of  $d = 8.2$  mm. This leads to an optical path length extension of  $\sim 10$  cm per etalon. The type 2 etalons with an FSR = 38.8 GHz have a separation of  $d = 3.8$  mm and a finesse of  $\mathcal{F} = 25$ . They also add  $\sim 10$  cm to the optical path length. A laser pulse duration of

$t = 300$  ps FWHM corresponds to a length of  $\sim 10$  cm FWHM in free space. Assuming that there was an approximate path length difference of 30 cm in the interferometer arms means that the control and the signal pulses only overlapped at their tails, which could explain the bad visibility observed in Figure 4.4 (a).

Adjusting for the estimated path length difference of the signal field and the control field by using a translation stage in the control field arm lead to a major improvement in the visibility of the interference fringes, as can be seen in Figure 4.4 (b - d). The images all look a bit different, because changing the translation stage changes the beam pointing of the control field and therefore the overlap with the signal field.

This yields a challenge for subsequent experiments, namely to find out what the best timing configuration for implementing an efficient Raman memory is. Furthermore, the far off-resonant Raman memory scheme is based on a two-photon absorption process (see Section 1.2.4). As the signal field experiences a superluminal group velocity during this absorption process, the arrival time of the signal field should be slightly earlier than that of the control field. This procedure ensures that the pulse overlap between the signal field and the control field during the memory interaction process is optimal. If, for example, the signal field and the control field entered the memory cell at the same time, the signal field would “overtake” the control field, thereby reducing the temporal overlap and the memory efficiency.

However, the measurements in Figure 4.4 demonstrate that adjusting the optical path lengths was the right approach for increasing the interference visibility and the temporal pulse overlap between the signal field and the control field.

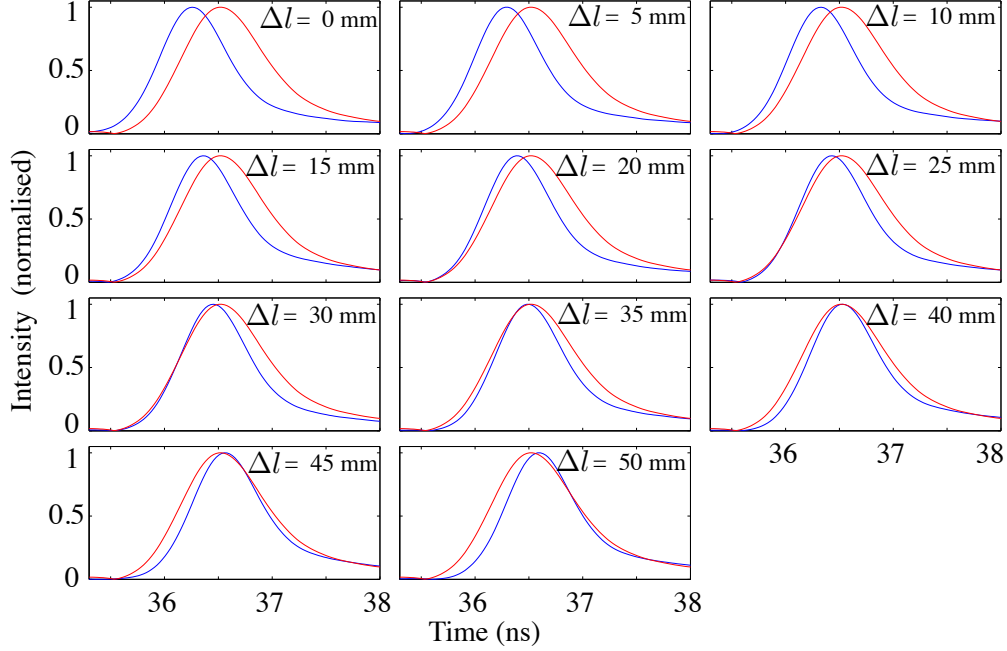


**Figure 4.5:** Temporal beam profiles of the signal and the control field. The profiles are measured with a 1 ns response time photodiode. The signal field is represented by the red curve (fixed in time) and the control field by the blue curve. The arrival time of the control field is varied with a translation stage with a range of  $\Delta l = 50$  mm. The total path delay caused is  $2 \times \Delta l$ . This corresponds to  $\Delta t \sim 330$  picoseconds.

### 4.2.2 Direct temporal measurements on a fast photodiode

Using a fast photodiode was another way to measure the temporal overlap of the laser pulses. Due to the operation with sub-nanosecond laser pulses, and a lack of fast enough photodiodes (see Section 3.9.3) and oscilloscopes, we initially decided not to use this method. However, using a photo diode with a one nanosecond response time provided a reasonable set of measurements illustrating the temporal relation between the signal field and the control field, as can be seen in Figure 4.5. For these measurements, the location of the translation stage was moved to the position where the best interference fringes in the previous experiments using the beam profiler were observed (see Section 4.2.1). The signal field (red curve) and

the control field (blue curve) are displayed in Figure 4.5. The signal field path length was fixed whereas the control field path length was changed by adjusting the delay stage.  $\Delta l$  indicates the setting on the translation stage. For settings of  $\Delta l < 40$  mm the control field arrived before the signal field. At  $\Delta l = 40$  mm the pulse overlap was best and for  $\Delta l > 40$  mm the control field arrived after the signal field. For all subsequent experiments we chose a setting similar to the one displayed for  $\Delta l = 40$  mm where both the signal field and the control field arrived at the same time. Two conclusions can be drawn from the plotted pulse shapes:

i) The measured signals rise nicely, as one would expect from a Gaussian pulse shape, but fall-off rather strangely. The pulses should be symmetric and the observed pulse shape is due to the lack of temporal resolution of our detectors as well as ringing in the detectors. There are two sorts of ringing. One is caused by the detector itself<sup>1</sup> (see Figure 4.11) and the other is caused by pick-up of the high voltage switching of the Pockels cell that selects individual pulses from the 80 MHz pulse train. The displayed images are corrected for background-ringing, where I subtracted the noise arising from the Pockels cell pick up in the absence of a light field.

ii) The signal and the control field have two different FWHMs. This is surprising because both fields are derived from the same laser oscillator. The explanation therefore can only be that some broadening mechanism acts on the signal field, namely the etalons in the signal field arm of the interferometer. All etalons have theoretical FWHM transmission windows of 1.5 GHz, matched to the 1.5 GHz bandwidth of the 300 ps laser pulses (see Section 3.7.2). However, if the etalon

---

<sup>1</sup>If a Gaussian-like signal is detected and displayed on the oscilloscope, the amplitude does not return to zero immediately, but turns negative and oscillates back to zero in a damped way.

transmission window does not match the spectral pulse shape of modulated sidebands exactly, the laser pulses get truncated in the frequency domain. In this case, the transmitted pulses will appear spectrally narrower and temporally broader compared to the incident signal field and the unfiltered control field.

### 4.3 Observation of Raman gain and absorption

Previously, I studied the sidebands close to resonance, observed their partial absorption and response to optical pumping (see Section 4.1) and investigated the importance of the temporal pulse overlap (see Section 4.2). The next step towards the realisation of a Raman-based quantum memory was the observation of Raman absorption and Raman gain.

#### 4.3.1 Gain and absorption on red and blue sideband

As discussed in Section 3.6, two sidebands result in a double  $\Lambda$ -scheme with a two-photon resonance for the blue and the red sideband. For the next experiments the laser oscillator was tuned 15 GHz to the blue of the blue resonance ( $|1\rangle - |2\rangle$  transition), such that there was a two-photon resonance for the red sideband at  $\Delta_{\text{red}} = 15$  GHz and a two-photon resonance for the blue sideband at  $\Delta_{\text{blue}} = 24$  GHz, as illustrated in Figure 4.6 (a). The diode laser was tuned to the red resonance ( $|3\rangle - |2\rangle$  transition) and pumped all the atoms from state  $|3\rangle$  into state  $|1\rangle$ . Therefore, the blue sideband should experience Raman absorption and be reduced whereas the red sideband should experience Raman gain and be amplified in the presence of the strong control field (black arrows) mediating the two-photon transitions.

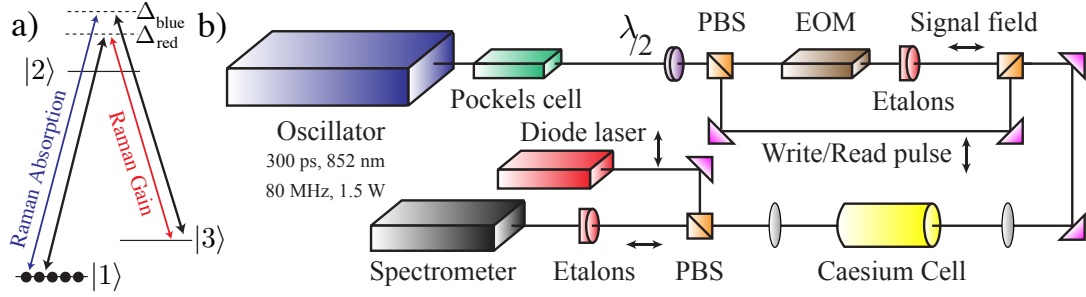


**Figure 4.6:** Raman gain and absorption scheme and setup. **(a)** Double  $\Lambda$ -scheme with Raman gain and Raman absorption channel. The ensemble is prepared in state  $|1\rangle$  by optical pumping. **(b)** Experimental setup for Raman gain and Raman absorption measurements. The etalons after the EOM consist of three type 1 etalons with an FSR = 18.4 GHz.

The experimental setup is illustrated in Figure 4.6 (b). Most of the laser oscillator power was diverted into the control field arm (write/read pulse) with a measured power of  $91.8 \mu\text{W}$  before the vapour cell. When the Pockels cell was set to pick zero pulses, the power meter still read  $56.5 \mu\text{W}$  due to the Pockels cell leak of the whole pulse train described in Section 3.8. This means that  $35.3 \mu\text{W}$  belonged to the picked pulses corresponding to a pulse energy of 5 nJ at a Pockels cell repetition rate of 6 kHz. Therefore the averaged ratio of the picked pulses to the leaked pulses was  $\mathcal{R} \sim 3/5^1$ . The sidebands could not be detected on the power meter, which indicated that their power was  $< 0.01 \mu\text{W}$ . Both the control field and the sidebands were focussed to a beam waist of  $\varnothing \sim 700 \mu\text{m}$  inside the vapour cell. The counter propagating diode laser had a beam diameter of  $\varnothing \sim 1.5 \text{ mm}$  and a power of 6 mW. The vapour cell was heated to  $50^\circ\text{C}$  and one type 1 etalon with an FSR of 18.4 GHz was placed in front of the entrance to the spectrometer. The etalon was tuned to sideband transmission and blocked the

<sup>1</sup> Here, the overall effect on the sidebands was observed. For subsequent memory operation, the picked pulses had to be isolated from the leaked pulses. This would be difficult if the spectrometer were to be used as a detection system.

laser oscillator.

The first observation of Raman gain and absorption is illustrated in Figure 4.7. These images are integrated perpendicular to the frequency axis of the usual spectrometer images (see Figure 4.2). Figure 4.7 (a) shows the blue and the red sidebands blue-detuned by 24 GHz and 6 GHz from the blue resonance ( $|1\rangle - |2\rangle$  transition), which sets the zero on the frequency axis. Figure 4.7 (b) is a differential image between sidebands-only minus sidebands with the control field turned on. The effect of the control field was that both sidebands got a little bit more absorbed, which is why the differential signal is positive for both sidebands. The reason for this is optical pumping caused by the strong control field. Figure 4.7 (c) is a differential image between sidebands-only minus the sidebands with the diode laser turned on. The diode laser was tuned to the red resonance ( $|3\rangle - |2\rangle$  transition) and shovelled population from state  $|3\rangle$  to state  $|1\rangle$ . Therefore, the red sideband, which was closer to the blue resonance than the blue sideband, got absorbed a bit more, which is why the differential signal is positive. The blue sideband was rather unaffected and therefore the differential signal is close to zero.

So far, these observations do not reveal any new physics. However, the interesting part follows in Figure 4.7 (d), which is another differential image; but this time between the sidebands-only minus the sidebands with control field and diode laser turned on at the same time. If both processes described in cases (b) and (c) took place independently of each other, it would be expected that they add up. Therefore the differential signal should look similar to both. Surprisingly, though, the opposite happens! The red sideband got stronger (amplification), which is why the differential signal is negative and the blue sideband got weaker

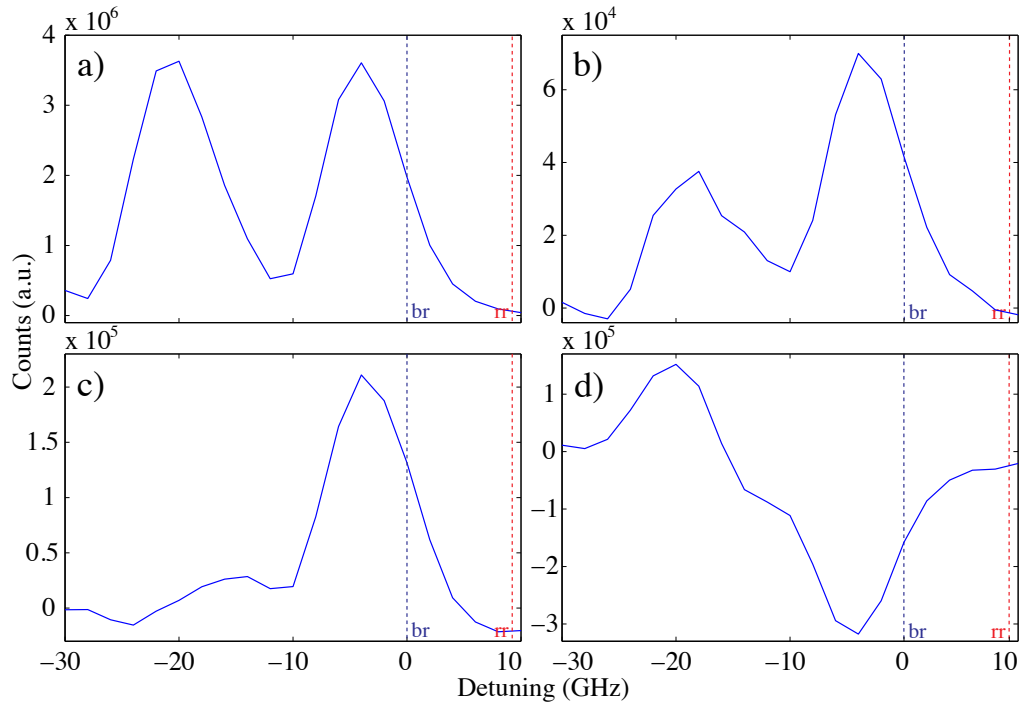


**Figure 4.7:** Raman gain and Raman absorption on both sidebands. **(a)** The blue and the red sidebands are 24 GHz and 6 GHz blue-detuned from the blue resonance (br). The red resonance is indicated by rr. **(b)** Differential signal between sidebands-only and sidebands with control field. **(c)** Differential signal between sidebands-only and sidebands with diode laser. **(d)** Differential signal between sidebands-only and sidebands with control field and diode laser. The blue sideband experiences Raman absorption and the red sideband experiences Raman gain.

(absorption), resulting in a positive difference. It is important here to take a close look at the scales of the different plots; it is impossible to achieve the measured values of plot (d) by just adding the different values of plot (b) and (c).

This is a clear indication that some other mechanisms, namely Raman interactions, were active in the case when all laser fields were switched on at the same time. The red sideband experienced *Raman absorption* and the blue sideband experienced *Raman gain* when the  $\Lambda$ -system was prepared in the ground state  $|1\rangle$  as illustrated in Figure 4.6 (a). Raman absorption was a prerequisite for a subse-

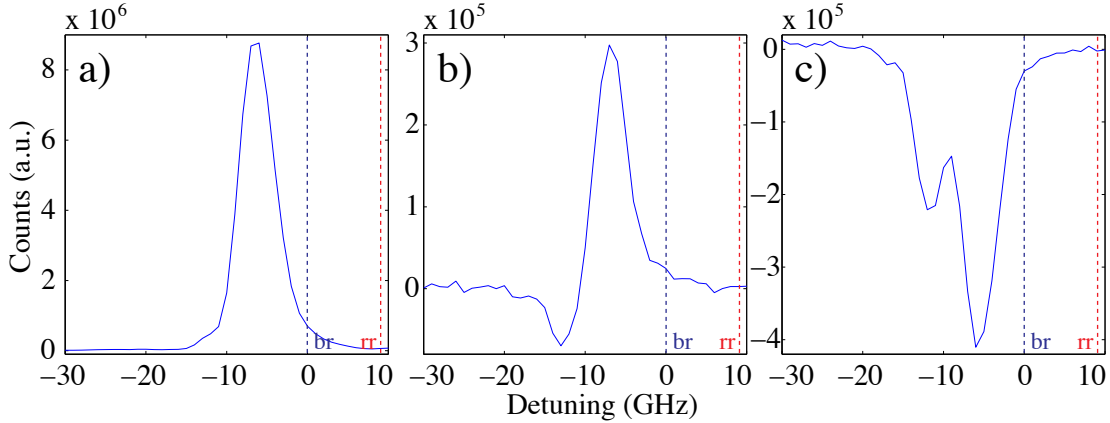


**Figure 4.8:** Raman gain and absorption on a single sideband. Raman gain or Raman absorption depend on the setting of the optical pump laser. (a) The red sideband is 6 GHz blue-detuned from the blue resonance (br). The red resonance is indicated by rr. (b) Differential signal of the red sideband only and the red sideband with the control field and the diode laser pumping on the blue resonance. (c) Differential signal of the red sideband only and the red sideband with the control field and the diode laser pumping on the red resonance.

quent Raman-based quantum memory and therefore these observations indicated that we were on the right track to implementing a Raman-based memory.

### 4.3.2 Gain and absorption on a single sideband

As we have seen in Section 4.3.1, two sidebands enable two Raman channels, one for Raman absorption and one for Raman gain. The physics would be greatly simplified if there were a single sideband only. In order to extinguish one of the two Raman channels, one of the type 1 etalons with an FSR = 18.4 GHz after the EOM (see Figure 4.6 (b)) was replaced by a type 2 etalon with an FSR = 38.8 GHz. With this configuration it was possible to extinguish one of the two sidebands as well as the carrier frequency completely, as can be seen in Figure 4.8 (a). The laser oscillator was tuned 15 GHz to the blue from the

$|1\rangle - |2\rangle$  transition. The type 2 etalon with an FSR of 38.8 GHz was set such that it transmitted only the red sideband, which was 6 GHz detuned to the blue from the  $|1\rangle - |2\rangle$  transition, and extinguished the blue sideband. In Figure 4.8 (b) the differential signal between the red sideband only and the red sideband with the control field and the diode laser pumping the blue resonance ( $|1\rangle - |2\rangle$  transition) can be seen. This caused Raman absorption on the red sideband and therefore the differential signal is positive. The little dip below zero at  $-14$  GHz is related to imperfect filtering of the strong control field. Figure 4.8 (c) illustrates Raman gain on the red sideband. Here, the diode laser was tuned to the red resonance instead of the blue resonance. For this reason the opposite two-photon transition compared to the one in Figure 4.8 (b) took place and therefore the differential signal in Figure 4.7 (c) is negative. The dip below zero at  $-14$  GHz has the same origin as in the Raman absorption case: imperfect filtering of the strong control field.

The conclusion from these measurements was that the observation of Raman gain or Raman absorption only depended on the tuning of the optical pump laser in addition to the presence of the control field. In subsequent experiments the leakage of the strong control field was eliminated by the installation of additional etalons in front of the detection system and the use of wave plates designed for 852 nm. It was observed that placing the cell in the optical beam path rotated the polarisation of both the signal and the control field slightly, which caused less transmission of the signal field and more, unwanted transmission of the control field through the polarising optics in front of the detection system. This effect was due to birefringence in the vapour cell windows but could be compensated by installing and adjusting a  $\lambda/2$  and a  $\lambda/4$  wave plate after the vapour cell that

minimised the control field leakage.

### 4.3.3 Gain and absorption power study

For the following experiments, the experimental setup was the same as the one illustrated in Figure 4.6 (b). The laser oscillator was tuned 18 GHz to the red of the red resonance, i.e. the  $|2\rangle - |3\rangle$  transition in Figure 4.6 (a). The etalons after the EOM were tuned such that they only transmitted the blue sideband, which was located 9 GHz to the red of the red resonance (see Figure 4.9). This set of measurements investigated the Raman gain and the Raman absorption depending on the control field pulse energy, which was initially set to 5 nJ. The experiment was repeated at a rate of 6 kHz. The diode laser had a power of 20 mW and was tuned either to the blue or to the red resonance. The detection system (Andor camera) was programmed to accumulate data for 0.1 s during 100 different cycles and to display the average. The caesium cell was heated to 60°C and the physical beam sizes were the same as mentioned before in Section 4.3.1.

Figure 4.9 (a) shows  $\sim 17\%$  Raman absorption on the blue sideband. Here, the diode laser (pumping the red resonance) and the control field were both turned on at the same time. In Figure 4.9 (b) the opposite effect, Raman gain, takes place. Here, the diode laser pumped the blue resonance and together with the control field turned on, the result was a signal increase of  $\sim 22\%$  compared to the sideband itself without any other laser fields. Figure 4.9 (c) shows a control field pulse energy study of Raman absorption and Figure 4.9 (d) shows a control field pulse energy study of Raman gain. The control field energy was increased from 0 nJ to 5 nJ successively and the change of sideband transmission was measured. All displayed percentages were calculated by summing over all counts

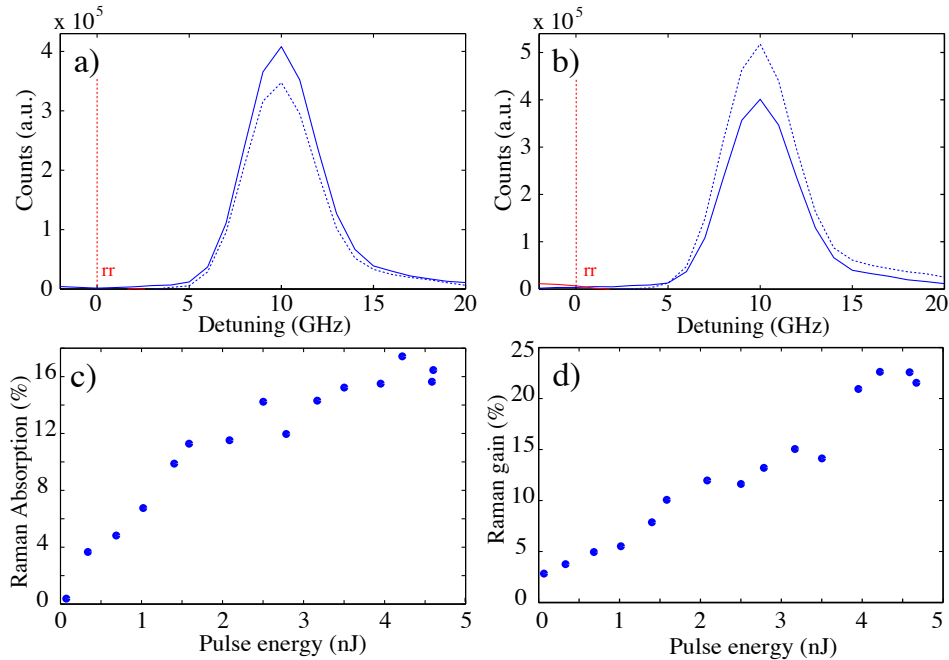


**Figure 4.9:** Raman gain and absorption dependence on control field pulse energy. **(a)** Raman absorption ( $\sim 17\%$ ) if diode laser is tuned to the red resonance. Frequency axis zeroed at location of red resonance (rr). **(b)** Raman gain ( $\sim 22\%$ ) if diode laser is tuned to the blue resonance. **(a) & (b)** Solid line: Transmission of the blue sideband alone. Dashed line: Transmission of the blue sideband with the control field and the diode laser turned on. **(c)** Raman absorption vs. control field pulse energy. **(d)** Raman gain vs. control field pulse energy. Solid dots indicate experimental data.

of the unaffected sideband and subtracting it from the total counts of the affected sideband in the presence of the control field and the diode laser.

In the spontaneous Raman regime the increase in gain and absorption should be linear with the control field energy<sup>[83]</sup>. Raman absorption and Raman gain increased with increasing pulse energy of the control field as Figures 4.9 (c) & (d) illustrate. This suggested that subsequent experiments should be operated with the highest possible control field energy, in order to function most efficiently.

#### 4.3.4 Conclusion of Raman gain and absorption studies

In the previous Section 4.3.3 we managed to demonstrate Raman gain and Raman absorption. This was a major step towards the realisation of a Raman-based quantum memory, because Raman absorption indicated that some of the incident light remained inside the atomic medium and did not exit the vapour cell.

The experimental setup we developed offered enough flexibility to generate the precise frequencies required to observe two-photon processes. However, the measurements made with the Andor camera, averaging over time scales  $\sim 1$  s, included picked, memory-relevant pulses as well as a large fraction of leak-through pulses, strongly attenuated by the Pockels cell, from the 80 MHz pulse train (see Section 3.8). The shortest common acquisition time at which the Andor camera and the Pockels cell could operate together was 100  $\mu$ s. The Pockels cell generated pulses at its maximum rate (10 kHz) but during every 100  $\mu$ s acquisition interval, one picked pulse as well as 8000 leaked pulses were present. Even though every leaked pulse was 1000 times smaller compared to the picked pulse, it was the number of leaked pulses that posed the problem.

In order to isolate single signal pulses, it was necessary to have a very sensitive detector with a high enough temporal resolution on the order of nanoseconds (see Section 3.9.4). As we will see in Section 4.5.1, upgrading the experiment with this sort of detector was the last major hurdle before the first observation of Raman storage and Raman retrieval of single signal pulses was achieved.

## 4.4 Experimental setup

For the previous experiments, which investigated Raman gain and Raman absorption, the control field and the signal field arms of the interferometer were adjusted such that the path length difference  $\Delta l$  between the two arms was exactly zero (see Section 4.3). This meant that whenever a signal pulse arrived at the vapour cell, a control pulse also arrived at the vapour cell. This configuration was fine for an initial storage experiment, but what would happen when the next control field and signal field arrived? Would another storage event take place and/or would a spin wave coherence be left in the atomic ensemble from the previous set of pulses, that then interacted somehow with the current set of pulses, causing storage and maybe readout at the same time?

Ideally, the signal field should be switched off during the readout event, in order to avoid this dilemma of simultaneous storage and readout. How long would the atomic spin wave excitation actually last inside our atomic ensemble? Appropriate timing for the retrieval event was important, because if decoherence<sup>1</sup> were strong, there would not be anything left to retrieve at the chosen time.

These were the main questions that went through our minds when we thought about implementing the last stage of the experiment for storage and retrieval of weak optical pulses. The experimental setup we decided to try can be seen in Figure 4.10 (a). The majority of the devices used in this setup were introduced previously in Chapter 3. The most important detail about this diagram is the timing sequence of the laser pulses. The Pockels cell was set to pick two laser pulses at a time with a repetition rate of 6 kHz. They were split into two arms,

---

<sup>1</sup>Decoherence is the effect that destroys the atomic spin wave coherence inside the atomic ensemble. Different decoherence mechanisms are going to be discussed in Section 4.6.

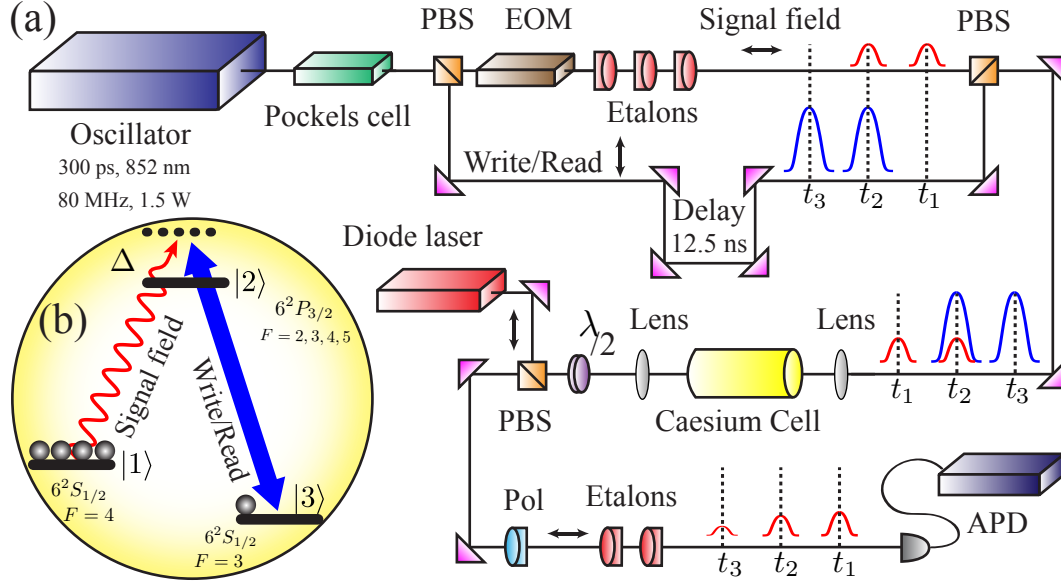


**Figure 4.10:** Quantum memory setup and  $\Lambda$ -level scheme. (a) Experimental setup. The Pockels cell picks two consecutive pulses from the pulse train. A 12.5 ns delay is introduced in the write/read path. Three different time bins are identified:  $t_1$ , which is irrelevant for the memory;  $t_2$ , where the storage happens and  $t_3$ , where the readout takes place. Two type 1 etalons with an FSR of 18.4 GHz and one type 2 etalon with an FSR of 38.8 GHz are used after the EOM. Two type 1 etalons are installed in front of the fast avalanche photodiode (APD). The vapour cell is heated to 55°C. A polarising beam splitter (PBS) and a Glan-Thompson polarising prism (Pol) are used for polarisation filtering. The signal ( $\leftrightarrow$ ) and the control field ( $\updownarrow$ ) have orthogonal polarisations. (b)  $\Lambda$ -level system. The laser oscillator (blue arrow) is tuned 18 GHz to the blue of the  $|3\rangle - |2\rangle$  transition. The red sideband (red arrow) is in a two photon resonance 9 GHz blue detuned from the  $|1\rangle - |2\rangle$  transition. The diode laser is tuned to the  $|3\rangle - |2\rangle$  transition, preparing the  $\Lambda$ -system in the ground state  $|1\rangle$ .

the signal field and the control field, which were orthogonally polarised. Signal fields were generated by the EOM for both carrier pulses at  $t = t_1$  and  $t = t_2$ . A optical delay of 12.5 ns, corresponding to a free space path length difference of  $\Delta l = 3.75$  m, was added to the control field arm, making it longer than the signal field arm by exactly the separation between two subsequent laser pulses. This way, the two control field pulses were delayed such that the first control field pulse overlapped in time precisely with the second signal field pulse ( $t_2$ ) and the

second control field pulse arrived 12.5 ns after the second signal field pulse at  $t = t_3$ . This little trick arranged for a clean storage event at  $t = t_2$  and a clean readout event at  $t = t_3$ . The first signal pulse at  $t = t_1$  just passed the cell due to its off-resonant character and did not affect the memory behaviour.

Using this configuration enabled the first operation of a deterministic Raman-based optical memory, but it limited the flexibility regarding storage time of the memory, fixing it to 12.5 ns. As we will see in Section 4.6, this constraint was soon lifted by upgrading the experiment with a new Pockels cell system (see Section 3.8) and a fast RF switch (see Section 3.5.2).

## 4.5 Results

### 4.5.1 First observation of storage and retrieval

The first experimental observation of storage and retrieval of optical light pulses dates back to the evening of August 5th, 2009 around 10pm. After upgrading the experiment with the new fast APD (see Section 3.9.4) during the course of the day and carrying out some preliminary tests, the experiment was set up and ready to go in the evening hours. I remember quite well that nobody else was in the lab and that I started jumping around like crazy when I saw the graphs illustrated in Figure 4.11 on the oscilloscope. I wasn't sure whether or not I was dreaming but worried that what I saw might not be there for a lot longer. So I started looking for somebody else to have a look at the traces that the oscilloscope displayed. The office was completely empty, too, at that time of the evening, but upstairs, next to the Townsend lab, I found Tobias Witting in his office, who became the first witness of the Raman-based optical memory.

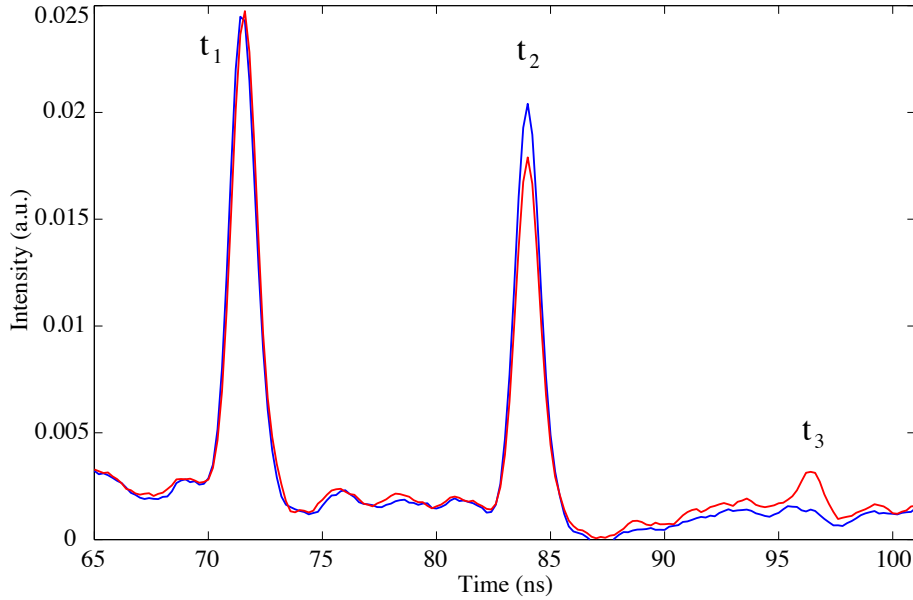


**Figure 4.11:** First observed memory operation. The blue/red curve represent the signal field without/with the control field and the diode laser. At  $t = t_1$  nothing happens, the signal is only transmitted through the cell due to its far off-resonant character. At  $t = t_2$  there is partial absorption of the signal field (storage process). At  $t = t_3$  the stored excitation is retrieved from the memory (readout event).

The experimental settings for this data were the following: The oscillator, and therefore the control field, was tuned 18 GHz to the blue of the blue resonance ( $|3\rangle - |2\rangle$  transition; see Figure 4.10 (b)). The etalons in the signal field path were tuned for transmission of the red sideband, located 9 GHz to the blue of the blue resonance, establishing a two-photon transition with the control field, as illustrated in Figure 4.10 (b). The control field pulses contained an energy of 5 nJ each and the signal pulses consisted of  $\sim 10000$  photons corresponding to an energy of  $\sim 2$  fJ. The diode laser, tuned to pump the blue resonance, had a power of 1 mW and was continuously switched on. As will be discussed in Section 4.6.2.3, permanent diode laser radiation during the storage interval has a negative effect on the spin wave excitation, especially for longer storage times.

Therefore it is best to turn off the diode laser in subsequent experiments before the storage process begins. However, for a storage time of 12.5 ns this effect is almost negligible (see Section 4.6.2.3). The cell was heated to 55°C and the beams were focussed into the vapour cell and re-collimated afterwards with a 1/1 telescope, consisting of two 30 cm lenses. The beam diameters of the control field and the signal field inside in the interaction region were  $\varnothing \sim 500 \mu\text{m}$ ; the diode laser beam waist was  $\varnothing \sim 1.5 \text{ mm}$ .

The storage and retrieval experiment, which was carried out with these settings, is presented in Figure 4.11. The blue curve illustrates the incident signal field pulses that were generated by the Pockels cell and the EOM without a memory interaction, where no control or diode laser fields were switched on. Both pulses, due to their off-resonant character, were transmitted without absorption. The reason why they did not have the same height was due to the detector response, which offset the zero level a bit whenever a pulse was detected. Also, the small oscillations at the bottom of the curves arose from detector ringing that could be considered as noise (see Section 4.2.2). It was verified that, if the control field and the diode laser were switched on without a signal field, the APD detector would not register any signal. This indicated that the extinction of the control field and the diode laser by the polarising optics and the etalons (see Figure 4.10 (a)) was better than the sensitivity of the APD detector. Therefore, when a single storage or retrieval event with a temporal resolution of 1 nanosecond was observed, there was no background noise at all, neither from the strong control field nor from the permanently switched on diode laser. Compare this to the case where the Andor camera was used as a detection system and only longer periods of time including multiple events could be observed (see Section 4.3.2).

However, the interesting part of the experiment took place when the signal field, the control field and the diode laser were all switched on simultaneously (Red curve in Figure 4.10). The first signal pulse at  $t = t_1$  passed the cell without any interaction, because at its arrival time no control field was present that could mediate a storage process. At time  $t = t_2$  though, the presence of a control field pulse mapped part of the signal field into a spin wave excitation inside the atomic caesium ensemble (see Section 1.2.4), which was why the transmitted red signal was less compared to the blue signal, where no control field was present. This event was the storage event of the memory. At  $t = t_3$  a signal was detected where none was before. This was the retrieved signal, which originated from the extraction of the spin wave excitation from the caesium ensemble and its reconversion into a light pulse. The storage time was precisely 12.5 ns, corresponding exactly to the duration of two subsequent laser pulses from the oscillator. The total efficiency of the memory at this stage was quite low, but as we will see in the next sections and chapters, continuous progress was made in improving the memory efficiency and lifetime.

### 4.5.2 Memory parameter-space investigation

After the storage and the retrieval of an optical pulse were observed for the first time (see Section 4.5.1), understanding the memory's response to different parameters like vapour cell temperature, signal field power and control field power was next on the to do list. For these measurements the spatial and temporal pulse overlap, as well as the beam waist of the different laser beams in the interaction region was changed and optimised for achieving maximum efficiencies.

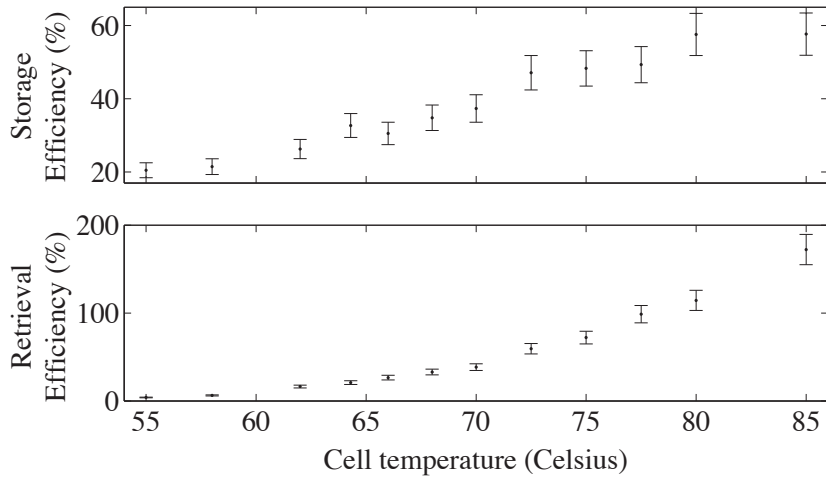


**Figure 4.12:** Temperature dependence of the optical memory. **(a)** Storage efficiency of the memory vs. cell temperature. **(b)** Retrieval efficiency of the memory vs. cell temperature. Error bars indicate the standard error of the mean. Data points are calculated by integrating over the temporal trace of the stored and the retrieved signal pulses and normalising these values with respect to the integral over a signal field that is completely transmitted when the memory is switched off.

#### 4.5.2.1 Vapour cell temperature run

At first I decided to investigate how the memory efficiency  $\eta$  depended on the temperature of the vapour cell. The outcome of these measurements can be seen in Figure 4.12. As the temperature of the vapour cell was increased, more caesium atoms  $N_A$  were added to the atomic ensemble, with which the light fields interacted. This increased the optical depth  $d$  (see Section 2.8) which in turn made the Raman memory more efficient. However, as was discussed in Section 3.10 about optical pumping, it became more difficult to optically prepare the  $\Lambda$ -level system in the ground state the warmer the vapour cell got. The observed storage efficiency, illustrated in Figure 4.12 (a), clearly demonstrated this behaviour and a maximum of  $\sim 60\%$  of the incoming signal field was stored at a temperature of  $\sim 80^\circ\text{C}$ . A closer look at Figure 4.12 (b) reveals a very interesting

phenomenon, namely retrieval efficiencies of more than 100%. Of course, from a perspective of storing and retrieving a light field, this is not feasible at all, but as the memory interaction was based on Raman transitions, it is possible that the retrieved signal experienced Raman gain in regimes of high vapour pressures where optical pumping was inefficient. Here, enough population was left unpumped in the storage state, which, if exposed to a control field and a signal field, led to stimulated Stokes scattering into the signal mode. The initial signal field acted as a seed for this two-photon process. The retrieval efficiency curve exhibits a linear character at low temperatures and turns into an exponential curve at temperatures above 70°C (see Figure 4.12 (b)). It is possible that this amplified Raman scattering process is coherent, which should be investigated further in the future. We conclude from this experiment that it is best to operate the Raman memory in the linear regime, where no amplification effects occur that could lead to a misinterpretation of the memory behaviour.

#### 4.5.2.2 Control field pulse energy dependence

Next we investigated the behaviour of the memory efficiency with respect to the control pulse energy (see Equation 2.23 in Section 2.7). For the following experiments the vapour cell was heated to 62.5°C. This temperature was chosen in order to ensure that the memory was operated in the linear regime, as discussed before in Section 4.5.2.1.

Experimental data for the storage and retrieval processes are displayed in Figure 4.13, showing retrieval of the stored information 12.5 ns after storage of the signal pulse ( $t = 0$ ). The storage and retrieval efficiencies depend on the write and read pulse energy: when zero, 100% of the incident signal field is transmitted, by

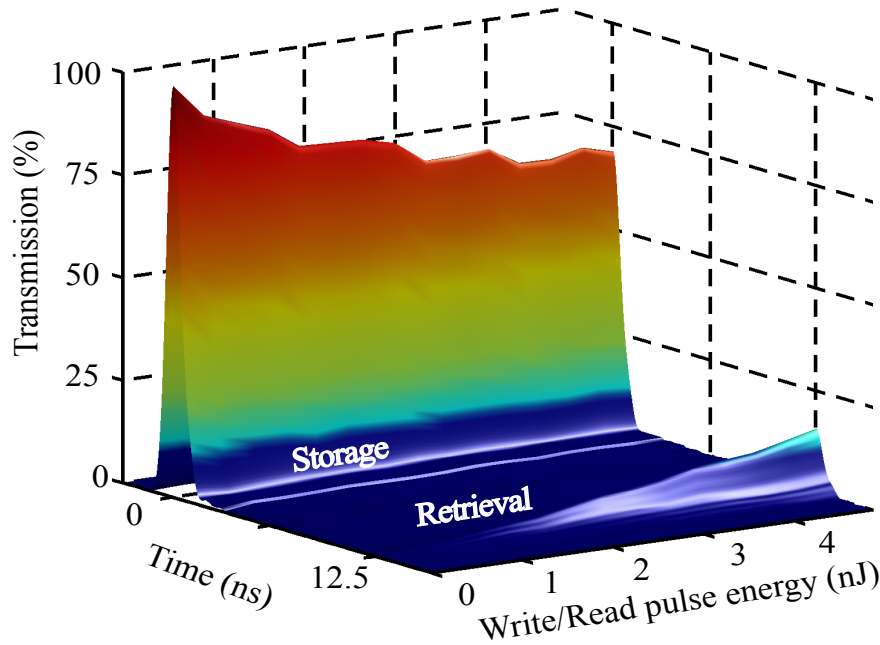


**Figure 4.13:** Optical storage and retrieval in detail. Storage ( $t = 0$  ns) and retrieval ( $t = 12.5$  ns) of light pulses vs write/read pulse energy. With no write pulse present (0 nJ), there is 100% transmission; with the highest write/read pulse energies (4.8 nJ) this drops to 70%, indicating that 30% of the incident signal is stored. At  $t = 12.5$  ns, 50% of the stored information is retrieved, giving a total memory efficiency of 15%.

contrast with resonant storage protocols, where the memory becomes absorbing when ‘inactive’; and as the pulse energies increase, the transmitted fraction of the incident signal decreases and the retrieved signal increases. The total retrieval efficiency was higher than 15% and comparable or better compared to most of the state-of-the-art experiments at the time<sup>[70,75,117–121]</sup>.

Figures 4.14 (a, b) show a comparison of the measured storage and retrieval efficiencies with the predictions of a theoretical model<sup>[80]</sup> introduced in Section 2.7. For modelling the experimental data according to Equations (2.24) and (2.25), Gaussian temporal profiles are assumed for all pulses. Therefore the input field

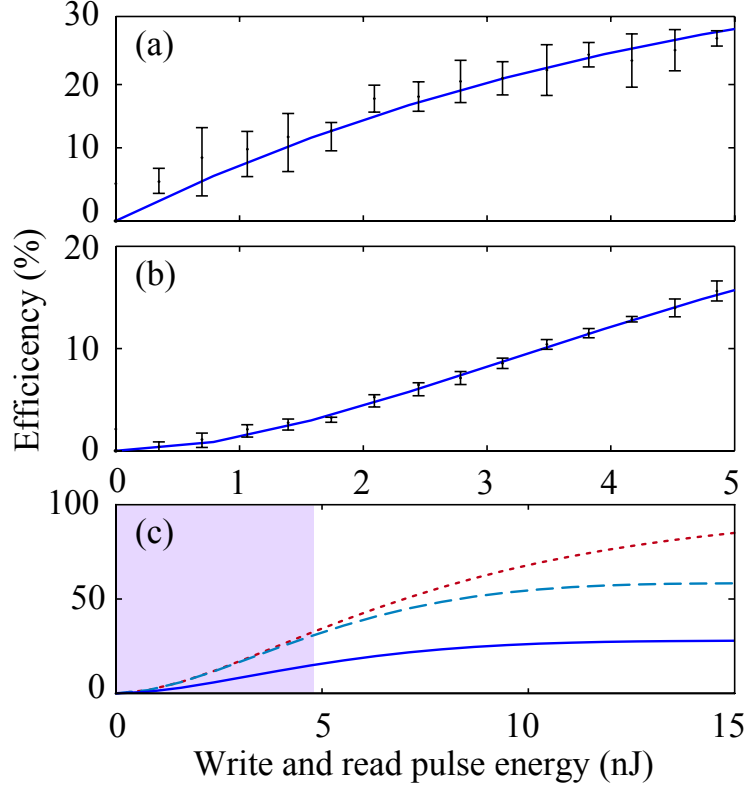


**Figure 4.14:** Memory efficiency dependence of control field pulse energy. **(a)** Storage efficiency. **(b)** Total efficiency. Dots and error bars represent experimental data; solid lines represent predicted theory. Error bars indicate the standard deviation derived from several datasets each averaged over 100 samples per point. **(c)** Theoretical predictions for total efficiency (see Equation 2.25) extrapolated to higher pulse energies, using the same experimental optical depth  $d$ . Solid line: efficiency for current experimental configuration (forward readout). Dashed line: optimal efficiency using forward retrieval, limited by re-absorption [79,93]. Dotted line: optimal efficiency using phasematched backward retrieval. The shaded area denotes the range of pulse energies accessible in the present experiment.

$A_{\text{in}}(\tau)$  can be expressed as

$$A_{\text{in}}(\tau) = \left(\frac{2}{\pi}\right)^{\frac{1}{4}} \frac{1}{\sqrt{T_s}} e^{-\left(\frac{\tau-t_s}{T_s}\right)^2}, \quad (4.1)$$

where  $T_s$  is the duration of the signal field and  $t_s$  is the delay of the signal

field with respect to the control field. The output field  $A_{\text{out}}(\tau)$  is computed using Equation (2.22). The timing and duration of the signal pulse are adjusted to account for the dispersive effects of the etalons used to spectrally filter the signal. Therefore the following parameters are used in the simulation:  $T_s = 2.5$ ,  $t_s = -1$ ,  $C = 2$ , and  $\Omega(\tau) = e^{-\tau^2}$  represents the envelope of the control pulse. In the present experiment the resonant optical depth  $d \sim 1800$  (see Section 2.8) is already large enough that near unit efficiency is attainable in principle. The theory presented above accounts for the finite energy of the available control pulses, the limitation due to which this optimal efficiency is not saturated. The experimental observations agree well with the theoretical model introduced in Section 2.7.

The retrieval efficiency  $\eta_{\text{ret}} = \eta_{\text{tot}}/\eta_{\text{store}}$  is significantly larger than the storage efficiency  $\eta_{\text{store}}$ , since the total efficiency  $\eta_{\text{tot}}$  exceeds  $\eta_{\text{store}}^2$ , indicating that the signal pulse shape is not optimal — an ideal memory has equal storage and retrieval efficiencies<sup>[79]</sup>.

Figure 4.14 (c) shows a theoretical extrapolation for the total memory efficiency  $\eta_{\text{tot}}$  to larger control pulse energies. In the present configuration, using forward retrieval,  $\eta_{\text{tot}} \sim 30\%$  is achievable for pulse energies  $\sim 15$  nJ. Also plotted is the optimal attainable efficiency for this case, along with the optimal efficiency for backward retrieval<sup>[79,93]</sup>. Achieving these bounds requires appropriate shaping of the signal field to compensate for distortion introduced by the etalons and for the dynamic Stark shift from the strong write field. This, however, may not be straightforward, because pulse shaping in the picosecond regime is an emerging technology and an active research area in itself<sup>[122–124]</sup>. Re-absorption of the signal limits the efficiency to around 60% for forward retrieval, but efficiencies above

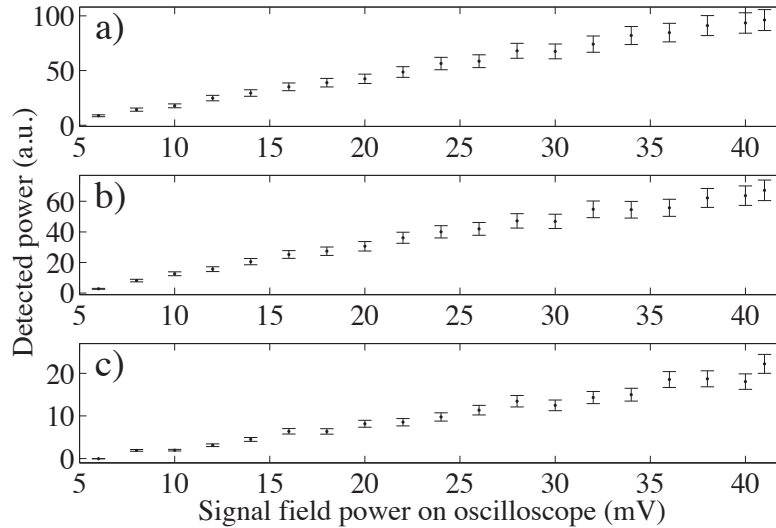


**Figure 4.15:** Detected power vs. signal field intensity. (a) Transmitted, un-stored signal field vs. signal field power. (b) Transmitted fraction of the original signal that did not get stored vs. signal field power. (c) Retrieved signal vs. original signal field power. Error bars indicate the standard deviation derived from several datasets each averaged over 100 samples per point. All three curves behave in the same linear way as expected from changing the signal field power.

90% can be reached using phase-matched backward retrieval<sup>[93]</sup>.

#### 4.5.2.3 Signal field power run

Next we investigated the dependence of the memory behaviour with respect to the signal field intensity, while the control field power, diode laser power and vapour cell temperature were kept constant. The storage and the retrieval efficiency of the memory were unaffected when the signal field strength was changed. This is because the memory efficiency  $\eta$  was independent of the signal field amplitude, as discussed in Section 2.7. Figure 4.15 verifies that behaviour. Figure 4.15 (a) represents the incident signal field transmitted through the vapour cell without any memory interaction because the control and the signal field were switched

off. Its transmission scaled linearly with signal field power, which was varied using a  $\lambda/2$  wave plate and a polariser. Figure 4.15 (b) shows the transmitted fraction of the original signal that did not get stored during the storage process and Figure 4.15 (c) illustrates the measured power of the retrieved signal as a function of the incident signal field power. As expected, they exhibited a linear behaviour and the ratio between the stored and the original transmitted signal is  $\mathcal{R}_{s/t} = 0.7 \pm 0.03$  and the ratio between the retrieved and the original transmitted signal is  $\mathcal{R}_{r/t} = 0.18 \pm 0.03$ . This suggests that all three curves change in the same fashion as a function of the signal field strength. Therefore the total memory efficiency  $\eta_{\text{tot}}$  does not depend on the incident signal field power.

### 4.5.3 Storage and retrieval of gigahertz bandwidth

One of the most important novelties about the far off-resonant Raman memory is its capability for storing and retrieving light pulses with extremely large bandwidth. High bandwidth allows the storage of temporally short photons, enabling quantum information to be processed at a higher clock rate and more quantum information to be sent during the same amount of time. This can be difficult to achieve with atomic memories, since photons must be stored in long-lived atomic states with narrow linewidths (see Chapter 2). Figure 4.16 demonstrates the storage and retrieval of signal pulses with a bandwidth 300 times larger than the natural width of the caesium  $D_2$  line ( $\sim 5$  MHz)<sup>[95]</sup>, that mediates the interaction. So far, quantum memories have operated with bandwidths ranging from kHz to MHz<sup>[38,70,77,125]</sup>. Compared to these memories, the new far off-resonant Raman approach represents an increase of more than 100, extending the usable bandwidth into the GHz regime. Note that very recently a second quantum memory

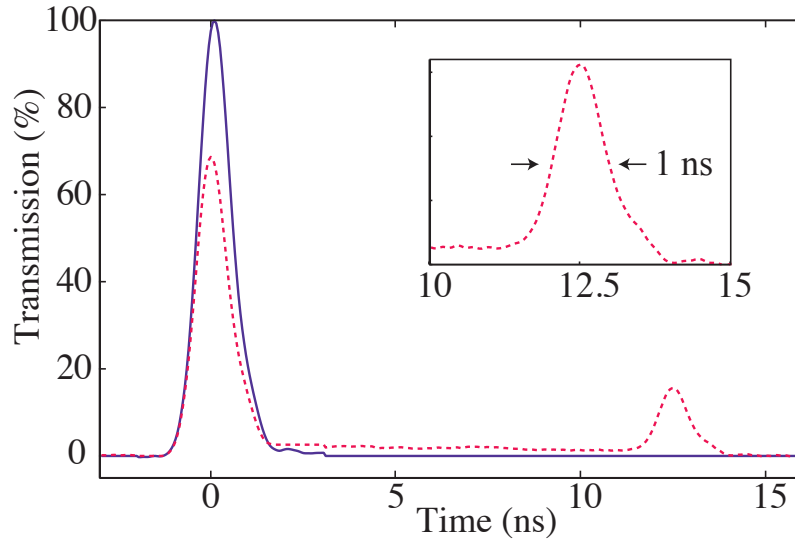


**Figure 4.16:** Storage and retrieval of pulses with GHz bandwidth. Storage ( $t = 0$  ns) and retrieval ( $t = 12.5$  ns) of GHz bandwidth light pulses. Solid line: Signal field without memory interaction. Dashed line: Signal field with memory interaction. Inset: Zoom of retrieved signal field showing the measured full width at half maximum (FWHM) temporal duration of 1 ns, limited by the detector response time. This shows that the bandwidth of the retrieved signal exceeds 1 GHz.

reached the gigahertz regime<sup>[126]</sup>.

Figure 4.16 shows the storage and the retrieval event in detail. At  $t = 0$  a signal pulse got mapped into an atomic spin wave excitation in the caesium ensemble and 12.5 ns later the stored excitation was recovered and the retrieved signal emerged from the ensemble. The inset in Figure 4.16 shows the short pulse duration of the retrieved signal. The measurement was limited by the 1 ns response time of the detector (see Section 3.9.4), corresponding to a bandwidth of 1 GHz. Theoretically, the Raman memory is also capable of larger bandwidths. The fundamental limit regarding storable bandwidth in a Raman memory is set by the interaction medium, specifically the splitting of the ground state  $|1\rangle$  and storage state  $|3\rangle$ , as discussed in Section 2.9.1. If the bandwidth were too large

(i.e. approximately larger than half the size of the splitting), the signal or the read/write field, when tuned to either the ground state or the storage state, would also address the other state, thus leading to a competing ‘double- $\Lambda$ ’ system. Depending on the overlap, this would substantially reduce or completely disrupt the memory fidelity and efficiency. In the caesium case, the ground-/storage-state splitting is the hyperfine splitting between the  $6^2S_{1/2}$  F=3 and F=4 manifold, which is 9.2 GHz. Therefore the maximum storable bandwidth is roughly 4 GHz.

Practically, however, there is a delicate balance between the storage bandwidth and the available control field power, detuning and optical depth. Since the detuning should be much larger than the bandwidth to maintain adiabatic evolution (see Section 2.6), larger bandwidths require larger detunings, but this would reduce the interaction strength, therefore requiring larger control field power and greater optical depth. On the other hand, optical pumping at large optical depths can become problematic (see Section 3.10.2). In general, determining the feasibility of Raman storage requires careful assessment of the various material and optical parameters.

The time-bandwidth product  $N$  of a memory quantifies the number of distinct time bins available for computational operations in a hypothetical quantum processor using the memory. Assuming that the storage time of the memory is limited to several hundred  $\mu\text{s}$  — typical for warm alkali vapours<sup>[106]</sup> — time-bandwidth products as high as  $N \sim 10^5$  should be achievable<sup>[44]</sup>. Furthermore, the time-bandwidth product is an important benchmark for broadband quantum information networks, as a larger value indicates that more information can be sent during the same amount of time. This is an essential requirement for creating high-speed transmission links between different nodes of the quantum network.

Another useful figure of merit is the multimode capacity: the number of modes that can be stored simultaneously (in a single storage/retrieval cycle)<sup>[39,40]</sup>. Multimode memories have applications in multiplexed quantum repeater protocols<sup>[40]</sup>. Although the Raman memory is essentially a single-mode memory in the current collinear configuration<sup>[39]</sup>, multiple modes can be stored by using either angular multiplexing<sup>[93]</sup> or multiple memories<sup>[127]</sup>, as we will see in Chapter 6.

#### 4.5.4 Verification of the memory coherence

So far the ability to controllably absorb and retrieve light pulses was demonstrated. The question of whether or not the stored and the retrieved field were the same is still unanswered. In order to address this issue and find out whether the memory preserved coherence, a Mach-Zender type interferometer, as illustrated in Figure 4.17, was set up. The signal field was split into two beams by a 50/50 beam splitter. One beam was sent into the memory experiment, comprising the first arm of the interferometer, and set to a storage time of 12.5 ns, the other beam travelled along the 3.75 m longer second arm of the interferometer that produced an optical delay of 12.5 ns. The length of this optical delay line was already difficult to accommodate on the optical bench — going to e.g.  $\sim 1 \mu\text{s}$  would not be possible this way. Note that single mode fibres could be used for implementing longer delay lines. The retrieved signal and the attenuated, delayed signal were recombined at a second 50/50 beam splitter. From there onward they overlapped temporally, passed a polariser to ensure that they had the same polarisation and coupled into a single mode fibre (SMF) that was connected to a fast APD. The SMF guaranteed that both the retrieved and the delayed signal had exactly the same spatial mode, a key requirement in addition to equal signal

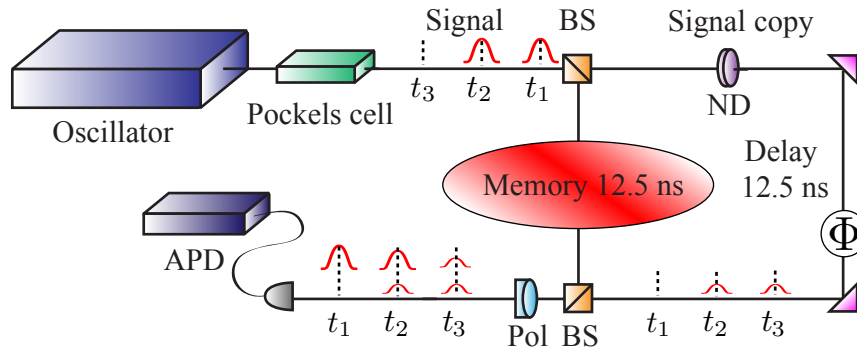


**Figure 4.17:** Memory coherence test interferometer setup. Mach-Zender type interferometer setup for testing the memory coherence. The signal field consists of two pulses in time slots  $t_1$  &  $t_2$  and is divided into two identical copies. The memory setup represents one interferometer arm (producing a retrieved signal at time  $t_3$ ); the other is an optical delay line, shifting one copy of the signal by 12.5 ns to time bins  $t_2$  &  $t_3$ . A neutral density filter (ND) attenuates the copied signal and matches it to the retrieved signal produced by the memory. A phase shifter (piezoelectric mirror), adjusts the phase  $\Phi$  of the optical delay path with respect to the memory path. The fibre-coupled APD detects the interference signal caused by the two light fields.

intensities and polarisations of the two individual signals for observing high interference visibility. It was verified that the time difference between the delayed and the retrieved signal pulse was  $\Delta\tau = 0$  and that their intensities were equal.

The interferometer was neither intrinsically stable on time scales of several minutes and above, as can be seen in Figure 4.18 (a), nor was it actively stabilised using feedback control<sup>[128,129]</sup>. The large free space beam paths in both interferometer arms were affected by temperature fluctuations and air currents that changed the beam pointing of both laser beams and maybe even affected the individual phase of the laser beams due to a change of refractive index  $n$  along the beam paths. Figure 4.18 (a) shows the integrated traces of the different time slots  $t_1$ (blue),  $t_2$ (red) and  $t_3$ (black) for the bare interferometer. At  $t_1$  there was just a single transmitted signal pulse and therefore no interference. The

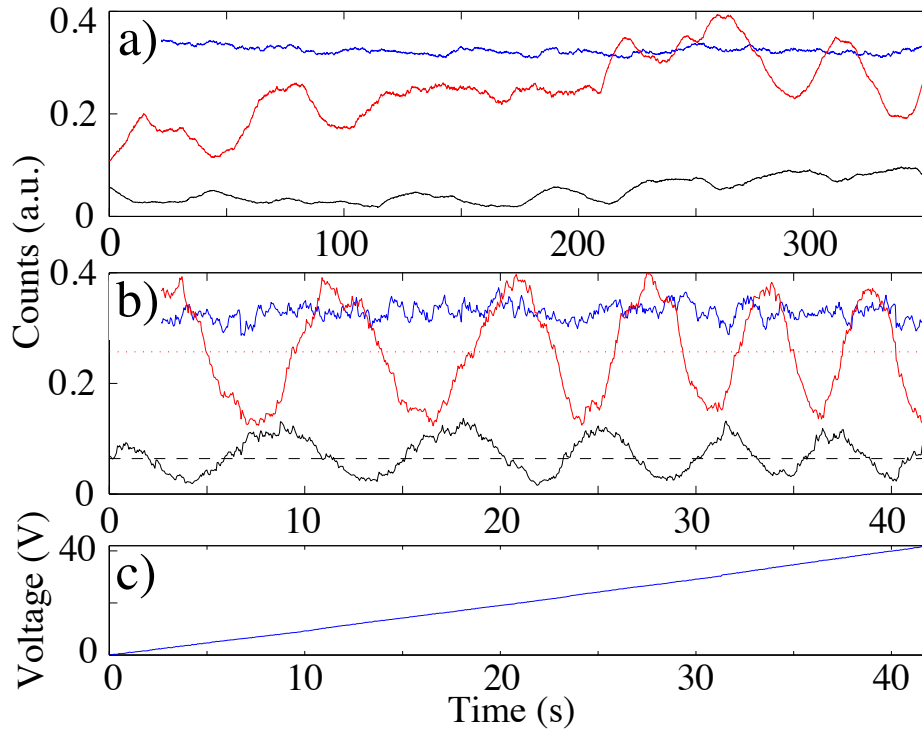


**Figure 4.18:** Mach-Zender type interferometer characterisation. **(a)** No active path length control. Blue curve ( $t_1$ ): Hardly any fluctuations because there is only a single pulse and therefore no interference is possible. Red curve ( $t_2$ ) and black curve ( $t_3$ ): Random interference on long time scales  $\sim 100$  s due to fluctuations in the large interferometer arms. **(b)** Active path length control via piezo electric mirror. Blue curve: Relatively constant (single pulse only). Red curve and black curve: Strong periodic oscillations due to controlled path length change in second interferometer arm. **(c)** High voltage ramp of piezo electric stack.

measured signal stayed roughly constant over time. However, there was a small oscillator drift in frequency over time with respect to the transmission window of the etalons that resulted in an imperfect match with the laser frequency and therefore a reduction of the transmitted signal.

At  $t_2$ , the transmitted portion of the stored signal interfered with the first pulse of the delayed signal and at  $t_3$  the retrieved signal interfered with the second pulse of the delayed signal. Both traces show an interference effect; there

are weak signals that indicate destructive interference and strong signals that indicate constructive interference. However, these effects are totally random and there are no correlations between the red and the black curve. One feature that can be identified from the red curve is that the interferometer has stable periods that can last up to 100 s. If information were to be extracted from this interferometer, the phase of one of the interferometer arms would have to be changed faster than the timescale, at which the random fluctuations occur.

This is exactly what was done in Figure 4.18 (b). One of the mirrors in the long interferometer arm was replaced by a mirror that was mounted on a piezo electric stack, such that the path length difference  $\Delta l \sim \mu\text{m}$  could be changed actively. The required high voltage for the piezo stack was about 40 V in order to create a path length difference of  $\Delta l \sim 5 \mu\text{m}$ . The ramping speed was set to  $1 \text{ Vs}^{-1}$  as can be seen in Figure 4.18 (c).

Taking a closer look at Figure 4.18 (b) reveals that there are hardly any fluctuations for the blue curve because there was only one signal and therefore nothing to interfere with. However, the interesting physics is displayed by the red curve and the black curve, where large oscillations are visible. The oscillations are periodic and repeat themselves about every 8 s. On these short time scales the random interferometer drift discussed above was irrelevant and therefore the oscillations are purely of interferometric origin due to the active path length change caused by the expansion and contraction of the piezo stack. The dotted red line represents the sum of the two individual signal peaks at time bin  $t_2$  and the dashed black line is the sum of the two individual peaks at time bin  $t_3$ . The constructive interference for both the red curve and the black curve exceeds the peaks by more than a factor of 2. The reason why the red curve does not go to

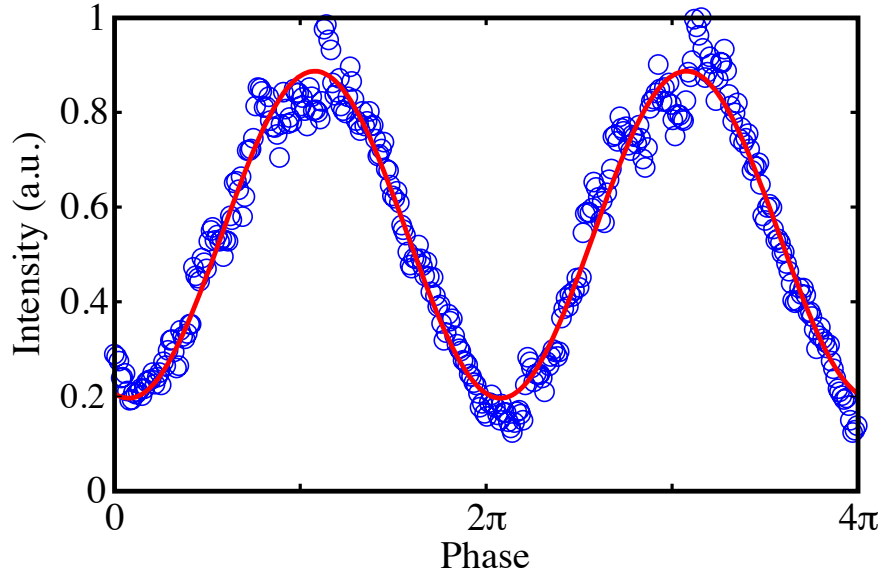


**Figure 4.19:** Memory coherence data. Raw interference of stored and retrieved signal. Circles indicate experimental data, the solid curve is a least squares fit. A linear scan of the path length difference in the interferometer results in sinusoidal oscillations of the total intensity. This shows a high visibility of  $82.7 \pm 0.9\%$  (normalised for interferometer instability).

zero is because here two signals of different amplitude interfered; the transmitted part of the stored signal and the attenuated copy of the original signal.

The crucial part representing the memory coherence can be extracted from the black curve and is illustrated in a better format in Figure 4.19. Plotted are the raw interference data versus the phase  $\Phi$  accumulated in the second interferometer arm by changing the position of the piezo electric mirror (PEM). A scan of the PEM caused the interference of the two optical fields to turn from destructive ( $\Phi = 0$ ) to constructive ( $\Phi = \pi$ ) with a periodicity of  $2\pi$ . The fringe visibility was  $82.7 \pm 0.9\%$  (normalised for interferometer instability). This indicates that the memory was highly coherent and preserved the phase information of the stored signal.

In this coherence test, while measuring the interference between the input and retrieved signals, we simultaneously measured the interference between the input signal and a weaker replica of the signal as a benchmark, obtaining an interferometer visibility of  $V_b = 77.2 \pm 0.5\%$ . Representing the effects of imperfect mode matching and phase fluctuations in both the interferometer and the laser pulse train, this provided a direct measure of the intrinsic interferometer visibility for the duration of the coherence test, and thus a maximum achievable value for the measured memory visibility. In our experiment, we obtained a raw memory visibility (for the interference between the input and retrieved signals) of  $V_{\text{raw}} = 63.8 \pm 0.6\%$  from the data in Figure 4.19. Normalising this value by the measured intrinsic interferometer visibility gave a corrected visibility of  $V_{\text{corr}} = V_{\text{raw}}/V_b \approx 82.7 \pm 0.9\%$ . This value could be interpreted as the actual visibility of the Raman memory interaction.

We compare these experimental observations with a theoretical model for predicting the visibility that takes into account the expected distortion of the signal field due to pulse stretching as it passes through the etalons, dispersion in the memory and the A.C. stark shift due to the strong control field. The model is based on the assumptions made in Section 4.5.2.2 and in Equation (4.1). The predicted visibility  $V_{\text{pred}}$  is computed as

$$V_{\text{pred}}(t) = \int_{-\infty}^{\infty} A_{\text{out}}^*(\tau - t) A_{\text{in}}(\tau) d\tau, \quad (4.2)$$

where  $t$  is a variable delay of the output field  $A_{\text{out}}$  that can be chosen to optimise the visibility. Using the parameters mentioned in Section 4.5.2.2, the maximum predicted visibility is computed to be 83%. This compares well with the experiment and therefore suggests that no other dephasing mechanisms are present

during the storage time. Due to this good match of experiment and theory we believe that the Raman memory operates close to perfect coherence<sup>[33]</sup>.

Because the stored signal was retrieved after just 12.5 ns, the observed efficiency was not affected by decoherence, which was only significant over much longer timescales. Instead, it was a direct probe of the intrinsic efficiency of the Raman memory interaction.

## 4.6 Improving the memory

The last sections demonstrated the functionality of Raman-based quantum memory but the initially achieved storage time and memory efficiency were not very high, so that solutions to improving this situation were sought.

### 4.6.1 Increasing the memory efficiency

As discussed in Section 2.7, the efficiency  $\eta$  of the quantum memory mainly depends on the optical depth  $d$ , the control field power and the detuning  $\Delta$ . Increasing the optical depth  $d$  is easy and can be done by simply heating the vapour cell; the problem with this approach however is optical pumping (see Section 3.10). The higher the density of the vapour, the less efficient the optical pumping and the worse the preparation of the  $\Lambda$ -level system.

In order to increase the memory efficiency, the detuning  $\Delta$  of the oscillator was reduced by 3 GHz to 15 GHz to the blue of the blue resonance and the control field power was enhanced by replacing all silver mirrors<sup>1</sup> used in the experiment with custom-made high reflectivity dielectric mirrors<sup>2</sup>, boosting the pulse energy of the

---

<sup>1</sup>Thorlabs silver mirrors (PF10-03-P01) with a reflectivity of 97% at 852 nm.

<sup>2</sup>Dielectric mirrors from Laseroptik with a reflectivity of 99.9% at 852 nm.

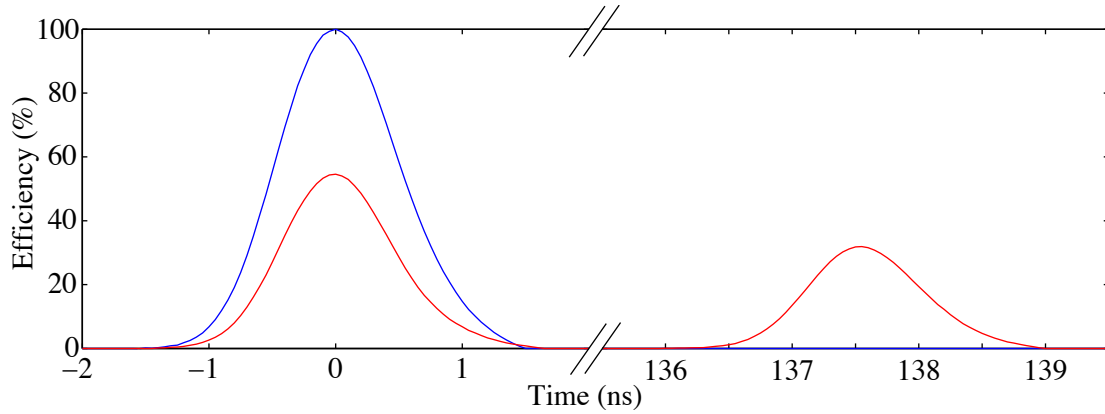


**Figure 4.20:** Increased memory efficiency. Blue curve: Incident signal without control field. Nothing is stored or retrieved. Red curve: Transmitted signal with control field. At  $t = 0$  ns the incident signal gets stored and at  $t = 137.5$  ns the stored signal gets retrieved. The total efficiency of the memory is  $> 30\%$  with a control field energy of 10 nJ.

control field from 5 nJ to 10 nJ. Furthermore the old Pockels cell system (PCS1) was replaced by a new Pockels cell system (PCS2), as described in Section 3.8, allowing for pulse picking at arbitrary delays. The 12.5 ns delay line in the control field arm was removed and a fast optical switch (see Section 3.5.2) was used to turn off the RF power for the EOM, such that no signal pulse was generated at the readout event. Magnetic shielding was placed around the vapour cell; the reasons for this will become clear in Section 4.6.2. The rest of the experimental setup stayed unchanged compared to the one described in Section 4.4. The results obtained regarding boosted memory efficiency can be seen in Figure 4.20. Here, the transmission of a signal pulse without a control field (blue curve) and its storage and retrieval in the presence of a control field (red curve) were measured. The storage time was set to 137.5 ns and the total efficiency of the memory  $\eta$  exceeded 30% with the smaller detuning  $\Delta$  and the higher control field pulse energy. The efficiency was still limited by experimental parameters like control

field power and readout geometry, as discussed in Section 2.7.

In order to increase the control pulse energy in subsequent experiments, the application of an amplifier system is considered and the implementation of a backward geometry for the retrieval of memory excitation<sup>[93]</sup> is planned.

### 4.6.2 Storage time enhancement & dephasing

As mentioned before in Section 4.6.1, the Pockels cell system PCS2 allows for selecting an arbitrary, completely controllable retrieval time, only limited by the repetition rate of the Pockels cell system. This means, that if the Pockels cell were operated at 10 kHz, the maximal retrieval time would be 100  $\mu$ s. In this section the physical limits of the storage time that are imposed by different spin wave dephasing mechanisms like influence of laser fields, magnetic dephasing and atomic diffusion are investigated.

#### 4.6.2.1 First memory decay measurements

During the first experiments (see Section 4.5.1), where the storage time was set to 12.5 ns, none of the aforementioned dephasing mechanisms played an important role. This is because on that timescale the atoms were basically frozen to a single location such that atomic diffusion was negligible and also coherence loss due to resonant atomic excitation by the permanently-on diode laser or dephasing of the atomic spins relative to each other by external magnetic stray fields was very unlikely<sup>[33,106]</sup>.

Subsequent measurements were carried out using the following experimental parameters: The laser oscillator was tuned 15.2 GHz to the blue of blue resonance and the red sideband was chosen as the signal field. The control field pulse

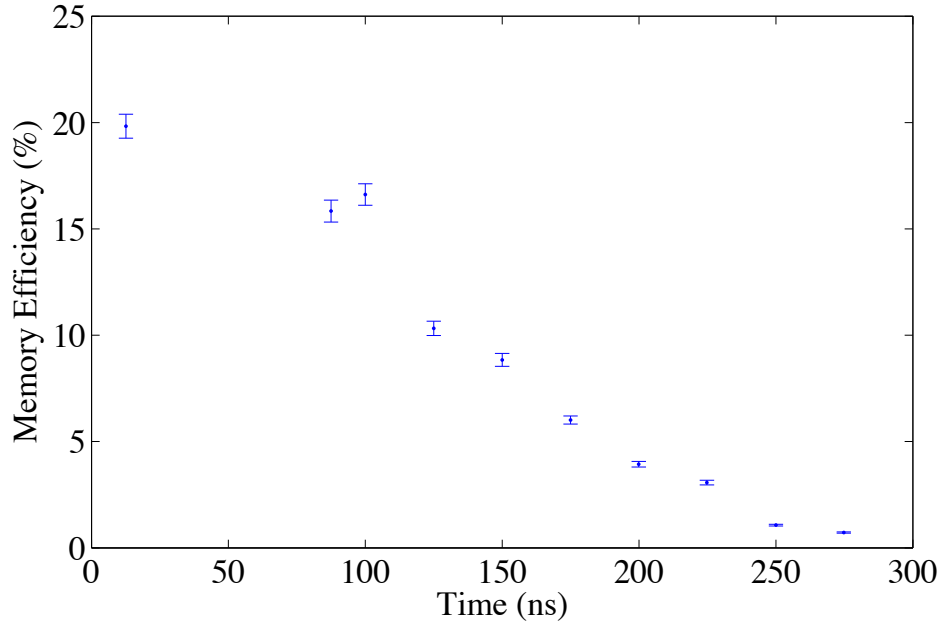


**Figure 4.21:** Memory lifetime without magnetic shielding. Dots represent experimental data and error bars indicate the standard error of the mean. The memory lifetime is  $\sim 150$  ns.

energy was 10 nJ and the vapour cell was heated to  $62.5^\circ\text{C}$  with no magnetic shielding in place. The control field and the signal field beam diameters were  $\varnothing \sim 350 \mu\text{m}$  inside the vapour cell. The experiment was operated with a repetition rate of 3.07 kHz. The oscilloscope was programmed to average over 30 different experimental runs, where a single run consisted of the measurement of the transmitted signal field through the vapour cell. The diode laser was tuned to the blue resonance and was permanently turned on with a cw laser power of  $80 \mu\text{W}$  and a beam waist of  $\varnothing \sim 1 \text{ mm}$ . Varying the storage time of the memory by adjusting the picked pulses of the Pockels cell lead to the results presented in Figure 4.21. At 12.5 ns, the setting for the initial experiments (see Section 4.5.1), the highest retrieval efficiency was observed. As the storage time was increased, the memory efficiency dropped off quickly and reached a  $1/e$  value

at about 150 ns, the lifetime of this magnetically unshielded, permanently diode-laser-pumped memory incarnation. On these timescales atomic diffusion was not an issue. However, magnetic dephasing and diode laser pumping were a problem. It is hard to draw precise conclusions from the obtained data, because it was affected by contributions from various dephasing mechanisms. In order to achieve longer storage times in consecutive experiments, successively eliminating possible dephasing mechanisms was the way to proceed.

#### 4.6.2.2 Extension of memory lifetime by magnetic shielding

Further investigation of the different dephasing mechanisms required the use of magnetic shielding, which was placed around the memory cell. In addition, the old Pockels cell system (PCS1), which originally was used for pulse picking, was installed in the diode laser beam path to turn off the diode laser for up to 900 ns, the maximum switching time of this device (see Section 3.8). Magnetic shielding<sup>1</sup> reduced magnetic field gradients and magnetic stray fields caused by nature and the laboratory equipment, and created a *zero Gauss environment*<sup>2</sup>. As many electronic devices were used, e.g. Pockels cells operating with high voltages, there was a lot of magnetic noise that affected the spin coherence of the memory. The homemade magnetic shielding system consisted of three layers of  $\mu$ -metal<sup>3</sup> with a thickness of 0.12 mm each. They were wrapped cylindrically around the vapour cell with a diameter of  $\varnothing \sim 3$  cm. The shield extended past the vapour cell on both ends by about 5 cm and had a total length of 18 cm.

---

<sup>1</sup>Magnetic shielding was purchased from Magnetic Shields, UK.

<sup>2</sup>In a zero Gauss environment there are no magnetic fields present.

<sup>3</sup> $\mu$ -metal is a nickel-iron alloy (approximately 75% nickel, 15% iron, plus copper and molybdenum) that has a very high magnetic permeability. The high permeability makes  $\mu$ -metal very effective at screening magnetic fields.

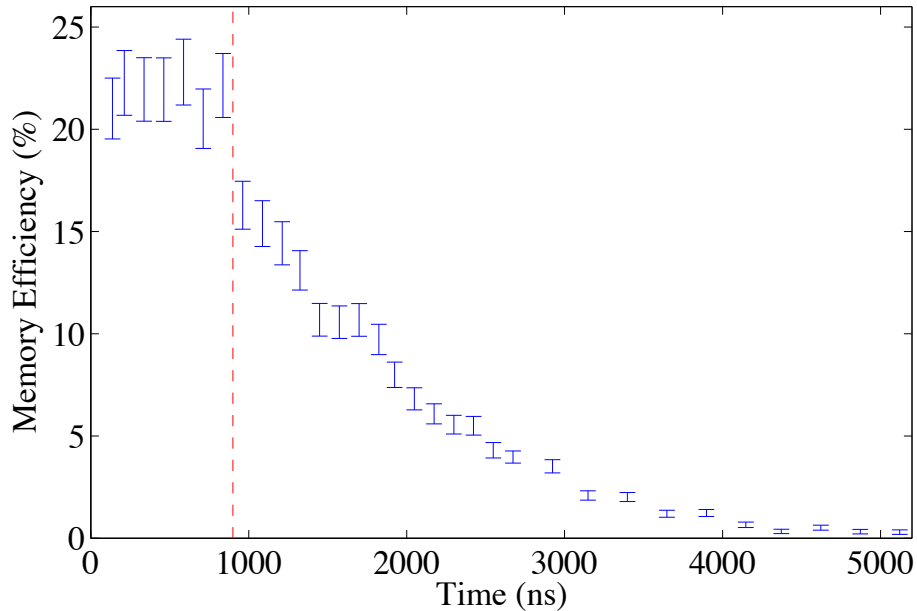


**Figure 4.22:** Memory lifetime with magnetic shielding and diode laser off for 900 ns. Red dashed line indicates when diode laser switches back on. Dots represent experimental data and error bars indicate the standard error of the mean. The lifetime of this memory is  $\sim 1800$  ns.

The effect of magnetic shielding on the memory lifetime can be seen in Figure 4.22. The diode laser was turned off initially during the storage process and switched back on at  $t = 900$  ns (dashed red line). The magnetic shielding had a very positive effect on the memory lifetime. In the presented case the lifetime was  $\sim 1800$  ns. This is already an improvement of more than 10 compared to the magnetically unshielded case displayed in Figure 4.21. In the shielded experiment, the memory efficiency did not fall off quickly at the beginning when the diode laser was turned off ( $t < 900$  ns). But after the diode laser turned on at  $t > 900$  ns, there was a drastic reduction in memory efficiency, possibly caused by the diode laser starting to pump out the memory spin wave coherence that was established between the ground state and the storage state. Furthermore, due

to the non-ideal design of the magnetic shielding chamber, magnetic dephasing played an important role as well. Magnetic shielding could be improved by using thicker  $\mu$ -metal and placing lids at the end of the shielding cylinder that only have small entry and exit ports for the light fields.

In order to isolate specific dephasing mechanisms, it would be nice to be able to turn off the diode laser completely, for example by using an AOM (see Section 3.3.2.2). This equipment was not available during the first experiments, but was added subsequently. Results obtained with this technology are described in Section 4.6.2.4.

#### 4.6.2.3 Dephasing caused by the diode laser

The effect of the diode laser in emptying out the storage state via optical pumping was investigated further. The same set up as in Section 4.6.2.2 was used. For these measurements however, the memory storage time was fixed to 900 ns and the duration for which the diode laser was switched off during the storage period was changed. The result can be seen in Figure 4.23. The left-most data point at  $t = 900$  ns corresponds to the diode laser being switched off for 900 ns, i.e. for the whole storage time. The right-most data point at  $t = 50$  ns shows the memory efficiency for the case when the diode laser was turned off for the first 50 ns and turned on for the remaining 850 ns of the storage time. It is hard to draw precise conclusions from the data regarding the population of the storage state and the ground state. However, it is clear from this data set that the diode laser had a negative effect on the efficiency of the memory when it was left on during the storage period. Basically, the memory efficiency was halved from the case where the diode laser was turned on for 850 ns out of the 900 ns storage time compared

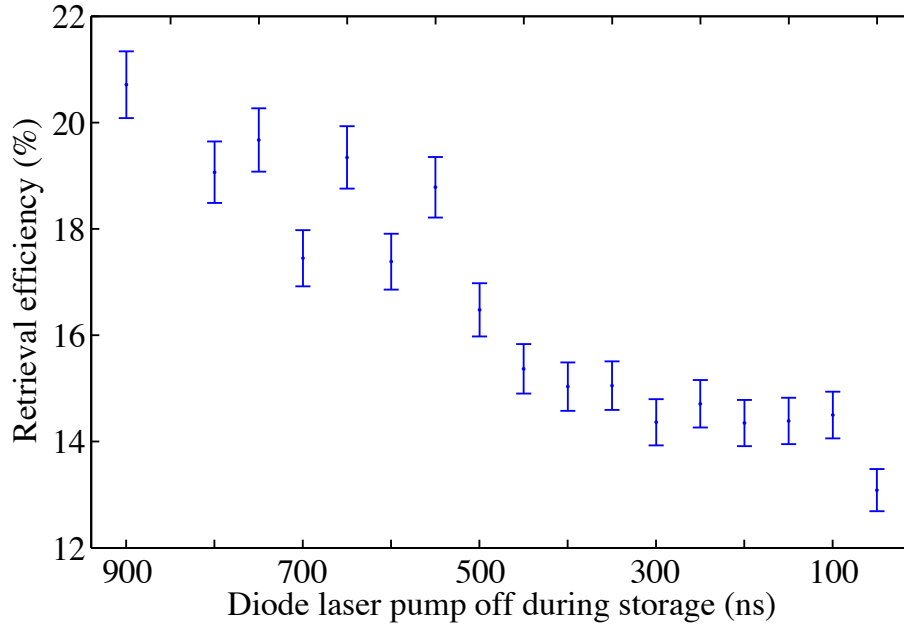


**Figure 4.23:** Effect of diode laser on memory efficiency. The storage time is fixed to 900 ns and the diode laser turn-off time during the storage period is varied from 900 ns (completely off during storage) to 50 ns (almost completely on during the storage), where the memory efficiency drops by half compared to the “off-case”.

to the case where the diode laser was completely switched off. This suggests that using an AOM for turning off the diode laser completely during the storage period is essential for achieving longer memory lifetimes.

#### 4.6.2.4 Memory with magnetic shielding and diode laser off

Installing and using an AOM in the diode laser beam path finally allowed us to turn off the diode laser completely, even for longer storage times. Furthermore, the control field pulse energy could be increased to 12 nJ and the beam overlaps were optimised to reach the current technological limits regarding memory efficiency and memory lifetime. The results can be seen in Figure 4.24. The memory efficiency exceeded 30% for short storage times and the memory lifetime

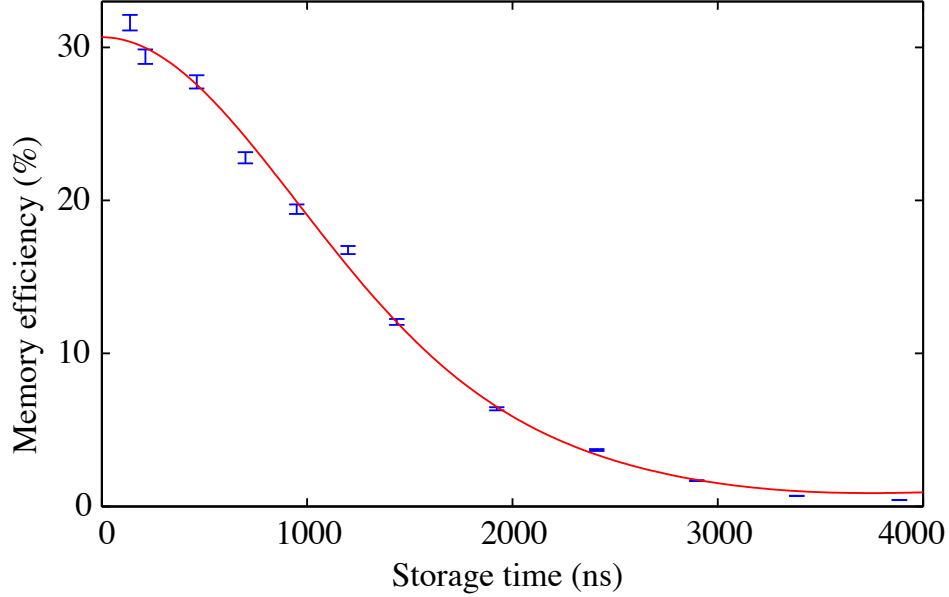


**Figure 4.24:** Memory lifetime with magnetic shielding and diode laser permanently off. The lifetime of the memory is about  $1.5 \mu\text{s}$ . The blue dots indicate experimental data measured with a fast APD. Error bars represent the standard error in the mean. The solid line is the theoretical dephasing predicted for a constant magnetic field of  $0.13 \pm 0.05$  Gauss, which can be attributed to the residual of the Earth’s magnetic field. Note that this dephasing could be compensated using spin-echo techniques, or suppressed with improved magnetic shielding.

was  $\sim 1.5 \mu\text{s}$ . These results were obtained with similar magnetic shielding compared to the one used in Section 4.6.2.2 and residual static fields were the main dephasing mechanism as discussed in Section 2.10.1.

The fit in Figure 4.24 is produced by plotting  $\eta(t)$  (2.30), multiplied by an appropriate scaling factor, assuming a uniform initial thermal distribution  $p_{m_i} = 1/(2F_i + 1)$ , where the magnetic field  $B \approx 0.13$  Gauss and orientation ( $\theta = 30^\circ$  from the vertical, i.e. from the direction of the control field polarisation, and  $\phi = 25^\circ$  from the direction of propagation of the optical beams) are determined from a least-squares fit to the experimental data.

In principle, magnetic dephasing can be eliminated by improved magnetic

shielding (see Section 4.6.2.2), enabling storage times limited by atomic diffusion to several hundred  $\mu\text{s}$ <sup>[106]</sup>. However, because this memory has such a broad bandwidth, the measured lifetime already corresponds to a time-bandwidth product of  $\sim 2500$  (see Section 4.5.3). With a memory efficiency of 20% at a storage time of 1  $\mu\text{s}$ , this memory could already be used to improve heralded photon-pair rates as compared to typical parametric down-conversion sources, which have heralded single photon rates of  $\sim 1$  MHz<sup>[130]</sup>. As discussed in Ref.<sup>[33]</sup>, the memory efficiency is restricted mainly by control field power and the less efficient, but experimentally simpler, forward-retrieval configuration<sup>[80]</sup>.

#### 4.6.2.5 Magnetic rephasing

In an ideal isolated system, where only a homogeneous magnetic field is present and the atoms are frozen in space, magnetic dephasing of a stored spinwave excitation is a pure periodic process because the electronic energy level structure is discrete due to the Zeeman effect. The time between rephasings is  $T_{\text{rephase}} \sim 1/|\mathbf{B}|$ , where  $\mathbf{B}$  is the magnetic field. The stronger the magnetic field, the quicker the rephasings. However, in a real physical system there are other processes that cause decoherence and reduce the spinwave coherence like atomic collisions, diffusion of the atoms out of the optical beam path and inhomogeneous magnetic stray fields that do not lead to a periodic rephasing. Suppose that the timescale for these processes is  $T_{\text{irrev}}$ . The earth's magnetic field  $B_{\text{earth}}$  is weak and therefore  $T_{\text{rephase}} \gg T_{\text{irrev}}$ , which means that it will not be possible to observe natural rephasings mediated by the earth's magnetic field in a real system. If an external homogeneous magnetic field is added, then the total magnetic field  $\mathbf{B}_{\text{tot}} = \mathbf{B}_{\text{earth}} + \mathbf{B}_{\text{added}}$  can be increased and the rephasing time can be reduced

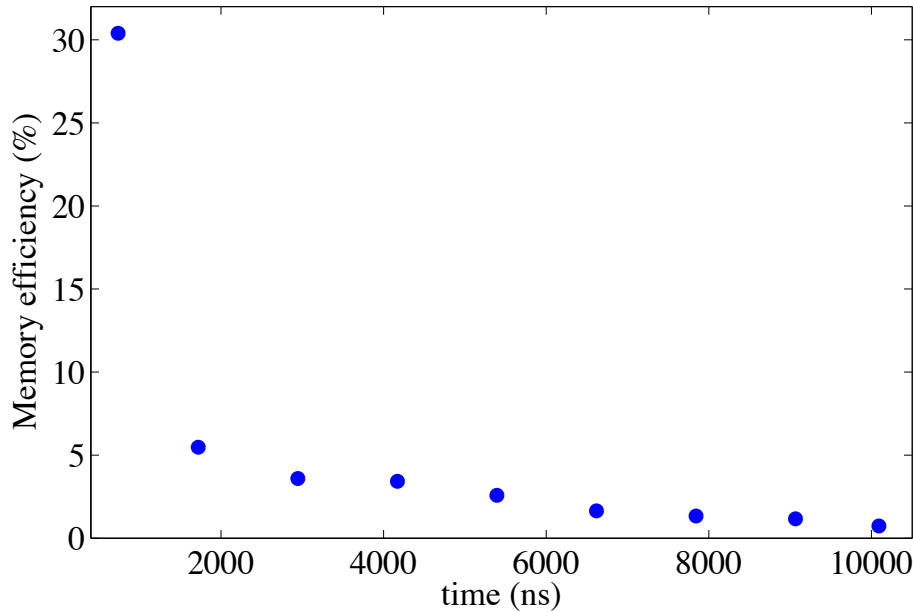


**Figure 4.25:** Magnetic rephasing. The application of an external magnetic field enables the extension of the storage time up to  $10 \mu\text{s}$ . The experimental errors for the memory efficiency  $\eta$  are  $\sim 0.05\%$  and are therefore smaller than the blue points that represent the experimental data which was measured with a fast APD.

such that  $T_{\text{rephase}} < T_{\text{irrev}}$ . In this case magnetic rephasing will be observable.

I was curious to see whether it is possible to observe magnetic rephasing in our experiment and therefore constructed a magnet with the following specifications. The magnet had a toroidal structure with  $N = 1000$  windings, a length of  $L = 10$  cm and an inner diameter of  $\varnothing = 7$  cm, providing enough space to accommodate the vapour cell including the heating system. The current applied to the magnet ranged from 0.2 A to 1.7 A. With the magnetic field,  $B = \mu_0 \times \frac{NI}{L}$ , where  $B$  is the magnetic field,  $N$  is the number of windings,  $I$  is the current and  $L$  is the length of the toroid, that corresponded to a magnetic field of 25 - 200 Gauss.

The vapour cell was placed inside the magnet and the external magnetic field was tuned. For a fixed storage time different retrieved signals could be obtained

for different magnetic field settings. For each of the specific storage times the retrieved signal field was optimised. The obtained data is displayed in Figure 4.25. In these experimental conditions, signals could be retrieved from the memory for up to 10  $\mu\text{s}$  after the original storage process. Compare this to the maximum storage time of  $\sim 4 \mu\text{s}$  in Figure 4.24.

An externally applied magnetic field causes a Zeeman shift of the atomic energy levels and due to the polarisation selection rules certain transitions are allowed only (see Section 6.3.5). If for example the entire ensemble were prepared in a single magnetic sub-level, e.g.  $m_F = 0$  of the  $6S_{1/2}, F = 4$  ground state, and only a circularly polarised signal field and control field were incident, only one single magnetic sub-level (e.g.  $m_F = 2$ ) in the  $6S_{1/2}, F = 3$  storage state were to participate in the spin wave excitation. Thereby the aforementioned reversible magnetic rephasing could be eliminated, but the irreversible magnetic dephasing due to random magnetic field fluctuations would still be a problem.

This set of data is very preliminary and before any solid conclusions can be drawn from these observations, much more detailed experiments need to be carried out. However, I think this is an interesting phenomenon that could possibly be useful for future experiments regarding the extension of the memory's storage time, which is why I decided to include these results here.

## 4.7 Multiple readout

With the Pockels cell system PCS2 there is not only the possibility to control the timing of the stored and retrieved pulses, but also to vary the width of the Pockels cell switching windows (see Section 3.8). Therefore the number of readout

pulses is selectable, and the PCS2 can be set to retrieve multiple signals from the same spin wave excitation. However, this works only if the first read pulse did not extract the complete coherence from the atomic ensemble. Furthermore, the strength of the read pulses can be attenuated by overlapping the Pockels cell's rising/falling edge with one of the pulses from the pulse train.

#### 4.7.1 Complete readout – ‘Crazy train’

The experimental setup for carrying out this idea was the same as the one described in Section 4.6.1. The control pulse energy was 10 nJ, the Pockels cell repetition rate was set to 3.09 kHz and the diode laser pump power was 150  $\mu\text{W}$ . The diode laser was turned off completely during the storage period and the beam waists for both the control field and the signal field were  $\varnothing \sim 350 \mu\text{m}$  along the 7 cm vapour cell that was heated to 62.5°C. The diode laser was tuned to the blue resonance and the control field was tuned 15 GHz to the blue of the blue resonance. The red sideband was selected to form the two-photon resonance. Two layers of magnetic shielding with a thickness of 0.15 mm each and a length of 38 cm were in place around the vapour cell and the heating system. A beam pick-off using a small glass plate was inserted in the control field path to monitor the number of picked pulses on a fast photo diode.

Figure 4.26 (a) shows the storage event that took place at  $t = 0$  ns. About 40% of the incident signal (black curve) got stored and 60% of the incident signal got transmitted (dashed red curve). The control field pulses (blue curves) were all normalised to 1. The typical retrieval, using a single read out pulse, which we have already seen many times before, is illustrated in Figure 4.26 (b). The retrieval efficiency in this case was  $\sim 17\%$  at  $t = 900$  ns. The second, very small

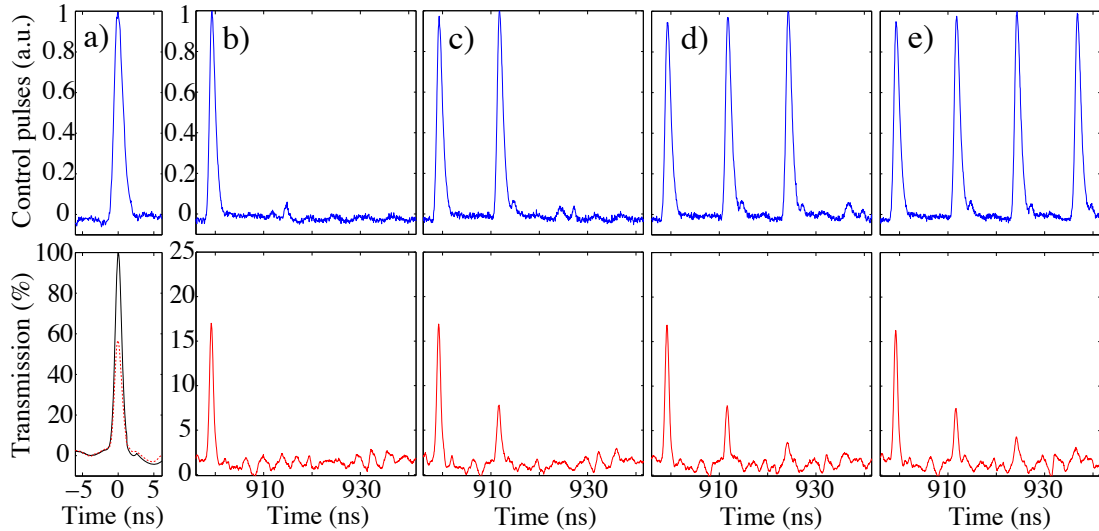


**Figure 4.26:** Complete readout. Blue curves: Control field pulses. Black curve: Incident un-stored signal field. Red dashed curve: Transmitted fraction of stored signal field. Red curves: Retrieved signals. (a) Storage at  $t = 0$  ns. (b) Retrieval with one control pulse at  $t = 900$  ns. (c) Retrieval with two control pulses. (d) Retrieval with three control pulses. (e) Retrieval with four control pulses.

peak that shows up in the control field plot at  $t = 913$  ns, is connected to the response of the fast photodiode to an incident light field and is of no concern.

When the Pockels cell window for selecting the read pulses was increased, more pulses got picked, as illustrated in Figure 4.26 (b). Here two read pulses were picked and the result were two retrieved signals with different efficiencies. This demonstrates that the spin wave coherence inside the atomic ensemble that was not reconverted into a light pulse during the first readout event remained there and could be read out a second time. However, this occurred with a smaller efficiency than the first attempt, because some of the coherence was already retrieved in the first event. The first retrieved signal contained  $\sim 17\%$  of the stored light pulse and the second retrieved signal about  $\sim 10\%$ . Figure 4.26 (c) shows the case, where three read pulses were selected and therefore three retrieved

signals with efficiencies of  $\sim 17\%$ ,  $\sim 10\%$  and  $\sim 5\%$  could be identified. The third retrieved pulse only appeared very weakly because at that time not much coherence was left in the atomic ensemble to be reconverted into a photonic mode. Figure 4.26 (d) illustrates the four retrieval pulses case, where no retrieved signal could be identified during the fourth and last readout attempt. This indicates that the whole spin wave excitation was read out completely from the atomic ensemble in three different temporal modes and that no more coherence was left in the atoms.

Assuming a read efficiency of  $42\%$  ( $\frac{17\% \text{ retrieval}}{40\% \text{ storage}}$ ) during a single retrieval event of the stored excitation matches the observed data very well. After the first read event,  $23\%$  of the initially stored signal was left as a spin wave excitation, leading to a theoretical value of  $9.8\%$  for a second retrieved pulse. About  $13\%$  of the initial excitation remained, leading to a third read event with a value of  $5.5\%$ . The last retrieval at the fourth event theoretically should be  $\sim 3\%$ . However, this was not observable because of the detector noise.

### 4.7.2 Balanced and pyramid readout

After the observation of multiple readout events that lead to a complete retrieval of the stored excitation (see Section 4.7.1), some other retrieval patterns were investigated. The reason for this is that in future experiments entanglement could be created between the retrieved signal and the atomic ensemble if a single photon were stored and the retrieval efficiency were set to  $50\%$ . If a second read pulse extracted the rest of the spin wave excitation, entanglement could be created between the different time bins of the first and the second retrieval cycle.

A balanced and pyramidal retrieval pattern is illustrated in Figure 4.27. The

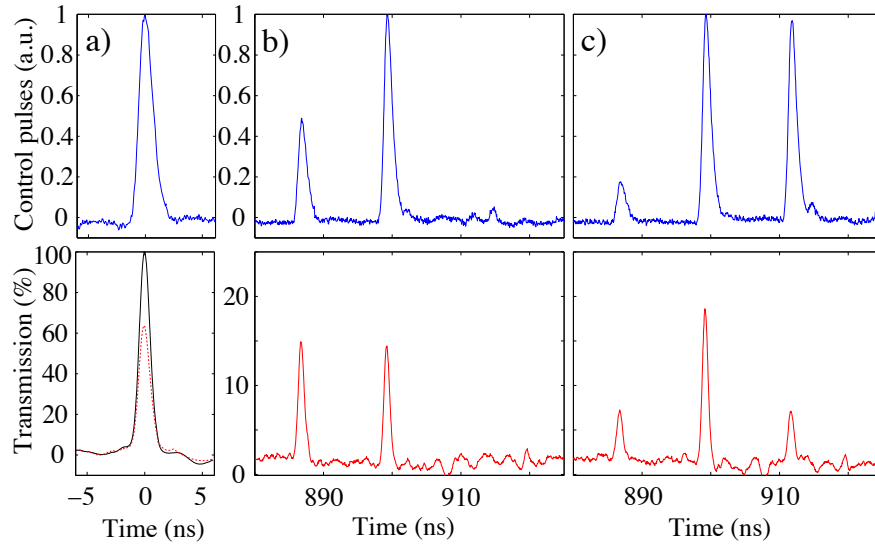


**Figure 4.27:** Balanced and pyramid readout. Blue curves: Control field pulses. Black curve: Incident un-stored signal field. Red dashed curve: Transmitted fraction of stored signal field. Red curves: Retrieved signals. **(a)** Storage at  $t = 0$  ns. **(b)** Retrieval with two increasingly strong control field pulses starting at  $t = 888$  ns. **(c)** Retrieval with three increasingly strong control field pulses starting at  $t = 888$  ns.

figure is arranged in the same way as Figure 4.26. Figure 4.27 (a) illustrates the storage of an incident signal pulse with an efficiency of 40% (black curve). 60% of the incident signal field were transmitted (dashed red curve). The blue curves represent the control field pulses. Figure 4.27 (b) shows the retrieval of two signal pulses (red curves) each with an efficiency of  $\sim 15\%$  caused by a doubling of the control pulse energy from the first to the second read pulse (blue curves). Figure 4.27 (c) illustrates a pyramidal retrieval sequence of three pulses with efficiencies of  $\sim 7\%$ ,  $\sim 18\%$  and  $\sim 7\%$ , caused by the control pulse sequence indicated.

The demonstrated multiple readout of a single stored excitation provides interesting new paths to various types of experiments. It can be used for example to obtain 100% recall of a stored excitation by reading out the stored spin wave until

it is completely retrieved. Furthermore, provided the memory operates with true single photons and the storage and retrieval efficiencies can be chosen arbitrarily, entanglement swapping schemes from light-light entanglement to light-matter entanglement, matter-matter entanglement and back to light-light entanglement can be envisioned.



# Chapter 5

## Single-photon-level experiments

All experiments up to this point were carried out using weak coherent signal pulses with an average of  $\sim 1000$  photons per pulse. It was demonstrated that these light pulses could be stored and retrieved for a significant amount of time in an efficient and phase-coherent fashion (see Section 4.5.3 & 4.5.4). However, in order to make this technology useful for quantum applications in a future quantum information technology network, where quantum information is processed, stored, and transferred over long distances<sup>[15,23]</sup>, memories capable of operating with single photons are essential.

Previously, single photons were stored and retrieved in a warm atomic vapour via the EIT protocol, but the noise level was not measured<sup>[41]</sup>. Other experiments that focussed on studying noise in warm atomic-vapour EIT systems concluded that the noise floor was too high for quantum applications due to *collision induced fluorescence*<sup>[64,65]</sup>. This drawback could be circumvented by operating EIT quantum memories in laser-cooled or cryogenic environments<sup>[47–49,78,94,131–133]</sup>. These techniques, however, are bulky and technically complex, which is why easy-to-

operate, room-temperature quantum memories would be favourable if these devices were to be used in potentially isolated, unmanned locations within an inter-continental quantum network (e.g. as part of a quantum repeater positioned at the bottom of an ocean). Note that also continuous variables quantum memories were demonstrated at room temperature<sup>[50,51]</sup>. These memories, however, operate in a completely different way. In particular it is not possible to retrieve stored single photons on demand from these memories, which is why these different techniques are not directly comparable.

In this chapter the noise floor of the Raman quantum memory is investigated. Furthermore, it is demonstrated that unconditional single-photon-level operation at room temperature is possible using an ensemble of thermal caesium atoms<sup>[44]</sup>.

## 5.1 Technical upgrades

In order to be able to carry out single-photon-level experiments, new pieces of equipment were purchased and parts of the old apparatus were improved. In the following I am going to explain in detail what adjustments and modifications were made.

### 5.1.1 Improved filtering

In the previous experiments the control field pulse contained a maximum energy of 12 nJ. This corresponded to a control field photon number of  $5 \times 10^{10}$  per pulse. The combined spectral and polarisation extinction ratio of the etalons and the polarisers was  $10^9$  (see Section 4.4). Therefore, theoretically about 50 leaked photons per pulse would be expected. This is too little to be detected with the

former fast APD (see Section 3.9.4), but visible with a *single photon counting module* (SPCM, see Section 5.1.2) and, of course, problematic for an optical memory operating at the single-photon-level. Therefore the spectral rejection ratio was increased by adding another etalon in front of the SPCM, giving a total extinction ratio of  $10^{11}$ , sufficient for replacing the current fast APD with the SPCM and ensuring that this device was not damaged by excessive photon flux.

### 5.1.2 Single Photon counting modules

The *single photon counting modules* (SPCM), purchased from Perkin Elmer, have a dark count<sup>1</sup> rate of  $\sim 250$  photons per second. They have a quantum efficiency of about 50% at 852 nm and a dead time<sup>2</sup> of several hundred nanoseconds after a photon was registered (click). The temporal pulse shape of a single photon cannot be observed with this technology, but statistics have to be accumulated over many thousand experiments as will be discussed in Section 5.1.5. The SPCM produces a TTL pulse whenever a photon is detected. This includes dark counts, noise photons from resonant fluorescence, ambient background noise but also the stored and the retrieved photons we would like to measure. The way to distinguish between them will become clear in Section 5.1.4.

### 5.1.3 FPGA

A *field-programmable gate array* (FPGA), is basically a small computer that operates independently of the other lab computers and can be programmed to carry out a specific task. We used an FPGA programmed for counting single TTL

---

<sup>1</sup>A dark count is electric noise that is intrinsic to any SPCM.

<sup>2</sup>The dead time is the time after a photon is registered. The SPCM processes the information and therefore is not responsive to any other impinging photons during this time interval.

pulses, e.g. the signal provided by the output of a single-photon counting module (see Section 5.1.2). Subsequent experiments were operated with a repetition rate of 3.09 kHz. Measuring  $\sim 3000$  clicks per second with the FPGA at a detection efficiency<sup>1</sup> of 3.5% meant that a light field with an average photon number of  $\bar{n} \sim 28$  per pulse was incident. Therefore, if operation at the single-photon level were desired, the signal field would have to be attenuated by a factor of  $\sim 30$ .

In consecutive experiments a time-to-amplitude converter (TAC, see Section 5.1.4) and a multi-channel-analyser (MCA, see Section 5.1.5) were used for acquiring single-photon-level histograms (e.g. Figure 5.1).

#### 5.1.4 Time-to-amplitude converter

In order to be able to distinguish between the random noise and the desired stored and retrieved photons a *time-to-amplitude converter* (TAC) was used. This device receives a first trigger (e.g. TTL pulse) from the master clock of the experiment (the Pockels cell that selects the pulses for storage and retrieval) and a second trigger from the SPCM. The TAC then produces a voltage on a scale from 1 - 10 V proportional to the time difference between the two trigger pulses. Thus the clicks that correspond to random noise produce a signal spread over whole voltage range, whereas the storage and the retrieval event, which always occur at the same time, produce distinct voltages only. These voltages are then fed forward to a counting device, which will be described in Section 5.1.5.

---

<sup>1</sup>The detection efficiency is determined by the transmission of the three etalons (see Section 3.7.2), the polarisers (see Section 3.7.3), the fibre coupling and the quantum efficiency of the SPCM (see Section 5.1.2).

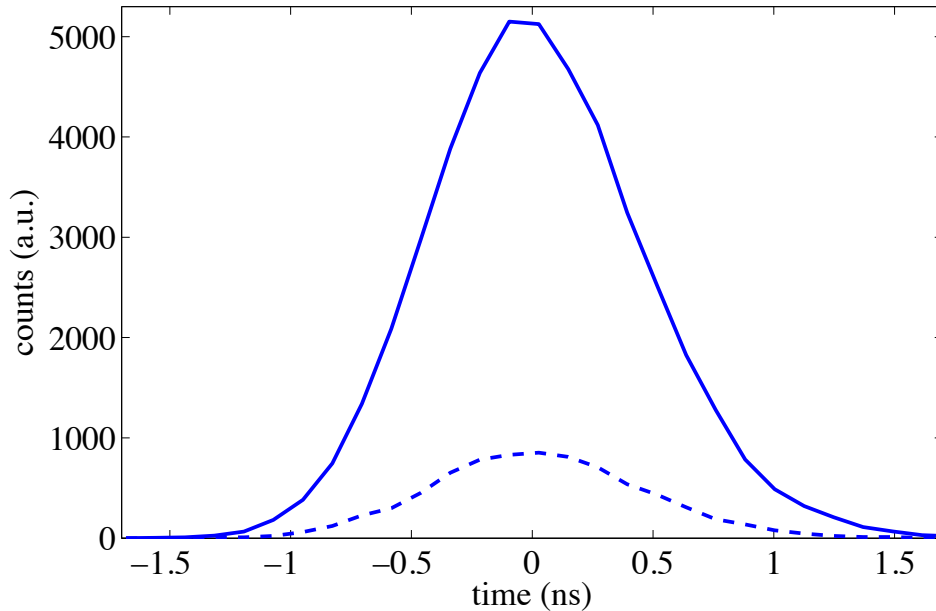


**Figure 5.1:** Single photon level experiments. Histogram/single photon level signal field accumulated over 370,000 experiments. Solid line: Average photon number per pulse  $\bar{n} = 3.6$ . Dashed line: Average photon number per pulse  $\bar{n} = 0.6$ .

### 5.1.5 Multi-channel analyser

This counting device is called a *multi channel analyser* (MCA). It is a remarkable piece of electronics that enables the creation of a histogram (see Figure 5.1) by transforming the voltage signal received from the TAC into a time bin. The amount of time-bins, and thereby the resolution of the histogram, can be chosen by the user by manually selecting a time interval (1 - 10,000 ns) and its time bin resolution (up to 16,384). The time interval is divided by the resolution number, thereby defining the temporal width of each time-bin. These steps define the width and the resolution of the histogram. If a voltage is detected, it is put to the corresponding time-bin and this way, when the experiment is repeated thousands of times, a histogram is established. Both the multi-channel analyser and the time-to-amplitude converter were purchased from Canberra UK LTD.

For the experiment illustrated in Figure 5.1 the MCA time window was set to 2,000 ns with 16,384 time bins, giving a temporal resolution of  $\sim 120$  ps. The weak coherent fields were generated the same way the signal fields were generated before (see Section 4.4), but in addition neutral density filters (ND) were used to attenuate the signal field by another factor of  $10^4 - 10^5$ , reducing the average photon number per pulse to  $\bar{n} \sim 1$ . Figure 5.1 shows the histograms of two different single-photon-level signal fields, each accumulated over 370,000 experiments and centered around time  $t = 0$ . The Gaussian pulse shape is recognisable, but it is broadened due to the  $\sim$  ns timescale detector jitter of the SPCM. Summing over all the detected clicks and dividing this number by 3.5%, the detection efficiency after the vapour cell, gives  $1.3 \times 10^6$  counts for the solid curve, and  $2.2 \times 10^5$  for the dashed curve, and therefore an average photon number per pulse of  $\bar{n} = 3.6$  for the solid and  $\bar{n} = 0.6$  for the dashed curve.

## 5.2 Results

The previous measurements demonstrated that the detection system reached single-photon-level sensitivity and that subsequent single-photon-level experiments could be carried out.

### 5.2.1 Single-photon-level data & fluorescence noise

Storage and retrieval at the single-photon level was implemented next and the results can be seen in Figure 5.2 (a). The control field pulse energy was 12 nJ, the vapour cell was heated to 62.5°C, the beam diameters were the same as discussed before (see Section 4.4) and the experiment was operated at 3.09 kHz. The data

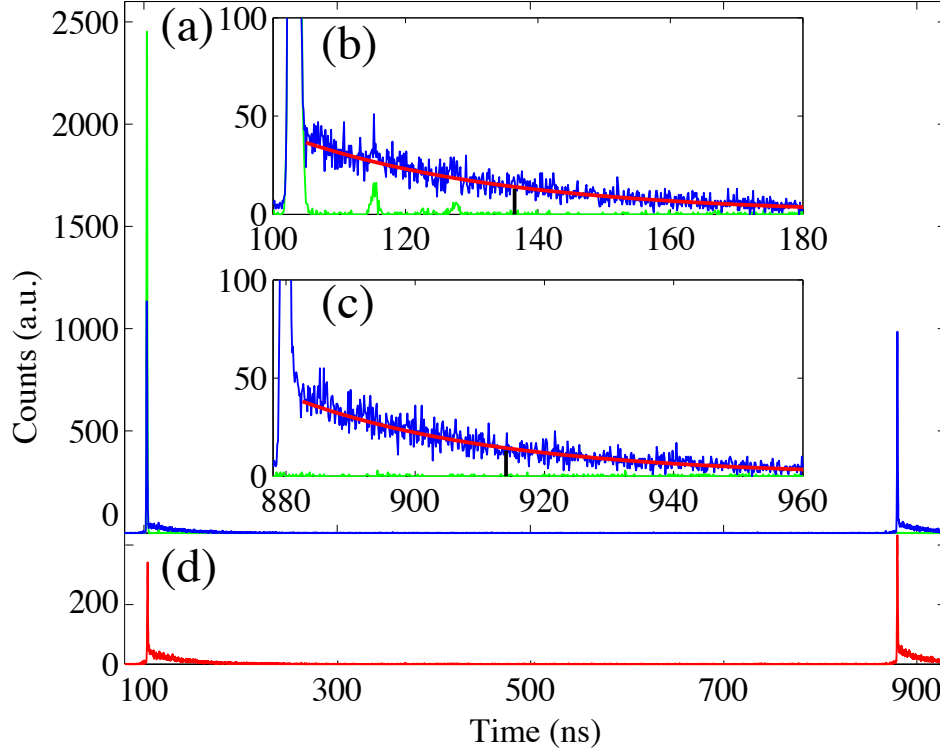


**Figure 5.2:** Single photon level storage and retrieval. (a)  $t_1 = 103$  ns shows the storage and  $t_2 = 880$  ns the retrieval event. Green line: Signal field without a control field. Blue line: Signal field with control field. (b) Zoom around  $t_1$ . (c) Zoom around  $t_2$ . The red curve represents a least squares fit to the exponential fluorescence tail visible in the presence of a control field (blue curve). The  $1/e$  value is indicated by the black lines, giving a decay time of  $\tau \sim 32 \pm 2$  ns. Histograms are accumulated over 360,000 runs. (d) Control field without a signal field and a diode laser.

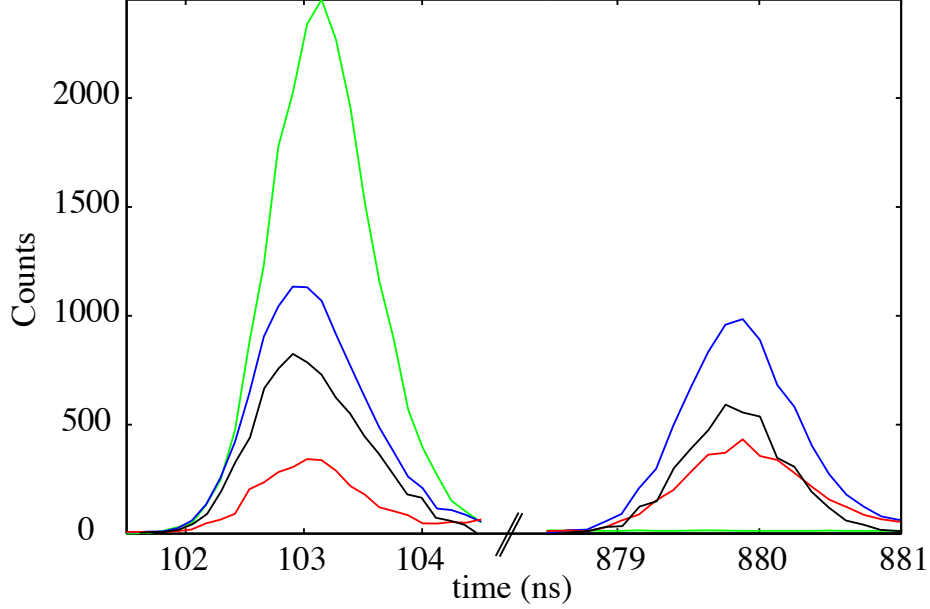
acquisition time was 120 s, corresponding to 370,000 experiments. The average input photon number per pulse was  $\bar{n}_I = 1.6$ , the average retrieved photon number per pulse was  $\bar{n}_R < 1$ , the storage time was set to  $\sim 800$  ns and the overall memory efficiency was about 30%.

Figure 5.2 (b) & (c) show the storage event ( $t = 103$  ns) and the retrieval event ( $t = 880$  ns) in detail. The green curve represents the incident signal without a control field. A signal could only be detected during the storage interval but

not during the retrieval interval because the fast RF switch turned off the signal field during the retrieval process (flat green line). 12.5 ns and 25 ns after the storage time, two smaller green pulses were present because the Pockels cell was not completely turned off and therefore subsequent light pulses were not entirely extinguished. This, however, was not a problem, because the subsequent pulses were very weak compared to the first picked pulse ( $< 1\%$ ).

The really interesting thing to note is, that the green curve returns to zero after the incident signal pulse has passed at about  $t = 105$  ns, but the blue curve (signal and control field together) does not. Instead, a noise tail is attached to the original stored signal pulse. The control field alone (see Figure 5.2 (d)) caused a much weaker signal during the storage and retrieval time frame compared to the case when the memory is operated with an input field (see Figure 5.2 (a)). Further details regarding this instantaneous noise will be discussed in Section 5.2.2. Furthermore, however, the same noise tail was present when the control field was sent through the vapour cell alone. The explanation was fluorescence noise, which was caused by the collision-induced excitation of atoms from the ground state and the storage state to the excited state by the control field, and subsequent spontaneous emission and relaxation. Even far from resonance, there were a few collisions of sufficient energy to excite atoms. The long tail was fitted by a least-squares fit (red curve) giving a decay time  $\tau \sim 32 \pm 2$  ns, which matched well with the excited state lifetime of caesium<sup>[95]</sup>.

However, while such collision-induced fluorescence limits the usefulness of other, more narrowband room-temperature quantum memories, as shown in<sup>[64,65]</sup>, in our extremely broadband memory, the 30 ns time scale of these emissions is much longer than the duration of the storage and the readout event, which is set



**Figure 5.3:** Single photon level data and instantaneous noise. Zooms around the incident ( $t_1 \sim 103$  ns) and retrieved ( $t_2 \sim 880$  ns) pulse showing the: incident signal (transmitted/retrieved signal with no control field) (green); transmitted/retrieved signal with the control field (blue); and noise (control field only) (red). Pure input signal and pure retrieved signal without any noise (black curve), i.e. blue curve minus the red curve. Histograms are accumulated over 360,000 runs.

by the 300 ps pulse width and the timing jitter of the detector, and therefore can completely be suppressed by time-gating the detection system. Instantaneous noise is a different issue and will be investigated in Section 5.2.2.

### 5.2.2 Instantaneous noise

In addition to the fluorescence noise, as discussed in Section 5.2.1, there is a second type of noise that is synchronous with the signal and the control field and therefore cannot be eliminated by time gating. This sort of noise is investigated further by taking a close look at the storage and the retrieval event.

The green curve in Figure 5.3 represents the signal field without a control field and the blue curve is the stored ( $t = 103$  ns) and the retrieved signal ( $t = 880$  ns). The average input photon number per pulse was  $\bar{n}_I = 1.6$  and the average retrieved photon number per pulse was  $\bar{n}_R = 0.58$ . The question is, how much of the retrieved signal was contributed by noise, for example caused by spontaneous Raman scattering or leakage of the strong control field pulse?

In order to answer that question, the control field was sent into the vapour cell without the signal field and the diode laser prepared the system as usual. The noise measurement is illustrated by the red curve in Figure 5.3. Its contribution was an average noise photon number per pulse of  $\bar{n}_N = 0.25$  during the storage and the readout event. This means that in the current case the pure retrieved photon number per pulse was  $\bar{n}_N = 0.33$ , corresponding to a single-photon-level memory efficiency of  $\sim 20\%$ .

The noise contribution of 0.25 photons represents the *unconditional noise floor* of the experiment. This is really important to note, because this number either allows or prevents the operation of a quantum memory in a continuous fashion without the need for post-selection of the retrieved photons. For the presented Raman memory, the noise floor is already much lower than a single photon and therefore enables the operation of a Raman-based quantum memory in an unconditional way even at room temperature<sup>[44]</sup>, as will be discussed in greater detail in Section 5.2.3. Contrast this to the papers suggesting that single-photon-level operation in a warm alkali environment is not possible<sup>[64,65]</sup>.

### 5.2.3 Origins of instantaneous noise

Previously we measured the instantaneous noise and found that it was much less than a single photon. But what is it composed of and can we reduce it even further? Two possible noise sources are the leakage of the strong control field and spontaneously scattered Raman photons. We investigated the former noise source by removing the vapour cell from the experimental setup and measuring the leakage of the control field through the polariser and three type 1 etalons, which gave a total filtering ratio of  $> 10^{11}$  (see Section 3.7.3). The measured signal was so low that it was not even visible in the histogram plotted in Figure 5.3. Therefore we ruled out the leakage of the control field as a contribution to the observed noise level of 0.25 photons. This left spontaneous Raman scattering (SRS) as a possible noise source. As SRS depends on the population difference of the ground state and the storage state<sup>[44,83]</sup>, we decided to investigate the noise dependence on optical pumping, which in turn affects the population difference of the ground state and the storage state. The results are displayed in Figure 5.4. The blue shading in Figure 5.4 (a) indicates optical pumping on the  $|3\rangle \leftrightarrow |2\rangle$  ('blue') transition, whereas the red shading represents optical pumping on the  $|1\rangle \leftrightarrow |2\rangle$  ('red') transition. Increasing the pump power on the blue transition partially suppresses the noise, although it rapidly levels off at an average of 0.25 photons per pulse, while the noise level rises linearly with increasing pump power on the red transition.

These observations are well-described by a simple noise model (see Section 2.10.2) based on *spontaneous Raman scattering* (SRS)<sup>[134,135]</sup>, in which Stokes and anti-Stokes photons scattered during the control pulse are both transmitted through our etalon-based filters (see Section 3.7.2) and detected as noise. For the

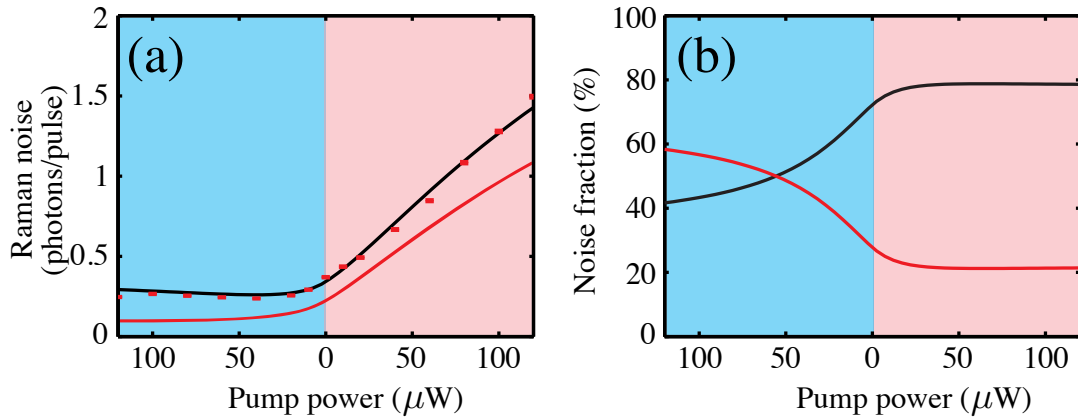


**Figure 5.4:** Spontaneous Raman scattering (SRS) noise. (a) Blue shaded area: Optical pumping on the  $|3\rangle \leftrightarrow |2\rangle$  (blue) transition. Red shaded area: Optical pumping on the  $|1\rangle \leftrightarrow |2\rangle$  (red) transition. The red points are data and the black line is a theoretical prediction of noise due to spontaneous Raman scattering. The red solid line shows the predicted noise due only to Stokes scattering (b) Predicted fractional noise contributions from Stokes (black curve) and anti-Stokes (red curve) light. Theoretical details can be found in Section 2.10.2.

experiment we had  $d = 1900$ ,  $\gamma = 16$  MHz,  $\Delta = 15$  GHz and  $W = 30$  GHz. To correctly describe our noise measurements, we find  $P_s = 84$   $\mu\text{W}$  and  $\kappa = 0.12$  using a least-squares fit. This high value for the optical depth is not a measured experimental value. It is a theoretical value based on the assumption that all the atoms are in single magnetic sub-level and can be addressed with a narrowband laser. Using Equation (2.27) with a specific caesium  $D_2$  line dipole matrix element and the total number of atoms at  $62.5^\circ\text{C}$ <sup>[95]</sup> addressed by the light fields leads the aforementioned value. As the Raman memory operates far off-resonant the effective optical depth is much much lower.

Since the model does not include collision-induced fluorescence<sup>[64]</sup> or leakage of the control, this suggests that these contributions are negligible. Furthermore, as shown in Figure 5.4 (a) & (b), around 60% of the noise affecting the quantum memory is emitted at the anti-Stokes frequency (when operated with maximal

blue pumping) and could be removed using further spectral filtering. This would already bring the true unconditional noise floor down to 0.1 photons per pulse, resulting in an unconditional signal-to-noise ratio (SNR) of 10:1 for single-photon retrieval. The remaining signal-frequency (Stokes) noise would remain even if the optical pumping and spectral filtering were perfect. It has its origin in four-wave mixing seeded by spontaneous anti-Stokes scattering. However, even this noise could be eliminated if the anti-Stokes channel were suppressed or rendered much weaker than the Stokes channel, for instance by operating the memory closer to resonance, so that the anti-Stokes detuning were relatively much larger. Finally, although our fibre-coupled detection system was optimised for the mode of the signal, the noise was scattered mostly into the control mode<sup>[104,105]</sup>, which suggests that the noise floor could be reduced further by angle tuning the control field<sup>[93]</sup>.

In order to assess the effects of the measured noise floor of 0.25 photons per pulse in a quantum application, we consider a simple thought experiment based on the DLCZ quantum repeater protocol<sup>[15]</sup>. By storing one half of an entangled state and averaging correlations over signal and noise photons retrieved from the memory, one can show that this noise level is already low enough to allow quantum key distribution via the Ekert protocol<sup>[136]</sup>, in which violation of Bell's inequality certifies the quantum channel<sup>[44]</sup>. Therefore the presented far off-resonant Raman memory can be considered a genuine quantum-ready optical memory, functioning at room temperature.



# Chapter 6

## Polarisation encoded qubit memory

After the experiment was upgraded to single-photon-level sensitivity, as was discussed in Chapter 5, we managed to store and retrieve weak coherent states at the single-photon level. Furthermore, we demonstrated that the noise levels were low enough to store and retrieve true single photons (see Section 5.2.2) and that the far off-resonant Raman memory was capable of serving as a useful quantum application<sup>[44]</sup>. However, it was not possible to carry out genuine single-photon experiments because no single-photon source with the right bandwidth was available. But there are plans for building such a device as will be discussed further in Chapter 8.

In the meantime, we thought about ways of using this new quantum memory architecture for applications that demonstrated its usefulness. Polarisation-encoded qubit storage, for example, was an experiment that could be realised with the current, slightly modified apparatus as will be discussed in Section 6.1.

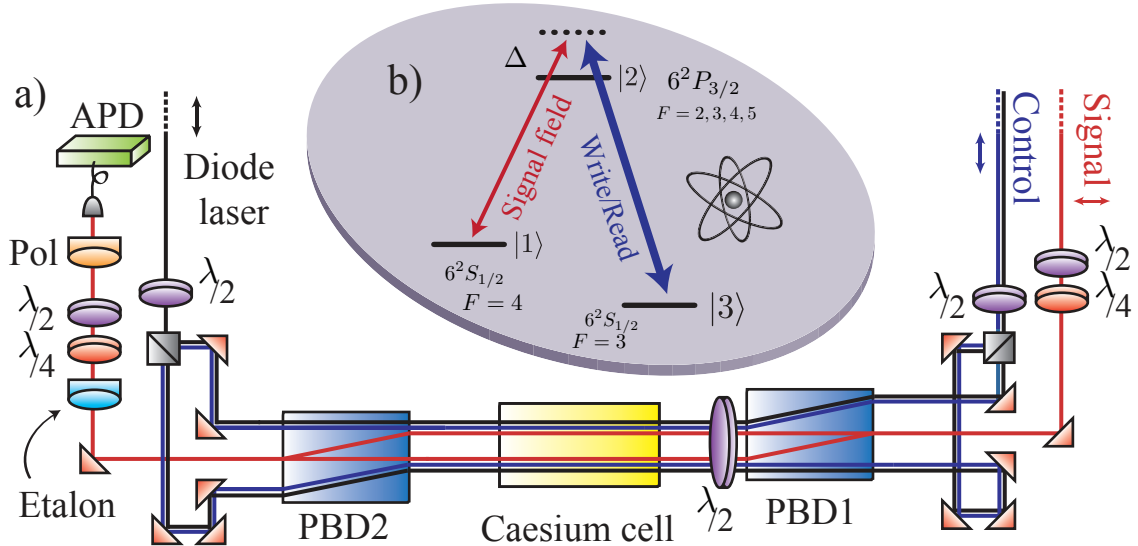


**Figure 6.1:** Qubit memory experimental setup and  $\Lambda$ -level system. (a) Experimental setup. The polarising beam displacers (PBDs), introduced in Section 3.11, split a collinear input beam with crossed polarisations into two parallel, physically separated output beams with horizontal ( $\leftrightarrow$ ) and vertical polarisation ( $\updownarrow$ ). Thereby, two independent parallel quantum memories are established inside the vapour cell. (b)  $\Lambda$ -level system indicating the atomic caesium structure and the applied laser fields.

## 6.1 Qubit memory — experimental setup

The Raman memory is approximately a single-mode memory at relatively small control field powers<sup>[39,88]</sup>. This means that one polarisation mode can only be stored per spin wave excitation and that a different experimental design has to be used in order to store two orthogonal polarisation modes. The solution was to employ two independent atomic ensembles. The experimental setup is illustrated in Figure 6.1. The laser pulses for the signal field and the control field were derived from the same laser oscillator as discussed before in Section 3.3.1. The signal field was modulated with an EOM (see Section 3.5.1) and the appropriate sideband was selected by using Fabry Perot Etalons (see Section 3.7.2). The diode

laser beam was produced by an ECDL (see Section 3.3.2) and turned on and off with an AOM as described in Section 3.3.2.2. The control field and the diode laser were vertically polarised ( $\updownarrow$ ) and the signal field was horizontally polarised ( $\leftrightarrow$ ). This was extremely important for the beam routing in the polarisation interferometer as can be seen in Figure 6.1 (a).

The polarisation interferometer was constructed from two polarising beam displacers (PBDs), which were introduced in Section 3.11. Vertical input polarisations pass straight through the PBD whereas horizontal polarisations are deflected and emerge parallel but displaced by 8 mm compared to the vertical components. In the signal beam path there was  $\lambda/2$  and a  $\lambda/4$  wave plate which allowed for preparing arbitrary input polarisations. As illustrated in Figure 6.1 (a), the signal field was split into two components by the PBD, leading to two separate, orthogonally polarised input fields that entered the vapour cell 8 mm apart from each other. These two fields were stored independently in two different spin waves, one for horizontal and one for vertical polarisation, in the same vapour cell. The  $\lambda/2$  wave plate inside the interferometer was set to rotate each polarisation by  $90^\circ$ , because otherwise a beam that passed straight through the first PBD would also pass straight through the second PBD and it would not be possible to create two different ensembles with individual signal fields, control fields and diode lasers .

As mentioned before the diode laser and the control fields were initially polarised vertically, but a  $\lambda/2$  wave plate and a polarising beam splitter cube (PBS) divided each of the laser beams into two, one with a horizontal polarisation and one with a vertical polarisation and each with adjustable beam powers. The two diode laser beams and the two control fields were then directed into the vapour

cell such that the two orthogonally polarised signal fields each overlapped with their corresponding diode laser and control laser beams, in order to create two independent single mode memories, as was described before in Section 4.4. The two ensembles were located 8 mm apart from one another and the beams were separated by the PBDs. The vapour was heated to 62.5°C and all the laser beams were focussed into and re-collimated after the vapour cell with 30 cm lenses, which are not shown in Figure 6.1 (a). The beam diameters were the same as in the single memory case described in Section 4.4:  $\varnothing \sim 350 \mu\text{m}$  for the signal and the control field and  $\varnothing \sim 1 \text{ mm}$  for the diode laser across the entire length of the vapour cell (7 cm).

At the second PBD, the two signal field paths were recombined and emerged as a single laser beam with a polarisation identical to the initial input polarisation before the interferometer, but with a 90° rotation for both polarisations due to the  $\lambda/2$  wave plate inside the interferometer. Then three type-1 etalons with an FSR = 18.4 GHz (see Section 3.7.2) were tuned for transmission of the signal field and extinction of any possible leak of the control field or the diode laser through the polarisation optics (PBDs, see Section 3.11). The subsequent  $\lambda/4$  and  $\lambda/2$  wave plates and the Glan Thompson polariser (Pol), aligned for transmission of vertically polarised light fields, comprised the polarisation analysis stage of the experiment. As mentioned before, any arbitrary input polarisation could be prepared before the interferometer, and here any prepared polarisation could be analysed before the signal was fibre-coupled and detected on the single photon counting module (SPCM), introduced in Section 5.1.2.

The spatial and temporal alignment of the polarisation interferometer required high precision because the laser beams had to overlap well in each of the two en-

sembles in order to get the Raman memory process to take place. The challenge was space. As discussed above, the beam separation caused by the beam displacers was  $\sim 8$  mm, which meant that the separation of the input beams, namely the signal, control and diode, had to be 8 mm, too, before they entered the PBD. This was not possible by using standard 1" mirrors and standard mirror mounts because they were too bulky. The solution to bring the input beams closely together were small dielectrically coated prisms (Thorlabs MRA10 E03) mounted on a table mount, such that they could be approximated to the signal field beam.

The timing of the polarisation interferometer was adjusted by delay stages in each of the two control field paths. They are not shown in Figure 6.1 (a). The signal field set both the physical location and the timing for the interaction, which was why the control field and the diode laser beam had to be adjusted accordingly.

## 6.2 Quantum process tomography

In an isolated quantum system, the dynamics is always unitary. However, our memory is not isolated, and there are losses, which can degrade the coherence of the memory (see Section 4.6.2). Arbitrary non-unitary dynamics can always be represented by a completely positive map, or *quantum process*<sup>[137]</sup>,

$$\rho_{\text{out}} = \sum_{m,n} \chi_{mn} \Gamma_m \rho_{\text{in}} \Gamma_n, \quad (6.1)$$

where the *process matrix*  $\chi_{mn}$  is a positive Hermitian matrix with unit trace that contains all the information about the dynamics, and the  $\Gamma_{m,n}$  represent an orthonormal basis for the space of density matrices. Here  $\rho_{\text{in,out}}$  are the density

matrices of the initial and final states. For unitary dynamics  $\chi$  is rank-1, and the process is *pure*. In general the coherence of a process is quantified by the process purity  $P = \text{tr}\{\chi^2\}$ , which falls below 1 for non-unitary dynamics. To examine the coherence of our memory we reconstruct the process matrix for polarisation storage using *quantum process tomography* (QPT)<sup>[137,138]</sup>. Here the process purity determines whether or not a quantum memory is able to store and retrieve arbitrary photonic qubit input polarisations and preserve the quantum coherences established between different polarisation modes.

Weak classical pulses (i.e. coherent states) were used for the measurements, but the results also hold for single-photon inputs because the click statistics of intensity measurements made on single photons sent through a linear optical system are always classical<sup>[87,139,140]</sup>.

QPT is carried out by preparing a set of input polarisation states that span the Bloch sphere — this is the standard set of mutually unbiased bases (or MUBs<sup>[141,142]</sup>), consisting of horizontal (H), vertical (V), right and left circular polarisation (R,L) and diagonal and anti-diagonal polarisation (D,A). Each of these polarisation states can be prepared by the  $\lambda/2$  and  $\lambda/4$  wave plates in the signal beam path before the interferometer (see Figure 6.1 (a) and Table 6.1 (a)), and then stored in the polarisation memory.

The field emerging from the memory (either directly transmitted, or retrieved after storage) is then directed through a second set of  $\lambda/4$  and  $\lambda/2$  wave plates and a polariser, representing the analysis stage, where projective measurements onto arbitrary polarisation states can be performed — measurements are made corresponding to projections along each of the states comprising each MUB (see Table 6.1 (b)). In total, then, 6 measurements are made on each of the 6 input

(a)			(b)		
Target state	HWP setting	QWP setting	Target state	QWP setting	HWP setting
H	0°	0°	H	0°	0°
V	45°	0°	V	0°	45°
D	22.5°	45°	D	45°	22.5°
A	67.5°	45°	A	45°	67.5°
R	45°	45°	R	45°	45°
L	0°	45°	L	45°	0°

**Table 6.1:** (a) State preparation. Wave plate settings for the preparation of the input polarisation states that span the Bloch sphere – this is the standard set of mutually unbiased bases (MUBs<sup>[141,142]</sup>). (b) State analysis. Wave plate settings for measurement of the polarisation states that comprise the standard set of mutually unbiased bases.

states, giving a total of 36 measurements.

For the case of polarisation qubit storage, where  $\rho_{\text{in,out}}$  are  $2 \times 2$  density matrices representing the input and output polarisation states, it is convenient to write the process matrix in the Pauli basis, where  $\Gamma_0 = I$  is the identity operator and  $\Gamma_{1,2,3} = \{X, Y, Z\}$  are the Pauli matrices. Numerical convex optimisation techniques are employed to ensure that the reconstructed matrix is strictly physical<sup>[137]</sup>, while satisfying the criterion of maximum likelihood<sup>[24]</sup>.

For the specific case of polarisation, a completely incoherent process has a purity of  $P = 1/2$ , while  $P = 1$  corresponds to perfect coherence. The  $X$  process indicates a bit flip with no phase change (e.g.  $H \rightarrow V$ ),  $Y$  represents a bit flip with an additional phase  $\Phi = \pi/2$  (e.g.  $H \rightarrow V \cdot e^{i\pi/2}$ ),  $Z$  represents a phase flip of one of the polarisation channels (e.g.  $V \rightarrow V \cdot e^{-i\pi}$ ) and  $I$  is the identity matrix (e.g.  $H \rightarrow H$ ).

An entirely pure process with a purity of  $P = 1$  is for example represented by i) a  $X$  process or a  $Y$  process with  $\chi_{XX} = 1$  or  $\chi_{YY} = 1$  in the process matrix,

depending on whether the phase difference of the interferometer is  $\Delta\Phi = 0^\circ$  or  $90^\circ$ , or by ii) an equal superposition of  $X$  and  $Y$  processes with  $\chi_{XX} = 0.5$ ,  $\chi_{YY} = 0.5$  and their coherences  $\chi_{XY} = 0.5$  and  $\chi_{YX} = 0.5$ , which is the case if the phase difference is  $\Delta\Phi = 45^\circ$ . If the phase of the polarisation interferometer fluctuates, the process purity is affected and a redistribution among the diagonal elements and/or a reduction of size of the off-diagonal elements of the process matrix takes place, which indicates an impure process.

### 6.3 Results

Using the technique for characterising the memory process, described before in Section 6.2, several experiments were carried out in order to determine whether or not the Raman-based polarisation memory was able to preserve the coherence between the two, physically separated polarisation modes.

The two memories were adjusted by preparing the  $H$  and  $V$  polarisation independently and thereby selecting one of the two memories individually. The transmitted signal through each memory was balanced with respect to the other memory on the fast APD, introduced in Section 3.9.4, by tilting the second PBD, ensuring that the detected signal was equal from both memories. The signal field contained about 1000 photons. Then a similar procedure was performed for the retrieved signal from both memories. However, if the total memory efficiencies differed, not the PBD but the control field power for the two memories was adjusted such that balanced retrieval was observed at the APD for both memories. This alignment procedure ensured that maximum visibility for the process purity could in principle be achieved.

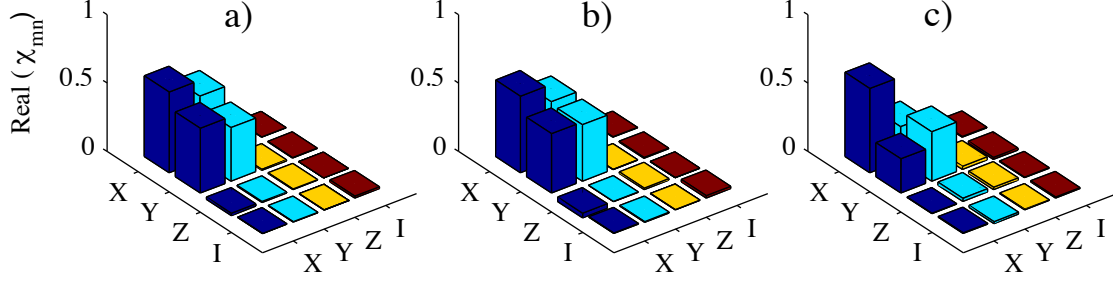


**Figure 6.2:** Process tomography at 400 ns. Process matrices  $\chi$  for the (a) bare interferometer without a memory, (b) transmitted, un-stored signal with memory cell, (c) retrieved signal from the memory. The process purities for these three situations are  $95\pm 0.5\%$ ,  $86\pm 1.7\%$  and  $64\pm 1.4\%$ . The errors are estimated by a Monte-Carlo simulation, in which Poissonian noise on the photon count statistics is randomly added and the QPT is repeated. The labels  $X$ ,  $Y$ ,  $Z$  and  $I$  denote the Pauli matrices, which are used as a basis for the Kraus operators of the quantum channel. Only the real parts of the process matrices are shown; all elements of the imaginary parts are less than 0.01.

### 6.3.1 Process tomography with 400 ns storage time

For the first process tomography experiments the storage time was set to 400 ns. The experimental parameters were precisely the same as described before in Section 6.1 and the process matrix  $\chi$  was reconstructed by performing the 36 measurements and following the recipe introduced in Section 6.2. The results can be seen in Figure 6.2, where plot (a) shows the process matrix  $\chi$  for the bare interferometer without a vapour cell, (b) shows the case where the memory cell was inserted into the beam path and heated to  $62.5^\circ\text{C}$  but the memory was not operated and only the transmitted signal was observed, and (c) illustrates the process matrix, where the memory was operated in the  $62.5^\circ\text{C}$  hot environment, and the retrieved signal was observed.

Note that there was a half-wave plate after the first PBD inside the polarisation interferometer (see Figure 6.1). This implemented bit flip processes ( $X$ )

and bit flip processes in combination with a phase difference, caused by slight differences in the path lengths of the two interferometer arms ( $Y$ ). The phase difference was  $\Delta\Phi \sim 45^\circ$ , which explained why the process matrix in part a) of Figure 6.2 is dominated by a superposition of  $X$  and  $Y$  operations, even in the bare interferometer case, where no memory was operated. If the  $\lambda/2$  wave plate inside the interferometer were not there,  $Z$  and  $I$  processes would be the dominant parts of the process; however, in the applied experimental configuration these were zero.

Comparing case (a) and (b) with each other looks somehow promising, because the diagonal as well as off-diagonal elements of the process matrix look similar, which means that the coherence within the two memories was preserved. In case (c), however, both off-diagonal elements, representing the coherences between  $X$  and  $Y$ , were reduced due to random phase fluctuations in the interferometer arms, which indicated that the polarisation memory was not able to preserve the coherence well between the two different polarisation channels.

The measurements suggest that the bare Mach-Zehnder interferometer formed by the two PBDs without a vapour cell was highly stable, but as soon as the memory cell was placed in the beam path the process purity  $P$  dropped from 95% to 86% when the transmitted signal was observed. Investigating the retrieved signal lead to a process purity of 64%, still higher than 50%, the maximal achievable process purity for a completely incoherent classical memory.

We conclude from these observations that there was some sort of dephasing mechanism when the heated vapour cell was added to the system. This dephasing effect increased further when the memory was operated and the retrieved signal was observed. It might be that inhomogeneous magnetic dephasing in the two

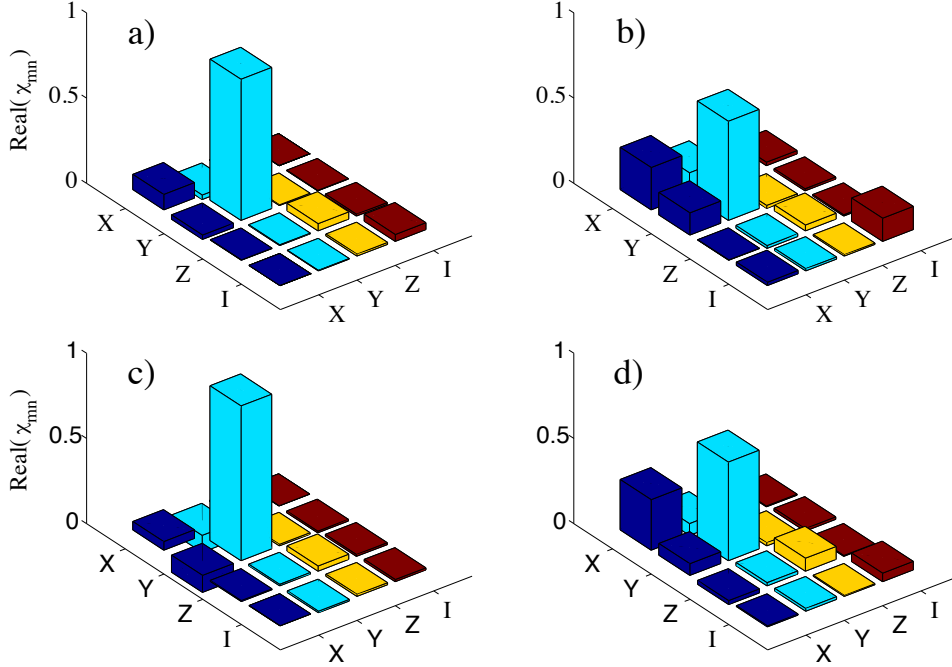


**Figure 6.3:** Process tomography at 12.5 ns. Process matrices  $\chi$ . (a) Transmitted signal at 65°C. (b) Retrieved signal at 65°C. (c) Transmitted signal at 67°C. (d) Retrieved signal at 67°C. The process purities for these situations are  $70\pm 3.5\%$ ,  $46\pm 3\%$ ,  $85\pm 2.3\%$  and  $44\pm 2.1\%$ . The errors are estimated by a Monte-Carlo simulation, in which Poissonian noise on the photon count statistics is randomly added and the QPT is repeated.

ensembles relative to each other caused this dephasing effect, but at this stage it is hard to draw meaningful conclusions and further evidence is required. In Section 6.3.3 the temperature dependence of this effect will be investigated.

### 6.3.2 Process tomography with 12.5 ns storage time

In order to gain further insight into possible dephasing mechanisms, the storage time of the memory was reduced from 400 ns to 12.5 ns. We hoped that reducing the storage time would eliminate possible dephasing mechanisms that affected the polarisation memory on timescales of several hundred nanoseconds, and that

the process purity would increase. Two different sets of measurements were taken for 65°C and 67°C and the results can be seen in Figure 6.3.

In these experiments, the phase difference of the interferometer was  $\Delta\Phi \sim 90^\circ$ , which was why there was only one prominent bit flip process with a superimposed phase shift ( $Y$ ) in the process matrix  $\chi$ . Figure 6.3 (a) & (b) correspond to the 65°C case and Figure 6.3 (c) & (d) show the 67°C case for the transmitted signal and the retrieved signal. Comparing the process matrices for the transmitted and the retrieved case, for both temperatures, reveals similar results like the ones observed before in the 400 ns case (see Figure 6.2), where the process fidelity suffered due to random fluctuations in the two interferometer arms. In the 12.5 ns case, coherences appear in the process matrix describing the retrieved signal, where none are present for the transmitted signal, a clear indication for random phase fluctuations inside the polarisation interferometer. The process purities are  $70 \pm 3.5\%$  and  $46 \pm 3\%$  for the 65°C case and  $85 \pm 2.3\%$  and  $44 \pm 2.1\%$  for the 67°C case for the transmitted and the retrieved signal respectively.

These observations indicate that reducing the storage time from 400 ns to 12.5 ns does not improve the process purity. It is hard to believe that inhomogeneous magnetic dephasing affected the two different ensembles on timescales shorter than 12.5 ns, because the individual memory coherence, as demonstrated in Section 4.5.4, was preserved for 12.5 ns. Therefore, there has to be some other mechanism that afflicts the coherence between the two memories.

### 6.3.3 Interferometer phase fluctuations

The measurements from Sections 6.3.1 & 6.3.2 suggest that the heated vapour cell, regardless of the memory storage time, has some negative effects on the

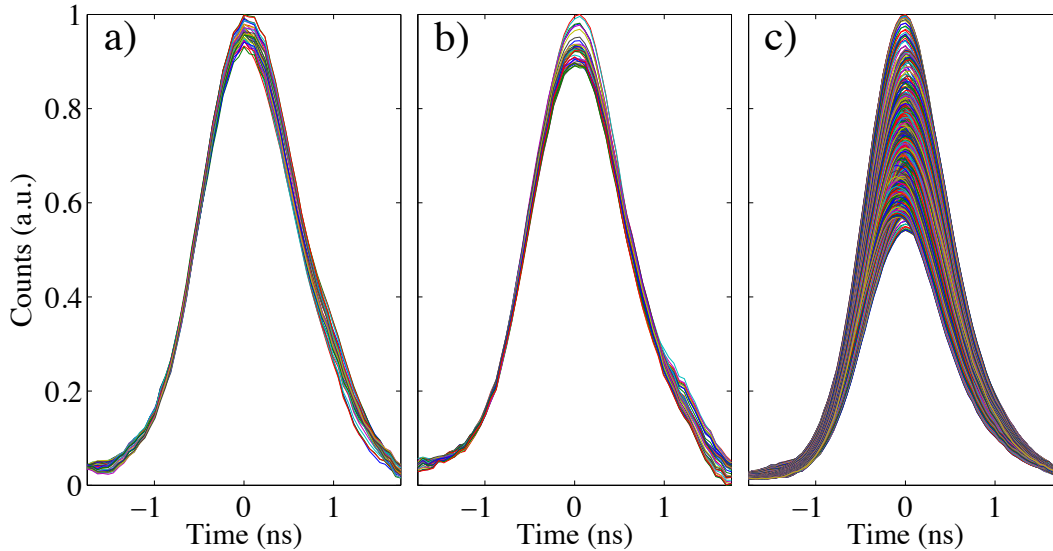


**Figure 6.4:** Polarisation interferometer fluctuations for different QPT settings. Several hundred retrieval experiments for the case of: **(a)** Preparation of  $V$ , detection of  $V$ . **(b)** Preparation of  $A$ , detection of  $A$ . **(c)** Preparation of  $A$ , measurement of  $L$ . Retrieved signals are normalised to 1 and centred around  $t = 0$  ns.

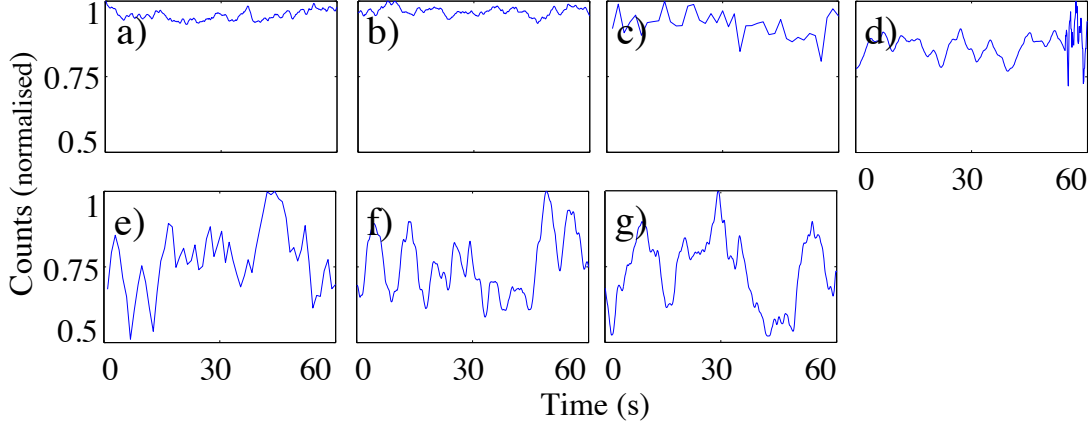
process purity. Furthermore it was observed that there were strong fluctuations for certain settings of the 36 different QPT measurements; particularly for those that reflected the phase relation between the different polarisation memories; like for example for the preparation of  $A$  and the measurement of  $L$ , or  $D$  and  $L$ .

Figure 6.4 shows 600 different retrieval pulses that were obtained from the same polarisation memory experiment. The experiment was carried out in a  $62.5^\circ\text{C}$  hot vapour cell, where the storage time was set to 12.5 ns. Three different wave plate settings out of the 36 QPT settings were investigated. Figure 6.4 (a) represents preparation in  $V$  and detection in  $V$ , which means that only one of the two polarisation memories was selected and therefore the measurements were unaffected by phase fluctuations between the interferometer arms. However, there were small differences in the measured pulses, due to beam pointing issues when

the beam was fibre-coupled. These were the common fluctuations that were observed in all measurements before and which were typically used for calculating the error from the mean. Figure 6.4 (b) shows preparation in  $A$  and detection in  $A$ , which means that both polarisation memories were used equally. Here the fluctuations increased slightly because these measurements were in principle affected by phase fluctuations in the interferometer. However, the fact that the measurement took place in the same basis as the prepared polarisation state lead to small fluctuations only. Figure 6.4 (c) on the other hand, reflecting the preparation of  $A$  and the measurement of  $L$ , shows extremely large fluctuations. This is because this QPT measurement was extremely sensitive to phase fluctuations arising from path length differences in the two interferometer arms. The reason for this is that the measurement basis was shifted by  $90^\circ$  from the preparation basis, and therefore phase fluctuations became much more visible than in the other QPT measurement cases.

These measurements reveal why the measured process purities were very low for the transmitted and the retrieved case in the presence of a hot vapour cell compared to the process purity of the bare interferometer without a vapour cell (see Section 6.3.1). In order to determine the origin of these phase fluctuations of the polarisation interferometer in the presence of a heated vapour cell, a series of measurements for different cell temperatures was taken.

The results can be seen in Figure 6.5, where each data point corresponds to an integrated retrieved pulse, like the ones displayed in Figure 6.4. No memory was operated during these measurements and only the transmitted signal field was observed. The prepared polarisation state was  $A$  and the measurement basis was  $L$  because this was one of the settings where the phase fluctuations of the



**Figure 6.5:** Polarisation interferometer fluctuations vs. vapour cell temperature and time. The detuning  $\Delta$  from the excited state  $|2\rangle$  is  $\sim 15$  GHz. (a) Room temperature. (b)  $T = 35^\circ\text{C}$ . (c)  $T = 40^\circ\text{C}$ . (d)  $T = 50^\circ\text{C}$ . (e)  $T = 60^\circ\text{C}$ . (f)  $T = 67.5^\circ\text{C}$ . (g) Here, the detuning  $\Delta$  is  $\sim 120$  GHz and the temperature of the vapour cell is set to  $T = 67.5^\circ\text{C}$ .

interferometer were most visible, as was discussed before. Each of the displayed graphs in Figure 6.5 shows several hundred measurements taken during a time interval of  $t = 60$  s. Plots (a) - (f) were acquired with the usual detuning of  $\sim 15$  GHz, and temperature settings ranging from  $25^\circ\text{C}$  to  $67.5^\circ\text{C}$ . Plot (g) was acquired for a detuning to the blue of  $\sim 120$  GHz and a temperature of  $67.5^\circ\text{C}$ . As can be seen from the different pictures, the interferometer stability got worse as the temperature of the vapour cell was increased. At  $T = 25^\circ\text{C}$  there were hardly any fluctuations, whereas at  $T = 67.5^\circ\text{C}$ , the fluctuations were close to 50%!

Faraday rotation<sup>[143,144]</sup> might change the polarisation of the signal pulses in the two interferometer arms differently. In order to investigate this, the laser oscillator was tuned about 120 GHz to the blue from the blue resonance ( $|1\rangle - |3\rangle$  transition). If Faraday rotation caused the phase fluctuations, then at this large detuning the effect would be a lot smaller or even be eliminated. However, the

data presented in Figure 6.5 (g) make clear that even at large detunings the interferometer was phase-unstable; the phase fluctuated randomly on a timescale of several seconds.

These results suggest that the presence of a heated vapour cell creates a turbulent environment in which the stability of the polarisation interferometer is decreased. The turbulence is possibly connected to the design of the vapour cell's heating system, the metal container that holds the vapour cell (see Section 3.2.1) and possibly the design of the magnetic shielding. There are plans to use tubes that surround the ends of the vapour cell and extend up to the polarising beam displacers, such that both interferometer arms are contained in the same turbulence-free environment or to design a big container that can be heated homogeneously and houses the whole polarisation interferometer setup.

### 6.3.4 Most recent QPT results

In this section I am going to present the latest experimental results, which show that the installation of the aforementioned tubes (see Section 6.3.3) for heat-shielding purposes had a drastic impact on the stability of the polarisation interferometer and the QPT results. These measurements were carried out by Patrick Michelberger and Duncan England<sup>[145]</sup>, the two DPhil students who took over the experiment. The experimental setup was the same as described in Section 6.1. The only difference was that plastic tubes were placed over the heated vapour cell and the polarising beam displacers enclosing the entire volume in between them. This created a homogeneous temperature environment where no air turbulence could disturb the phase between the two interferometer arms. The plastic tubes had a length of 10 cm each, a diameter of  $\varnothing = 4$  cm and a thickness of 3 mm.

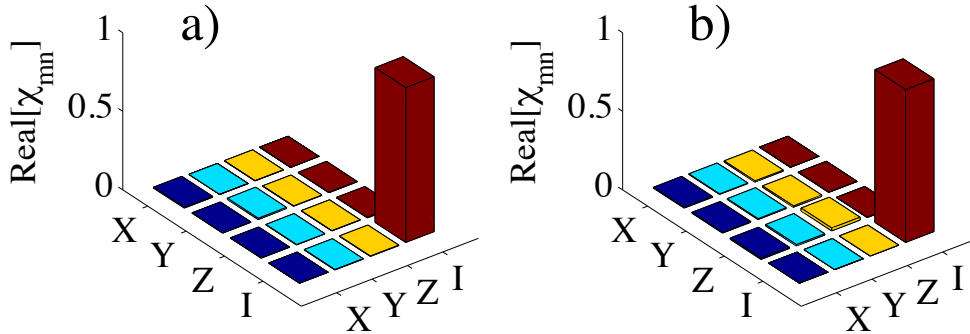


**Figure 6.6:** Stable QPT measurements. **(a)** QPT results for an incident signal without a memory interaction. The process purity is 99%. **(b)** QPT results for a stored and retrieved signal field. The process purity is 99%. This indicates that the polarisation input state and the polarisation output state are completely identical.

Furthermore, three wave plates, a  $\lambda/2$ , a  $\lambda/4$  and a  $\lambda/2$  wave plate, were placed before the QPT analysis stage in the experimental setup (see Figure 6.1). They were used to compensate for the  $90^\circ$  polarisation rotation due to the  $\lambda/2$  wave plate inside the polarisation interferometer (see Section 6.1) and to correct for the random phase setting of the polarisation interferometer. Therefore, only  $I$  processes instead of  $X$  and  $Y$  processes, as discussed in Section 6.3.1, were measured. The storage time was set to 12.5 ns and the incident signal field contained several thousand photons. The results can be seen in Figure 6.6, where Figure 6.6 (a) represents the QPT result for a signal field without a memory interaction and Figure 6.6 (b) represents the QPT result for a stored and a retrieved signal. The process purity for the first case (no memory interaction) is 99% and the process purity for the second case (retrieved signal) is 99% as well. These measurements suggest that the polarisation interferometer works perfectly and that the coherence between the two polarisation memories is completely preserved.

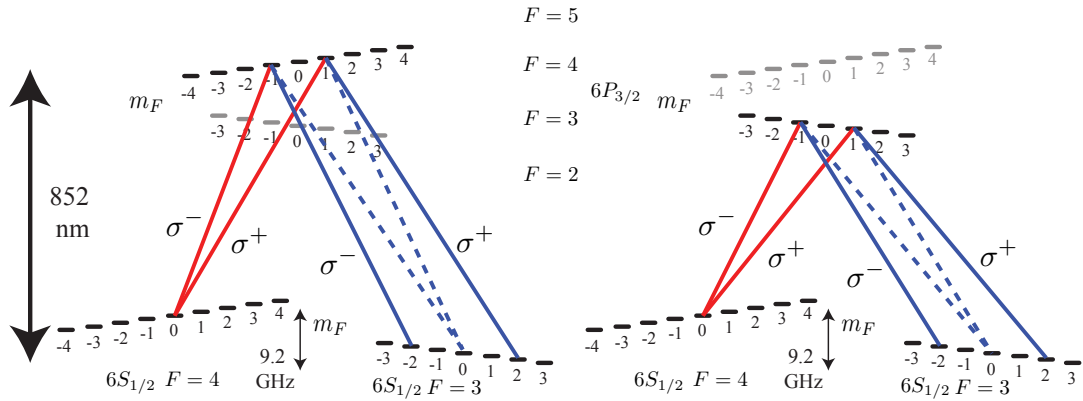


Figure 6.7: Zeeman qubit memory.

### 6.3.5 Alternatives for qubit storage

An other alternative technique for storing a polarisation qubit could for example be implemented in a single spin wave excitation by making use of the polarisation selection rules that apply to the atoms in the presence of magnetic guide field. Imagine a magnetic guide field along the axis of propagation, which causes a Zeeman splitting of the magnetic sublevels of the hyperfine states in caesium, as illustrated in Figure 6.7. Imagine furthermore that all the atoms can be prepared initially in the  $6S_{1/2}, F = 4, m_F = 0$  ground state by optical pumping. The signal field (red arrow) and the control field (blue arrow), both tuned to the caesium  $D_2$  transition but separated by 9.2 GHz, enable two possible pathways to the  $6S_{1/2}, F = 3, m_F = -2, m_F = 2$  states because the the atoms respond to a linearly polarised light field with  $\sigma^+$  and  $\sigma^-$  transitions as illustrated in Figure 6.7 in the presence of a magnetic guide field. The dashed lines correspond to forbidden transitions due to destructive interference of the corresponding pathways. The  $6S_{1/2}, F = 3, m_F = -2, m_F = 2$  magnetic sublevels serve as storage states for a polarisation qubit.

---

This approach opens the interesting opportunity to store a polarisation qubit in a single ensemble instead of using two physically separated ensembles as described in Section 6.1. However, optical pumping of the system into the  $6S_{1/2}, F = 4, m_F = 0$  state is experimentally challenging and polarisation filtering of the strong control field will not be possible because the control field has to have the same polarisation as the signal field. A solution to this would be to tune the angle of the signal and the control field such that spatial filtering could be applied. It becomes clear from this discussion that this approach, as well as the polarisation interferometer described in Section 6.1, have advantages and disadvantages, and the applicability of either approach will have to be determined in future experiments.



# Chapter 7

## Conclusions

Starting from an almost empty optical table, with nothing more than a Tsunami laser oscillator, some mirror mounts, photodiodes and first ideas of how to approach the challenge of generating and filtering two different, coherent laser beams separated by 9.2 GHz from each other, this project led to the complete demonstration of a fully functional, easy-to-operate room-temperature optical quantum memory, based on the until then only theoretically proposed, far off-resonant two-photon Raman interaction.

This entirely different approach to quantum memories enables the storage and retrieval of weak coherent laser pulses at the single photon level, with a bandwidth in the GHz regime, more than 100 times larger than most of the other quantum memories at present. Furthermore, the Raman-based memory scheme allows for implementing a room-temperature optical memory that is able to operate with a low unconditional noise floor<sup>1</sup> in the quantum regime. Using this technique,

---

<sup>1</sup>A low unconditional noise floor is key to operating at the single-photon level, because it ensures that the post-storage state is not contaminated by spontaneously initiated background noise, a problem which is often overlooked in experiments using conditional measurements.

most of the noise sources that afflict other room-temperature, EIT-based memory implementations when operating at the single-photon level can be avoided.

In addition, storage efficiencies of more than 30% at the single photon level and storage times of up to 4 microseconds are achieved, a combination of features that could already be used for increasing multi-photon rates obtained from parametric down-conversion sources. Multiple readout of a single stored excitation has been observed, leading to a complete (100%) readout after several readout events with less than unity efficiency. Furthermore, a dual rail polarisation memory is implemented demonstrating the Raman memory's capability for storing and retrieving real qubits, a key requirement for future quantum applications.

In order to demonstrate all these results, many hurdles had to be mastered successfully. These include: creating the appropriate ensemble of caesium atoms for the quantum memory, building an external cavity diode laser, implementing optical pumping of the caesium ensemble and preparing it in the ground state, selecting the right pulses from the 80 MHz pulse train, generating the 9.2 GHz shifted signal field from the laser oscillator, building a spectrometer with a resolution of 9.2 GHz or 0.02 nm for verifying the sideband generation, filtering sidebands and the carrier after the EOM, timing of all the laser pulses, filtering of the strong control field after the vapour cell via polarisation and spectral filtering, detecting individual signal pulses instead of a multiple-averaging, extending the lifetime and efficiency of the memory and increasing the detection efficiency to single-photon-level sensitivity.

# Chapter 8

## Outlook

Quantum memories are probably going to play a major role in future quantum information technology networks, where quantum information is distributed on intercontinental scales with the help of quantum repeaters or stored, processed and shared in local nodes. Real-world applications, like quantum repeaters and quantum computers are still in the distant future because at this stage there are no quantum memories that work efficiently enough with real single photons, and because there are only a few quantum computation algorithms and nobody at this time really knows how to build a functional quantum computer.

However, first commercial products, like the quantum cryptography systems from IDquantique in Geneva, Switzerland, that enable the secure communication of encrypted quantum information over short distances, are already available on the market. In addition there has been tremendous progress in research on quantum memories, single photon detectors and single photon sources during the last 3 1/2 years that will soon enable the construction of a functional quantum repeater system. Combined with the aforementioned quantum cryptography sys-

tems this might soon enable secure long-distance quantum information transfer, which we all could benefit from.

At last I present a couple of ideas on how some results presented in my thesis could be improved in the future, and what type of experiments are planned next:

### **Memory efficiency**

The memory efficiency of the Raman quantum memory mainly depends on the optical depth  $d$  and the control field power  $\Omega$ , as discussed in Section 2.8, but also on the readout geometry. Backward retrieval, as suggested in<sup>[93]</sup>, predicts a significant enhancement compared to the collinear forward readout.

Currently work is undertaken by new DPhil students in building an amplifier system for the 300 ps laser pulses in order to enhance the control field power and boost the memory efficiency.

### **Single photons**

All the work presented in this thesis was done with weak coherent signal states. We currently work on building a parametric downconversion source (PDC) using a PPKTP waveguide structure in order to generate true single photons with a bandwidth suitable for the Raman memory. The bandwidths of these photons will be on the order of  $\sim 1.5$  GHz, comparable to the laser bandwidth of the Tsunami oscillator that is in use at the moment.

### **Qubit memory**

The most recent results of the qubit memory demonstrate that the polarisation interferometer works perfectly well and that the coherence between the two polarisation memories is completely preserved (see Section 6.3.4). Work is in progress to extend the storage time of the qubit memory and combine it with real single

photons from a PDC source. This provides a whole new spectrum of different experiments that can then be performed, such as the entanglement of an atomic ensemble and a photon, or a real qubit memory where different ensembles are entangled with one another.



# Bibliography

- [1] Planck, M. Ueber die elementarquanta der materie und der elektricität. *Annalen der Physik* **4**, 564–566 (1901). [1](#)
- [2] Einstein, A. Über einen die erzeugung und verwandlung des liches betreffenden heuristischen gesichtspunkt. *Annalen der Physik* **322**, 132–148 (1905). [1](#)
- [3] Planck, M. Ueber das gesetz der energieverteilung im normalspectrum. *Annalen der Physik* **4**, 553–563 (1901). [1](#)
- [4] Bohr, N. On the constitution of atoms and molecules. *Philosophical Magazine* **26**(1) (1913). [1](#)
- [5] Maiman, T. H. Stimulated optical radiation in ruby. *Nature* **187**, 493 (1960). [1](#), [74](#)
- [6] Palvia, P., Palvia, S. C. J., and Harris, A. L. *Global Information Technology*. Ivy League Publisher, (2007). [2](#)
- [7] Kimble, H. J., Dagenais, M., and Mandel, L. Photon antibunching in resonance fluorescence. *Phys. Rev. Lett.* **39**, 691 (1977). [2](#)
- [8] Phillips, W. D., Prodan, J. V., and Metcalf, H. J. Laser cooling and electromagnetic trapping of neutral atoms. *Journal of the Optical Society of*

- America B* **2**, 1751–1767 (1985). [2](#)
- [9] Kuklinski, J. R., Gaubatz, U., Hioe, F. T., and Bergmann, K. Adiabatic population transfer in a three-level system driven by delayed laser pulses. *Phys. Rev. A* **40**, 6741 (1989).
- [10] Davis, K. B., Mewes, M. O., Andrews, M. R., van Druten, N. J., Durfee, D. S., Kurn, D. M., and Ketterle, W. Bose-einstein condensation in a gas of sodium atoms. *Phys. Rev. Lett.* **75**, 3969 (1995).
- [11] Fleischhauer, M. and Lukin, M. D. Quantum memory for photons: Dark-state polaritons. *Phys. Rev. A* **65**, 022314 (2002).
- [12] Schmidt-Kaler, F., Haffner, H., Riebe, M., Gulde, S., Lancaster, G. P. T., Deuschle, T., Becher, C., Roos, C. F., Eschner, J., and Blatt, R. Realization of the cirac-zoller controlled-not quantum gate. *Nature* **422**, 408–411 (2003). [3](#)
- [13] Mosley, P. J., Lundeen, J. S., Smith, B. J., Wasylczyk, P., U'Ren, A. B., Silberhorn, C., and Walmsley, I. A. Heralded generation of ultrafast single photons in pure quantum states. *Phys. Rev. Lett.* **100**, 133601 (2008).
- [14] Cohen, O., Lundeen, J. S., Smith, B. J., Puentes, G., Mosley, P. J., and Walmsley, I. A. Tailored photon-pair generation in optical fibers. *Phys. Rev. Lett.* **102**, 123603 (2009). [2](#)
- [15] Duan, L.-M., Lukin, M. D., Cirac, J. I., and Zoller, P. Long-distance quantum communication with atomic ensembles and linear optics. *Nature* **414**, 413–418 (2001). [2](#), [3](#), [141](#), [153](#)
- [16] Ladd, T. D., Jelezko, F., Laflamme, R., Nakamura, Y., Monroe, C., and O'Brien, J. L. Quantum computers. *Nature* **464**, 45–53 (2010). [2](#)

- [17] Perez-Delgado, C. and Kok, P. What is a quantum computer, and how do we build one? *Arxiv*, 0906.4344 (2009).
- [18] DiVincenzo, D. P. and IBM. The physical implementation of quantum computation. *Arxiv*, 0002077 (2000).
- [19] Kok, P., Munro, W., Nemoto, K., Ralph, T., Dowling, J., and Milburn, G. Linear optical quantum computing with photonic qubits. *Rev. Mod. Phys.* **79**, 135–174 (2007). [2](#)
- [20] Gisin, N., Ribordy, G., Tittel, W., and Zbinden, H. Quantum cryptography. *Rev. Mod. Phys.* **74**, 145 (2002). [2](#), [3](#)
- [21] Sangouard, N., Simon, C., de Riedmatten, H., and Gisin, N. Quantum repeaters based on atomic ensembles and linear optics. *Arxiv*, 0906.2699 (2009). [2](#)
- [22] Kok, P., Williams, C. P., and Dowling, J. P. Practical quantum repeaters with linear optics and double-photon guns. *Arxiv*, 0203134 (2002).
- [23] Briegel, H.-J., Dür, W., Cirac, J. I., and Zoller, P. Quantum repeaters: The role of imperfect local operations in quantum communication. *Phys. Rev. Lett.* **81**, 5932 (1998). [2](#), [3](#), [141](#)
- [24] O’Brien, J. L., Pryde, G. J., Gilchrist, A., James, D. F. V., Langford, N. K., Ralph, T. C., and White, A. G. Quantum process tomography of a controlled-not gate. *Phys. Rev. Lett.* **93**, 080502 (2004). [3](#), [161](#)
- [25] Ottaviani, C., Rebecqute, S., Vitali, D., and Tombesi, P. Quantum phase-gate operation based on nonlinear optics: Full quantum analysis. *Phys. Rev. A* **73**, 010301 (2006).

- [26] Plantenberg, J. H., de Groot, P. C., Harmans, C. J. P. M., and Mooij, J. E. Demonstration of controlled-NOT quantum gates on a pair of superconducting quantum bits. *Nature* **447**, 836–839 (2007).
- [27] Zou, X., Pahlke, K., and Mathis, W. Quantum phase-gate implementation for trapped ions in thermal motion. *Phys. Rev. A* **66**, 044307 (2002). [3](#)
- [28] Brun, T., Devetak, I., and Hsieh, M.-H. Correcting quantum errors with entanglement. *Science* **314**, 436–439 (2006). [4](#)
- [29] Cory, D. G., Price, M. D., Maas, W., Knill, E., Laflamme, R., Zurek, W. H., Havel, T. F., and Somaroo, S. S. Experimental quantum error correction. *Phys. Rev. Lett.* **81**, 2152 (1998).
- [30] Shor, P. W. Scheme for reducing decoherence in quantum computer memory. *Phys. Rev. A* **52**, 2493 (1995).
- [31] Steane, A. M. Error correcting codes in quantum theory. *Phys. Rev. Lett.* **77**, 793 (1996).
- [32] Steane, A. Quantum error correction: Down the information back-alley. *Nature Physics* **2**, 805–806 (2006). [4](#)
- [33] Reim, K. F., Nunn, J., Lorenz, V. O., Sussman, B. J., Lee, K. C., Langford, N. K., Jaksch, D., and Walmsley, I. A. Towards high-speed optical quantum memories. *Nature Photonics* **4**, 218–221 (2010). [4](#), [26](#), [30](#), [40](#), [123](#), [125](#), [132](#)
- [34] Julsgaard, B., Sherson, J., Cirac, J. I., Fiurasek, J., and Polzik, E. S. Experimental demonstration of quantum memory for light. *Nature* **432**, 482–486 (2004). [4](#)
- [35] Hedges, M. P., Longdell, J. J., Li, Y., and Sellars, M. J. Efficient quantum

- memory for light. *Nature* **465**, 1052–1056 (2010). [30](#)
- [36] Hosseini, M., Sparkes, B. M., Lam, P. K., and Buchler, B. C. High efficiency coherent optical memory with warm rubidium vapour. *Arxiv*, 1009.0567 (2010). [4](#)
- [37] Longdell, J. J., Fraval, E., Sellars, M. J., and Manson, N. B. Stopped light with storage times greater than one second using electromagnetically induced transparency in a solid. *Phys. Rev. Lett.* **95**, 063601 (2005). [4](#)
- [38] Schnorrberger, U., Thompson, J. D., Trotzky, S., Pugatch, R., Davidson, N., Kuhr, S., and Bloch, I. Electromagnetically induced transparency and light storage in an atomic mott insulator. *Phys. Rev. Lett.* **103**, 033003 (2009). [4](#), [114](#)
- [39] Nunn, J., Reim, K., Lee, K. C., Lorenz, V. O., Sussman, B. J., Walmsley, I. A., and Jaksch, D. Multimode memories in atomic ensembles. *Phys. Rev. Lett.* **101**, 260502 (2008). [4](#), [9](#), [24](#), [117](#), [156](#)
- [40] Simon, C., de Riedmatten, H., Afzelius, M., Sangouard, N., Zbinden, H., and Gisin, N. Quantum repeaters with photon pair sources and multimode memories. *Phys. Rev. Lett.* **98**, 190503 (2007). [4](#), [117](#)
- [41] Eisaman, M. D., Andre, A., Massou, F., Fleischhauer, M., Zibrov, A. S., and Lukin, M. D. Electromagnetically induced transparency with tunable single-photon pulses. *Nature* **438**, 837–841 (2005). [4](#), [7](#), [141](#)
- [42] Novikova, I., Gorshkov, A. V., Phillips, D. F., Sorensen, A. S., Lukin, M. D., and Walsworth, R. L. Optimal control of light pulse storage and retrieval. *Phys. Rev. Lett.* **98**, 243602 (2007).
- [43] Novikova, I., Phillips, N. B., and Gorshkov, A. V. Optimal light storage

- with full pulse-shape control. *Phys. Rev. A* **78**, 021802 (2008). [7](#)
- [44] Reim, K. F., Michelberger, P., Lee, K. C., Nunn, J., Langford, N. K., and Walmsley, I. A. Single-photon-level quantum memory at room temperature. *Arxiv*, 1010.3975 (2010). [4](#), [7](#), [116](#), [142](#), [150](#), [151](#), [153](#), [155](#)
- [45] Baluktsian, T., Urban, C., Bublat, T., Giessen, H., Löw, R., and Pfau, T. Fabrication method for microscopic vapor cells for alkali atoms. *Optics Letters* **35**, 1950 (2010). [4](#), [30](#)
- [46] Wu, B., Hulbert, J. F., Lunt, E. J., Hurd, K., Hawkins, A. R., and Schmidt, H. Slow light on a chip via atomic quantum state control. *Nature Photonics* **4**, 776–779 (2010). [4](#), [30](#)
- [47] Simon, J., Tanji, H., Thompson, J. K., and Vuletić, V. Interfacing collective atomic excitations and single photons. *Phys. Rev. Lett.* **98**, 183601 (2007). [4](#), [7](#), [30](#), [141](#)
- [48] Chen, S., Chen, Y.-A., Strassel, T., Yuan, Z.-S., Zhao, B., Schmiedmayer, J., and Pan, J.-W. Deterministic and storable single-photon source based on a quantum memory. *Phys. Rev. Lett.* **97**, 173004 (2006). [26](#)
- [49] Matsukevich, D. N., Chaneliere, T., Jenkins, S. D., Lan, S.-Y., Kennedy, T. A. B., and Kuzmich, A. Deterministic single photons via conditional quantum evolution. *Phys. Rev. Lett.* **97**, 013601 (2006). [4](#), [30](#), [141](#)
- [50] Appel, J., Figueroa, E., Korystov, D., Lobino, M., and Lvovsky, A. I. Quantum memory for squeezed light. *Phys. Rev. Lett.* **100**, 093602 (2008). [5](#), [142](#)
- [51] Jensen, K., Wasilewski, W., Krauter, H., Fernholz, T., Nielsen, B. M., Owari, M., Plenio, M. B., Serafini, A., Wolf, M. M., and Polzik, E. S.

- Quantum memory for entangled continuous-variable states. *Nature Physics* **7**, 13–16 (2011). [142](#)
- [52] Braunstein, S. L. and van Loock, P. Quantum information with continuous variables. *Rev. Mod. Phys.* **77**, 513 (2005). [5](#)
- [53] Hammerer, K., Sørensen, A. S., and Polzik, E. S. Quantum interface between light and atomic ensembles. *Rev. Mod. Phys.* **82**, 1041 (2010). [5](#)
- [54] Boller, K.-J., Imamolu, A., and Harris, S. E. Observation of electromagnetically induced transparency. *Phys. Rev. Lett.* **66**, 2593 (1991). [5](#)
- [55] Fleischhauer, M., Imamoglu, A., and Marangos, J. P. Electromagnetically induced transparency: Optics in coherent media. *Rev. Mod. Phys.* **77**, 633 (2005). [5](#)
- [56] Hau, L. V., Harris, S. E., Dutton, Z., and Behroozi, C. H. Light speed reduction to 17 metres per second in an ultracold atomic gas. *Nature* **397**, 594–598 (1999). [6](#)
- [57] Fleischhauer, M. and Lukin, M. D. Dark-state polaritons in electromagnetically induced transparency. *Phys. Rev. Lett.* **84**, 5094 (2000). [6](#)
- [58] Bajcsy, M., Hofferberth, S., Balic, V., Peyronel, T., Hafezi, M., Zibrov, A. S., Vuletic, V., and Lukin, M. D. Efficient all-optical switching using slow light within a hollow fiber. *Phys. Rev. Lett.* **102**, 203902 (2009). [6](#)
- [59] Liu, C., Dutton, Z., Behroozi, C. H., and Hau, L. V. Observation of coherent optical information storage in an atomic medium using halted light pulses. *Nature* **409**, 490–493 (2001). [6](#)
- [60] Mücke, M., Figueroa, E., Bochmann, J., Hahn, C., Murr, K., Ritter, S.,

- Villas-Boas, C. J., and Rempe, G. Electromagnetically induced transparency with single atoms in a cavity. *Nature* **465**, 755–758 (2010). [7](#)
- [61] Zhang, J., Hernandez, G., and Zhu, Y. Slow light with cavity electromagnetically induced transparency. *Opt. Lett.* **33**, 46–48 (2008). [7](#)
- [62] Baldit, E., Bencheikh, K., Monnier, P., Levenson, J. A., and Rouget, V. Ultraslow light propagation in an inhomogeneously broadened rare-earth ion-doped crystal. *Phys. Rev. Lett.* **95**, 143601 (2005). [7](#)
- [63] Ham, B., Hemmer, P., and Shahriar, M. Efficient electromagnetically induced transparency in a rare-earth doped crystal. *Optics Commun.* **144**, 227–230 (1997). [7](#)
- [64] Manz, S., Fernholz, T., Schmiedmayer, J., and Pan, J.-W. Collisional decoherence during writing and reading quantum states. *Phys. Rev. A* **75**, 040101 (2007). [7](#), [141](#), [148](#), [150](#), [152](#)
- [65] Hsu, M. T. L., Hétet, G., Glöckl, O., Longdell, J. J., Buchler, B. C., Bachor, H., and Lam, P. K. Quantum study of information delay in electromagnetically induced transparency. *Phys. Rev. Lett.* **97**, 183601 (2006). [7](#), [141](#), [148](#), [150](#)
- [66] Nilsson, M. and Kröll, S. Solid state quantum memory using complete absorption and re-emission of photons by tailored and externally controlled inhomogeneous absorption profiles. *Opt. Lett.* **247**, 393–403 (2005). [7](#), [30](#)
- [67] Moiseev, S. A. and Ham, B. S. Photon-echo quantum memory with efficient multipulse readings. *Phys. Rev. A* **70**, 063809 (2004).
- [68] Moiseev, S. A., Tarasov, V. F., and Ham, B. S. Quantum memory photon echo-like techniques in solids. *Journal of Optics B*: **5**, 497–502 (2003). [30](#)

- [69] Moiseev, S. A. and Kröll, S. Complete reconstruction of the quantum state of a single-photon wave packet absorbed by a doppler-broadened transition. *Phys. Rev. Lett.* **87**, 173601 (2001). [7](#)
- [70] Hetet, G., Longdell, J. J., Alexander, A. L., Lam, P. K., and Sellars, M. J. Electro-optic quantum memory for light using two-level atoms. *Phys. Rev. Lett.* **100**, 023601 (2008). [8](#), [110](#), [114](#)
- [71] Staudt, M. U., Hastings-Simon, S. R., Nilsson, M., Afzelius, M., Scarani, V., Ricken, R., Suche, H., Sohler, W., Tittel, W., and Gisin, N. Fidelity of an optical memory based on stimulated photon echoes. *Phys. Rev. Lett.* **98**, 113601 (2007).
- [72] Kraus, B., Tittel, W., Gisin, N., Nilsson, M., Kroll, S., and Cirac, J. I. Quantum memory for nonstationary light fields based on controlled reversible inhomogeneous broadening. *Phys. Rev. A* **73**, 020302 (2006).
- [73] Alexander, A. L., Longdell, J. J., Sellars, M. J., and Manson, N. B. Photon echoes produced by switching electric fields. *Phys. Rev. Lett.* **96**, 043602 (2006). [8](#)
- [74] Hetet, G., Hosseini, M., Sparkes, B. M., Oblak, D., Lam, P. K., and Buchler, B. C. Photon echoes generated by reversing magnetic field gradients in a rubidium vapor. *Opt. Lett.* **33**, 2323–2325 (2008). [8](#)
- [75] Afzelius, M., Simon, C., de Riedmatten, H., and Gisin, N. Multimode quantum memory based on atomic frequency combs. *Phys. Rev. A* **79**, 052329 (2009). [9](#), [10](#), [110](#)
- [76] Usmani, I., Afzelius, M., de Riedmatten, H., and Gisin, N. Mapping multiple photonic qubits into and out of one solid-state atomic ensemble. *Nature*

- Commun.* **1**, 1–7 (2010). [10](#), [11](#), [30](#)
- [77] de Riedmatten, H., Afzelius, M., Staudt, M. U., Simon, C., and Gisin, N. A solid-state light-matter interface at the single-photon level. *Nature* **456**, 773–777 (2008). [30](#), [114](#)
- [78] Clausen, C., Usmani, I., Bussieres, F., Sangouard, N., Afzelius, M., de Riedmatten, H., and Gisin, N. Quantum storage of photonic entanglement in a crystal. *Nature* **469**, 508–511 (2011). [10](#), [141](#)
- [79] Gorshkov, A. V., Andre, A., Lukin, M. D., and Sorensen, A. S. Photon storage in lambda-type optically dense atomic media. II. free-space model. *Phys. Rev. A* **76**, 033805 (2007). [11](#), [15](#), [23](#), [24](#), [25](#), [111](#), [112](#)
- [80] Nunn, J., Walmsley, I. A., Raymer, M. G., Surmacz, K., Waldermann, F. C., Wang, Z., and Jaksch, D. Mapping broadband single-photon wave packets into an atomic memory. *Phys. Rev. A* **75**, 011401 (2007). [15](#), [23](#), [24](#), [36](#), [110](#), [132](#)
- [81] Kozhekin, A. E., Molmer, K., and Polzik, E. Quantum memory for light. *Phys. Rev. A* **62**, 033809 (2000). [11](#), [15](#)
- [82] Raman, C. V. and Krishnan, K. S. A new type of secondary radiation. *Nature* **121**, 501–502 (1928). [11](#)
- [83] Boyd, R. W. *Nonlinear optics*. Academic Press, (2003). [12](#), [15](#), [100](#), [151](#)
- [84] Scully, M. O. and Zubairy, M. S. *Quantum optics*. Cambridge University Press, (1997). [15](#), [20](#)
- [85] Raymer, M. G. and Mostowski, J. Stimulated raman scattering: Unified treatment of spontaneous initiation and spatial propagation. *Phys. Rev. A*

- 24, 1980 (1981). [15](#), [22](#)
- [86] Raymer, M. and Walmsley, I. A. The quantum coherence properties of stimulated raman-scattering. *Progress in optics* **28**, 181 (1990). [15](#)
- [87] Loudon, R. *The Quantum Theory of Light*. Oxford University Press, (2004). [17](#), [160](#)
- [88] Nunn, J. *Quantum Memory in Atomic Ensembles*. PhD thesis, University of Oxford, (2008). [20](#), [21](#), [23](#), [24](#), [43](#), [46](#), [67](#), [156](#)
- [89] Fox, M. *Quantum Optics: An introduction*. Oxford University Press, (2006). [20](#)
- [90] Gorshkov, A. V., Andre, A., Lukin, M. D., and Sorensen, A. S. Photon storage in lambda-type optically dense atomic media. i. cavity model. *Phys. Rev. A* **76**, 033804 (2007). [24](#)
- [91] Gorshkov, A. V., Andre, A., Fleischhauer, M., Sorensen, A. S., and Lukin, M. D. Universal approach to optimal photon storage in atomic media. *Phys. Rev. Lett.* **98**, 123601 (2007). [24](#)
- [92] Nunn, J., Dorner, U., Michelberger, P., Reim, K. F., Lee, K. C., Langford, N. K., Walmsley, I. A., and Jaksch, D. Quantum memory in an optical lattice. *Phys. Rev. A* **82**, 022327 (2010). [24](#)
- [93] Surmacz, K., Nunn, J., Reim, K., Lee, K. C., Lorenz, V. O., Sussman, B., Walmsley, I. A., and Jaksch, D. Efficient spatially resolved multimode quantum memory. *Phys. Rev. A* **78**, 033806 (2008). [25](#), [111](#), [112](#), [113](#), [117](#), [125](#), [153](#), [178](#)
- [94] Choi, K. S., Deng, H., Laurat, J., and Kimble, H. J. Mapping photonic

- entanglement into and out of a quantum memory. *Nature* **452**, 67–71 (2008).  
[26](#), [30](#), [141](#)
- [95] Steck, D. A. Cesium d line data. *available online at* <http://steck.us/alkalidata> (2009). [26](#), [28](#), [29](#), [39](#), [41](#), [42](#), [51](#), [76](#),  
[114](#), [148](#), [152](#)
- [96] Steck, D. A. Rubidium 87 d line data. <http://steck.us/alkalidata> (2009).  
[28](#), [29](#)
- [97] Lee, K., Sussman, B. J., Nunn, J., Lorenz, V., Reim, K., Jaksch, D., Walm-  
sley, I., Spizzirri, P., and Prawer, S. Comparing phonon dephasing lifetimes  
in diamond using transient coherent ultrafast phonon spectroscopy. *Dia-  
mond and Related Materials* **19**, 1289–1295 (2010). [28](#)
- [98] Leonard, D., Krishnamurthy, M., Reaves, C. M., Denbaars, S. P., and  
Petroff, P. M. Direct formation of quantum-sized dots from uniform co-  
herent islands of InGaAs on GaAs surfaces. *Appl. Phys. Lett.* **63**, 3203  
(1993). [29](#)
- [99] Böttger, T., Thiel, C. W., Sun, Y., and Cone, R. L. Optical decoherence  
and spectral diffusion at 1.5 $\mu\text{m}$  in. *Phys. Rev. B* **73**, 075101 (2006). [29](#)
- [100] Davies, G. and Hamer, M. F. Optical studies of the 1.945 eV vibronic band  
in diamond. *Proceedings of the Royal Society of London. A. Mathematical  
and Physical Sciences* **348**, 285–298 (1976). [29](#)
- [101] Neumann, P., Kolesov, R., Naydenov, B., Beck, J., Rempp, F., Steiner,  
M., Jacques, V., Balasubramanian, G., Markham, M. L., Twitchen, D. J.,  
Pezzagna, S., Meijer, J., Twamley, J., Jelezko, F., and Wrachtrup, J. Quan-  
tum register based on coupled electron spins in a room-temperature solid.

- Nature Physics* **6**, 249–253 (2010). [30](#)
- [102] Kubler H., P., S., Baluktsian T., Low R., and Pfau T. Coherent excitation of rydberg atoms in micrometre-sized atomic vapour cells. *Nature Photonics* **4**, 112–116 (2010). [30](#)
- [103] Vetsch, E., Reitz, D., Sagué, G., Schmidt, R., Dawkins, S. T., and Rauschenbeutel, A. Optical interface created by Laser-Cooled atoms trapped in the evanescent field surrounding an optical nanofiber. *Phys. Rev. Lett.* **104**, 203603 (2010). [30](#)
- [104] Raymer, M. G., Walmsley, I. A., Mostowski, J., and Sobolewska, B. Quantum theory of spatial and temporal coherence properties of stimulated raman scattering. *Phys. Rev. A* **32**, 332 (1985). [36](#), [52](#), [153](#)
- [105] Sørensen, M. W. and Sørensen, A. S. Three-dimensional theory of stimulated raman scattering. *Phys. Rev. A* **80**, 033804 (2009). [36](#), [52](#), [153](#)
- [106] Camacho, R. M., Vudyasetu, P. K., and Howell, J. C. Four-wave-mixing stopped light in hot atomic rubidium vapour. *Nature Photonics* **3**, 103–106 (2009). [40](#), [116](#), [125](#), [132](#)
- [107] Essen, L. and Parry, J. V. L. An atomic standard of frequency and time interval: A caesium resonator. *Nature* **176**, 280–282 (1955). [41](#)
- [108] Sansonetti, J. E. and Martin, W. C. *Handbook of Basic Atomic Spectroscopy Data*. National Institute of Standards and Technology, (2003). [41](#)
- [109] Foot, C. *Atomic physics*. Oxford University Press, (2007). [45](#), [74](#)
- [110] Ricci, L., Weidemüller, M., Esslinger, T., Hemmerich, A., Zimmermann, C., Vuletic, V., König, W., and Hänsch, T. W. A compact grating-stabilized

- diode laser system for atomic physics. *Opt. Commun.* **117**, 541–549 (1995).  
[47](#)
- [111] Demtröder, W. *Laser Spectroscopy*. Springer, (2003). [53](#)
- [112] Hecht, E. *Optics*. Addison Wesley, (2002). [53](#)
- [113] Roy, R., Agrawal, D. K., and McKinstry, H. A. Very low thermal expansion coefficient materials. *Annual Review of Materials Science* **19**, 59–81 (1989).  
[64](#)
- [114] Kastler, A. Quelques suggestions concernant la production optique et la détection optique d'une inégalité de population des niveaux de quantification spatiale des atomes. *Journal de physique et le radium* **11**(255) (1950).  
[74](#)
- [115] Siegman, A. E. *Lasers*. University Science Books, (1986). [74](#)
- [116] de Tomasi, F., Allegrini, M., Arimondo, E., Agarwal, G. S., and Ananthalakshmi, P. Collision-enhanced resonance of laser-diode-excited cs in a buffer gas. *Phys. Rev. A* **48**, 3820 (1993). [78](#)
- [117] Hosseini, M., Sparkes, B. M., Hetet, G., Longdell, J. J., Lam, P. K., and Buchler, B. C. Coherent optical pulse sequencer for quantum applications. *Nature* **461**, 241–245 (2009). [110](#)
- [118] Sabooni, M., Beaudoin, F., Walther, A., Lin, N., Amari, A., Huang, M., and Kröll, S. Storage and recall of weak coherent optical pulses with an efficiency of 25%. *Arxiv*, 0912.2525 (2009).
- [119] Lobino, M., Kupchak, C., Figueroa, E., and Lvovsky, A. I. Memory for light as a quantum process. *Phys. Rev. Lett.* **102**, 203601 (2009).

- [120] Zhao, B., Chen, Y., Bao, X., Strassel, T., Chuu, C., Jin, X., Schmiedmayer, J., Yuan, Z., Chen, S., and Pan, J. A millisecond quantum memory for scalable quantum networks. *Nature Physics* **5**, 95–99 (2009).
- [121] Phillips, N. B., Gorshkov, A. V., and Novikova, I. Optimal light storage in atomic vapor. *Phys. Rev. A* **78**, 023801 (2008). [110](#)
- [122] Vega, A., Leaird, D. E., and Weiner, A. M. High-speed direct space-to-time pulse shaping with 1 ns reconfiguration. *Opt. Lett.* **35**, 1554–1556 (2010). [112](#)
- [123] Park, Y., Asghari, M. H., Ahn, T., and Azana, J. Transform-limited picosecond pulse shaping based on temporal coherence synthesization. *Opt. Express* **15**, 9584–9599 (2007).
- [124] Heritage, J. P., Weiner, A. M., and Thurston, R. N. Picosecond pulse shaping by spectral phase and amplitude manipulation. *Optics Letters* **10**, 609–611 (1985). [112](#)
- [125] Boozer, A. D., Boca, A., Miller, R., Northup, T. E., and Kimble, H. J. Reversible state transfer between light and a single trapped atom. *Phys. Rev. Lett.* **98**, 193601 (2007). [114](#)
- [126] Saglamyurek, E., Sinclair, N., Jin, J., Slater, J. A., Oblak, D., Bussieres, F., George, M., Ricken, R., Sohler, W., and Tittel, W. Broadband waveguide quantum memory for entangled photons. *Nature* **469**, 512–515 (2011). [115](#)
- [127] Collins, O., Jenkins, S., Kuzmich, A., and Kennedy, T. Multiplexed memory-insensitive quantum repeaters. *Phys. Rev. Lett.* **98**, 60502 (2007). [117](#)
- [128] Krishnamachari, V. V., Andresen, E. R., Keiding, S. R., and Potma, E. O.

- An active interferometer-stabilization scheme with linear phase control. *Optics Express* **14**, 5210–5215 (2006). [118](#)
- [129] White, R. G. and Emmony, D. C. Active feedback stabilisation of a michelson interferometer using a flexure element active feedback stabilisation of a michelson interferometer using a flexure element. *Journal of Physics E* (1985). [118](#)
- [130] Bouwmeester, D., Pan, J., Mattle, K., Eibl, M., Weinfurter, H., and Zeilinger, A. Experimental quantum teleportation. *Nature* **390**, 575–579 (1997). [132](#)
- [131] Chou, C.-W., Laurat, J., Deng, H., Choi, K. S., de Riedmatten, H., Felinto, D., and Kimble, H. J. Functional quantum nodes for entanglement distribution over scalable quantum networks. *Science* **316**, 1316–1320 (2007). [141](#)
- [132] Chen, Y.-A., Chen, S., Yuan, Z.-S., Zhao, B., Chuu, C.-S., Schmiedmayer, J., and Pan, J.-W. Memory-built-in quantum teleportation with photonic and atomic qubits. *Nature Physics* **4**, 103–107 (2008).
- [133] Choi, K. S., Goban, A., Papp, S. B., van Enk, S. J., and Kimble, H. J. Entanglement of spin waves among four quantum memories. *Nature* **468**, 412–416 (2010). [141](#)
- [134] Lukin, M. D., Matsko, A. B., Fleischhauer, M., and Scully, M. O. Quantum noise and correlations in resonantly enhanced wave mixing based on atomic coherence. *Phys. Rev. Lett.* **82**, 1847 (1999). [151](#)
- [135] Phillips, N. B., Gorshkov, A. V., and Novikova, I. Slow light propagation and amplification via electromagnetically induced transparency and four-

- wave mixing in an optically dense atomic vapor. *J. Mod. Optic.* **56**, 1916 (2009). [151](#)
- [136] Ekert, A. K. Quantum cryptography based on bell's theorem. *Phys. Rev. Lett.* **67**, 661 (1991). [153](#)
- [137] Nielsen, M. A. and Chuang, I. L. *Quantum Computation and Quantum Information*. Cambridge University Press, (2004). [159](#), [160](#), [161](#)
- [138] Langford, N. *Encoding, manipulating and measuring quantum information in optics*. PhD thesis, University of Queensland, (2007). [160](#)
- [139] Greenberger, D., Hentschel, K., and Weinert, F. *Compendium of Quantum Physics*. Springer Berlin Heidelberg, (2009). [160](#)
- [140] Taylor, G. Interference fringes with feeble light. *Proc. Cambridge Philos. Soc.* **15**, 114–115 (1909). [160](#)
- [141] Adamson, R. B. A. and Steinberg, A. M. Improving quantum state estimation with mutually unbiased bases. *0808.0944* (2008). [160](#), [161](#)
- [142] Wootters, W. K. and Fields, B. D. Optimal state-determination by mutually unbiased measurements. *Annals of Physics* **191**, 363–381 (1989). [160](#), [161](#)
- [143] Ingersoll, L. R. and Liebenberg, D. H. The faraday effect in gases and vapors. i. *J. Opt. Soc. America* **44**, 566–570 (1954). [169](#)
- [144] Siddons, P., Bell, N. C., Cai, Y., Adams, C. S., and Hughes, I. G. A gigahertz-bandwidth atomic probe based on the slow-light faraday effect. *Nature Photonics* **3**, 225–229 (2009). [169](#)
- [145] Michelberger, P. and England, D. *To be published* (2011). [170](#)